DC Superconducting Busbar for All Electric Aircraft Propulsion System

Gaurav Gautam

Department of Electronic and Electrical Engineering

University of Strathclyde, Glasgow

United Kingdom.

A thesis submitted for the degree of

Doctor of Philosophy

January 2025

Copyright Declaration

This thesis is the result of the author's original research. It has been composed by the author and has not been previously submitted for examination which has led to the award of a degree.

The copyright of this thesis belongs to the author under the terms of the United Kingdom Copyright Acts as qualified by University of Strathclyde Regulation 3.50. Due acknowledgement must always be made of the use of any material contained in, or derived from, this thesis.

Signed:

Gaurav Gautam

Date: Tuesday 28$^{\text{th}}$ January, 2025

Abstract

Second-generation, high-temperature superconducts (HTS) offer high current densities suitable for various high-power applications such as magnetic resonance imaging (MRI) magnets, electrical propulsion systems for aircraft, high-field magnets for fusion power plants, and magnetic levitation trains. While HTS is an effective solution for high-current applications, challenges arise due to the limited critical current capacity of a single HTS tape, typically in the order of a few hundred amps. To make them suitable for high-current applications, multiple tapes need to be grouped together. However, this process is complicated by the flat geometry of the HTS tape.

This thesis explores the design of a superconducting busbar for use in high-power applications within electric aircraft power distribution systems. A prototype of the superconducting busbar was created based on electromagnetic modelling and underwent testing in a laboratory environment.

A 2D electromagnetic busbar model with multiple high-temperature superconducting tapes was developed using TA-formulation. The electromagnetic model helps to understand the effect of self-field on critical current, this effect can't be neglected especially for high current scenarios, where multiple tapes are involved in the design. The modeling demonstrates how to reduce the impact of self-field on the critical current.

Additionally, a 2D electromagnetic model of the busbar is developed with H-formulation. This model helps to understand the current-sharing between the layers of the busbar during the steady-state and fault conditions. The busbar is equipped with a fault-tolerant design capable of withstanding fault events during transients. For the analysis and understanding of the fault-tolerant mechanism, H-formulation is used.

ii

A prototype was developed based on the modelling analysis and tested in a laboratory environment. The prototype superconducting busbar was tested against DC using a DC power supply in a liquid nitrogen environment. It was observed from modelling that introducing a gap between the HTS tapes reduces the effect of self-field on the critical current, which was not previously demonstrated. In the literature the superconducting busbar designs are developed for high current applications but not much emphasis given on the design which helps to reduce the effect of self-field on critical current. In this work, a novel design was developed to increase efficiency and reduce the overall cost. Copper tapes were used to introduce gaps between the HTS tapes, enhancing the design's fault tolerance capability. The prototype was also tested under fault current conditions, and its ability to ride through faults was explored. Additionally, low-resistive joints were implemented with multiple ReBCO tapes, and both 90-degree and 180-degree joints were tested. The busbar with these joints underwent thermal and power cycling to assess any degradation in electrical parameters, an aspect not previously demonstrated.

In this thesis, a superconducting busbar design is proposed and tested, which can ride through fault events with a design that reduces the effect of self-field on critical current. This busbar is also equipped with low-resistive joints and has undergone rigorous thermal and power cycling to assess the reliability and durability. Overall, the design offers a compact and efficient solution for high-current applications.

Acknowledgements

me have been crucial in helping me reach this significant milestone. I will always treasure the memories we have created together, and I hope to continue to make them proud. Thank you once again for always being there for me.

Contents

Contents

List of Figures

List of Tables

Nomenclature

2G : Second Generation

AC : Alternating Current

ACT : Advanced Conductor Technologies

AEA : All Electric Aircraft

B_a : External Magnetic Field

B_c : Critical Magnetic Field

B_{c1} : Lower Critical Field

B_{Cc2} : Upper Critical Field

BSCCO : Bismuth Strontium Calcium Copper Oxide

B   Magnetic Field

$CO2$: Carbon Dioxide

CORC Conductor on Round Core

D_P   Penetration Depth

DC : Direct Current

$\mathbf{E_c}$: Electric Field Threshold

$\mathbf{F_L}$ Lorentz Force

$\mathbf{F_P}$ Pinning Force

FEA : Finite Element Analysis

H2S : Hydrogen Sulphide

HEA : Hybrid Electric Aircraft

HTS : High Temperature Superconductor

IC : Critical Current

IEEE : Institute of Electrical and Electronics Engineer

J : Transport Current Density

$\mathbf{J_c(B)}$ Field Dependent Critical Current Density

$\mathbf{J_c}$: Critical Current Density

$\mathbf{J_{c0}}$ Current Density in Absence of Field

LN2 Liquid Nitrogen

LTS : Low Temperature Superconductor

MEA : More Electric Aircraft

MgB2 : Magnesium Diboride

MRI Magnetic Resonance Imaging

NASA : National Aeronautics and Space Administration

NOx : Oxides of Nitrogen

ReBCO : Rare Earth Barium Copper Oxide

RF : Radiative Forcing, W/m^2

T$_c$ Critical Temperature

YBCO : Yttrium Barium Copper Oxide

1

Introduction

1.1 Research justification

The emission of gases and particles from aviation significantly contributes to climate warming. CO2, in particular, is a major pollutant in aviation and is largely responsibile for net anthropogenic radiative forcing. In addition to CO2, non-CO2 pollutants also play a critical role in global warming dynamics. Together, these emissions contribute significantly to a aviation's impact on radiative forcing (RF), which is quantified in watts per square meter (W/m²) [11]. The Radiative Forcing Index (RFI) is a standard metric used to represent this ratio effectively.

According to data from 2005, emissions of CO2 from aviation represented about 1.6% of the global total anthropogenic CO2 radiative forcing. Moreover, the overall net radiative forcing from aviation was estimated to make up around 4.9% of the total anthropogenic radiative forcing [12]. These statistic underscores the substantial role that aviation plays in contributing to global warming, not only through CO2 emissions but also via other pollutants that affect the atmosphere's radiative balance. Understanding and quantifying these impacts is crucial for developing strategies to mitigate the environmental footprint of the aviation sector.

Flightpath 2050, Europe's ambitious vision for aviation, targets a 75% reduction in CO2 emissions per passenger-kilometre by 2050. It also aims for a 90% reduction in nitrogen oxide (NOx) emissions and a 65% reduction in noise emissions compared to the levels of 2000 [13].

To meet these objectives, aviation electrification is emerging as a promising solution.

Aviation electrification begins with replacing traditional subsystems, such as hydraulic and pneumatic systems with electric systems and progressively replacing traditional jet engines with electric propulsion motors. Aircraft that replace their traditional sub-systems with electrical subsystems, excluding the jet propulsion system, are known as More Electric Aircraft (MEA) [14, 15]. Boeing 787 and Airbus A380 are examples of more electric aircraft they consume more electric power compared to hydraulic-powered aircraft. Compared to conventional jet engines, MEAs are more efficient and generate less noise[16]. The aircraft that use electric power for thrust generation, are categorized as Hybrid Electric Aircraft (HEA) and All Electric Aircraft (AEA) [17]. HEAs utilize both aviation fuel and jet engines for power generation, while AEAs substitute jet engines with onboard power sources.

The development roadmap for these technologies outlines anticipated power and voltage levels in [18]. For larger aircraft, capable of carrying up to 300 passengers, a distributed propulsion system is proposed, requiring power exceeding 10 MW and a voltage range of 2-5 kV [17]. The distributed propulsion architectures for power distribution systems for all-electric aircraft are documented in multiple studies [19, 20, 21]. Superconductivity plays a crucial role in supporting such architectures due to its high power-to-weight ratio, which benefits components like the power distribution system and motors [22, 23, 24, 25]. DC power distribution systems are particularly prominent in all-electric aircraft due to the technical maturity of converters. These system require high current flow from the source to the propulsion unit. High Temperature Superconductors (HTS) offer an effective solution for efficiently transferring high current, as they incur no losses while carrying DC and require less space and weight.

A superconducting busbar is a promising solution for carrying high currents in a compact and lightweight design. Although the critical current of ReBCO tapes is limited to a few hundred amperes, multiple ReBCO tapes can be grouped together to handle high currents [26, 27, 28]. This thesis comprehensively explores a superconducting busbar design with fault ride-through capability. The design also reduces the effect of the self-field on the critical current. This effect cannot be neglected in high-current applications where the design requires

multiple HTS tapes. Superconducting busbar is also equipped with low-resistive joints and put through power and thermal cycling to assess its reliability and durability.

1.1.1 Objective

The thesis focuses on developing a superconducting busbar design for the power distribution system of all-electric aircraft.

- **Parallel HTS Tapes:** The busbar should incorporate multiple HTS tapes connected in parallel, addressing the reduction in critical current caused by self-field effects.

- **Efficiency Improvement:** The design should help to mitigate self-field impacts on critical current, enhancing overall efficiency.

- **Fault Tolerance:** The busbar should be able to enhance fault tolerance, enabling it to effectively ride through fault events.

- **Low-Resistance Joints:** The busbar should include 180° and 90° low-resistance joints, demonstrating its capability to connect multiple sources and loads.

- **Performance Validation:** The joints should undergo power and thermal cycling tests to assess the busbar's performance under power and thermal stress conditions.

- **Outcome:** A superconducting busbar prototype is developed that provides a high-performance, efficient and fault-tolerant solution for high-current applications such as power distribution system of all-electric aircraft.

1.2 Principal contributions

Reduced effect of self-field on critical current design

This thesis demonstrates a superconducting busbar design that reduces the effect of the self-field on critical current. This is achieved by introducing a gap between stacked ReBCO (HTS)

tapes. Finite Element Modeling (FEM) of the superconducting busbar was conducted to analyse the effect of adding a gap between the ReBCO tapes, and based on this analysis, a prototype was developed. The influence of the self-field depends on the distance between the ReBCO tapes and can be understood with the $B = \mu_0 I / 2\pi d$, where d is the distance between the ReBCO tapes, and I is the current flowing through them. This effect cannot be neglected in designs requiring multiple ReBCO tapes with high currents, Unlike high voltage where the voltage standard is defined by IEEE guidelines, for high current no such standards are defined so in this thesis, high current refers to current more than 5 kA. For high-current applications, such as power cables and busbars, the self-field effect reduces efficiency and increases costs, as more HTS tapes are required to carry the current due to the dependency of the critical current on the self-field. In this thesis, gaps were introduced between the ReBCO tapes using copper tapes, which reduces the effect of self-field on critical current and also helps increase the fault tolerance capability of the superconducting busbar.

Superconducting busbar fault tolerance design

This thesis presents a comprehensive design for a superconducting busbar engineered to withstand fault conditions during fault events. Unlike other known superconducting busbar design the copper tapes are added in between the HTS tapes, which helps to carry the current in the fault state and helps to ride through the fault event. During fault state the current in HTS tape surpasses the critical current and offers high resistance during that period, the copper acts as stabilizer and carries the current diverted from HST tapes. The design enhances busbar performance by improving fault tolerance and maintaining functionality and reliability during electrical faults. Validation of this design was achieved through both computer-aided Finite Element Analysis (FEA) and laboratory experiments. The FEA simulations provided detailed insights into the behaviour of the busbar during steady-state and fault-state conditions. Following this, laboratory experiments subjected the busbar to controlled fault conditions to verify its performance, ensuring it could manage and recover from such events. In a fault-state, the superconducting busbar is subjected to a current above its critical current. The laboratory experiments confirmed that the superconducting busbar can ride through fault

events effectively.

Implementing and testing low-resistive joints through power and thermal cycling

In this thesis, author has developed low-resistive $90°$ and $180°$ lap-to-lap joints for superconducting busbars. The superconducting busbar design not only includes low-resistive joints but also features reduced self-field effects on critical current and enhanced fault tolerance. While data on $180°$ joints are well-documented in the literature, this research marks the implementation and testing of $90°$ joints, which has not been previously covered. To ensure the reliability and durability of the joints, repetitive thermal and power cycling tests were conducted on the prototypes. These tests simulated real-world operating conditions by exposing the joints to repeated cycles of electric loading and thermal fluctuations, allowing us to assess their long-term performance and stability. The $180°$ joints served as a comparative benchmark due to their established performance characteristics, while the introduction of $90°$ joints represents a significant advancement, offering new solutions for connecting HTS tapes in more complex configurations. The results from these tests demonstrated that both types of joints exhibit good reliability and durability, maintaining their electrical properties and structural integrity under stress.

1.3 Thesis overview

This thesis aims to investigate and design a superconducting busbar for high current application.

Chapter 1 provides an introduction to the thesis and its research objectives.

Chapter 2 offers a detailed overview of superconductivity and its underlying principles. It begins with a definition of superconductivity and the criteria that govern it. Additionally, the chapter discusses the macroscopic magnetisation theories of type II superconductors in depth.

Chapter 3 discusses the state-of-the-art high-current conductor concepts. It examines existing techniques for cabling and stacking HTS tapes, highlighting their respective advantages

and disadvantages. The stacking technique employed in this thesis is elaborated upon, with a detailed explanation of the rationale behind its selection.

Chapter 4 explores the necessity of superconductivity in all-electric aircraft. Voltage standards of traditional aircraft and power consumption in aviation is discussed. Additionally, the chapter examines future voltage standards for all-electric aircraft and the anticipated power requirements.

Chapter 5 presents a design using T-A formulation. An electromagnetic model is developed to understand the effect of the self-field on critical current, involving multiple HTS tapes in the design. Based on the insights from the modelling, a prototype is developed and tested in a liquid nitrogen environment.

Chapter 6 reports on the fault ride-through capability of the busbar. H-formulation is used to analyse the behaviour of multiple HTS tape busbar designs during steady-state and fault-state conditions. A prototype is developed and tested against fault currents to evaluate the ride-through capability of the superconducting busbar, with an assessment of its power and Joule heating tolerance.

Chapter 7 explores the busbar joints. 90^0 and 180^0 low resistive joints are implemented, and the busbar undergoes power and thermal cycling to assess the reliability of the joints.

Chapter 8 provides a comprehensive summary of the research findings. The chapter concludes by offering recommendations for future research in this area, contributing to the development of more efficient superconducting busbars for high-current applications

1.4   Publications

1. ***G. Gautam**, M. Zhang, W. Yuan, G. Burt and D. Malkin, "Fault Tolerant Superconducting Busbar With Reduced Self-Field Effect on Critical Current Design for All Electric Aircraft," in IEEE Transactions on Applied Superconductivity, vol. 34, no. 3, pp. 1-5, May 2024, Art no. 4801805, doi: 10.1109 TASC.2024.3351610.

2. ***G. Gautam**, M. Zhang, W. Yuan, G. Burt and D. Malkin, "Superconducting DC busbar with low resistive joints for all-electric aircraft propulsion system," Physica C: Superconductivity and its Applications, Volume 627, 2024, 1354617, ISSN 0921-4534, doi.org/10.1016/j.physc.2024.1354617.

3. Abdioglu M, ***Gautam G**, M. Zhang, and W. Yuan, "AC transport loss analysis of HTS stack busbars for all-electric aircraft with harmonics and DC offset considerations," Superconductor Science and Technology, vol. 37, no. 7, p. 075021, Jun. 2024, doi: 10.1088/1361-6668/ad558c.

*Publications related to this thesis

2

Introduction of high temperature superconductivity

2.1 Introduction

At the beginning of the 20th century, Heike Kamerlingh Onnes measured the electrical resistance of various materials when cooled to very low temperatures. In 1911, the Dutch scientist made a groundbreaking discovery when he found that the resistance of mercury dropped to zero at temperatures below 4.2 K [29], marking the first observation of superconductivity. This phenomenon, where electrical resistance vanishes, led to the classification of materials exhibiting such behaviour as superconductors. Onnes coined the term "superconductivity" to describe this remarkable property observed in certain materials. In subsequent years, it was revealed that numerous materials could attain the superconducting state when cooled to sufficiently low temperatures [2]. Researchers also identified new materials that exhibited superconductivity at slightly higher temperatures. However, it appeared that superconductivity was typically limited to temperatures below 30 K [30].

Following extensive research on superconductivity across the periodic table's metals and the subsequent disappointment due to the low critical temperatures (Tc) encountered, researchers shifted their focus to investigating alloys and compounds. This shift led to the

8

discovery of superconductivity in a significant number of these materials. However, these new superconductors exhibited unusual behaviour; unlike pure metals, they did not demonstrate perfect diamagnetism but showed partial flux penetration. Initially, this was considered to be a possibe experimental error or the result of impurities. Nevertheless, in 1957, Abrikosov introduced the concept of a new category of superconductors [31], now known as type II superconductors. The field underwent a transformative change in 1986 with the discovery by Bednorz and Müller of a novel class of superconductors [32]. Following this breakthrough, a plethora of materials were identified that exhibited superconductivity at temperatures around 90 K [33]. These materials, which could not be fully explained by existing theories, were classified as high-temperature superconductors (HTS) to distinguish them from the traditional low-temperature superconductors (LTS).

A century after superconductivity was first identified, the search for new superconductors continues to yield results. Examples include the discovery of magnesium diboride (MgB2) in 2001 [34], iron-based superconductors in 2006—which achieved critical temperatures above 55 K [35, 36, 37] from 2008 onwards—and hydrogen sulphide (H2S) in 2015 [38], which exhibits superconductivity at 203 K under high pressure. More recently, in 2019 [39], lanthanum hydride (LaH10) was found to become superconducting at a temperature of 250 K when subjected to high pressures.

2.2 Threshold criteria for superconductivity

The superconducting state of a material is constrained by three critical parameters: transport critical current density (J_c), critical temperature (T_c) and critical magnetic field (B_c). If any of the parameters exceed their critical limits, the material transitions from the superconducting state to the normal state, as illustrated in figure 2.1.
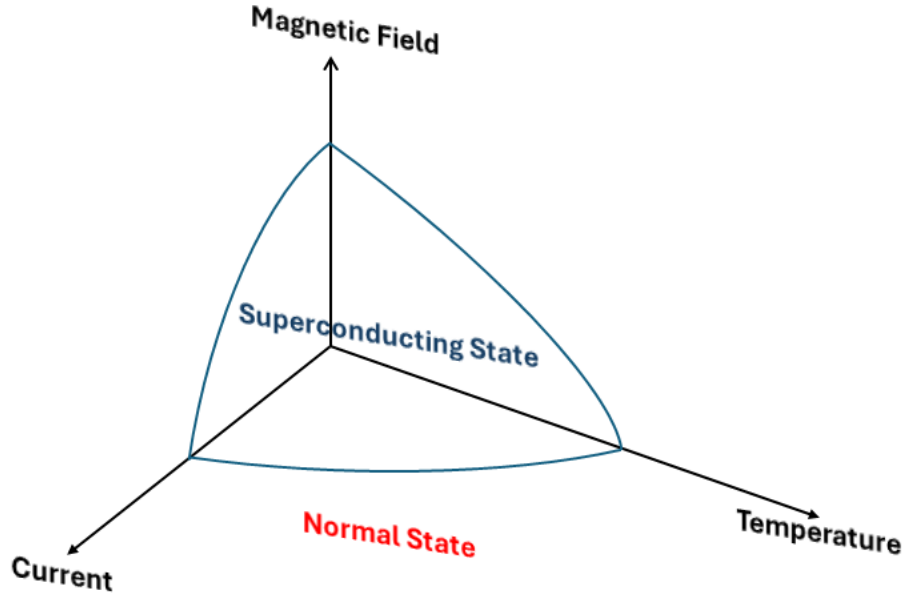
Figure 2.1: Diagram of the boundary surface distinguishing the superconducting state from the normal state within the coordinates defined by temperature, magnetic field, and current [1].

2.2.1 Transport critical current density

The critical current is the maximum current a superconductor can safely carry, and it is defined by an electric field threshold value. For HTS, the electric field threshold (E_c) is $(1\mu V/cm)$, as shown in figure 2.2. Transition of a superconductor to the normal conducting state typically generates an electric field that is described by power law through equation (2.1) [40].

$$E = E_c \left(\frac{I}{I_c} \right)^n \tag{2.1}$$

Where, I is the current flowing through superconductor, n represents resistive transition index (n = 21 is used in the modeling), and E_c stands for the electric field applied to establish the critical current I_c.
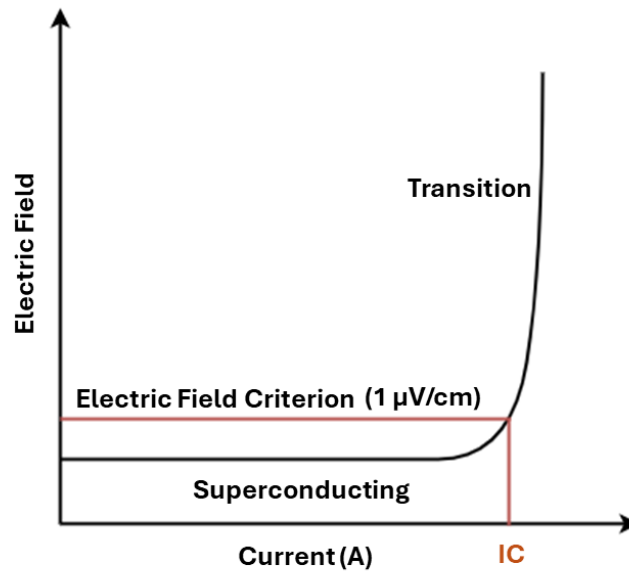
Figure 2.2: Electrical Field-Current Relationship in High-Temperature Superconductors (HTS), indicating the critical current threshold at an electrical field of 1 μV/cm [1].

2.2.2 Critical temperature

At temperatures below a specific threshold, known as T_c, the electrical resistance of a superconductor drops to zero. This threshold is referred to as the critical temperature. The electrical resistance of a superconductor as a function of temperature is shown in figure 2.3. The transition of superconducting state to normal state is steep, change in temperature required for transition is ΔT_c ($\Delta T_c = T_c(90\%) - T_c(10\%)$). Upon reaching the transition temperature, a significant increase in resistance, by several orders of magnitude, is usually noted. Although it is not possible to experimentally demonstrate that resistance in the superconducting state is absolutely zero, for all practical purposes, it is considered to be zero below Tc [41].

2.2.3 Critical magnetic field

The superconducting state is also influenced by external magnetic fields. A magnetic phase diagram helps explain the behaviour of a superconductor under an external magnetic field. figure 2.4 illustrates the magnetic phase diagram of type-I and type-II superconductors. In a

11
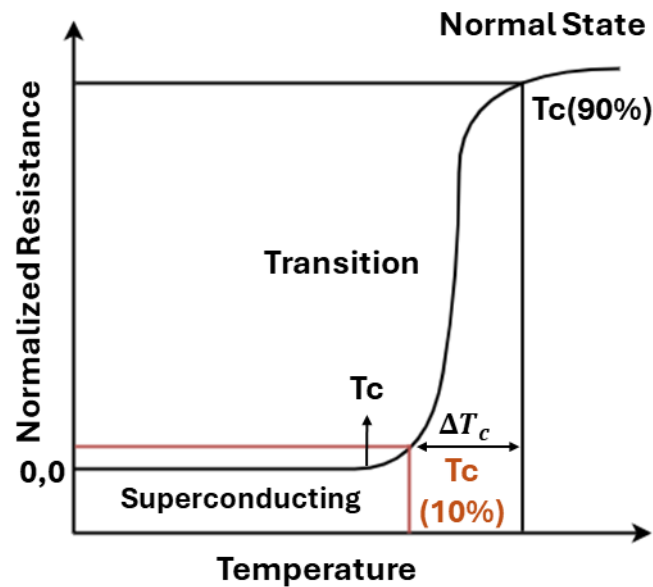
Figure 2.3: The electrical resistance of a superconductor is temperature dependent. ΔT_c is the difference between critical temperatures at 90% and 10%, shows a steep transition from the superconducting state to the normal state [1].

type-I superconductor, only one critical field exists, and below this field, the superconductor is in a superconducting state. In contrast, type-II superconductors exhibit two different states simultaneously. Type-II superconductors behave like perfect diamagnets below the lower critical field B_{c1}. Beyond B_{c1}, the superconductor enters a mixed state and remains superconducting until the upper critical field B_{c2}. Type-II superconductors can carry current even under such high magnetic fields, making them technologically important; they are also called technical superconductors [42, 41, 2]. In type-II superconductor, between lower critical field B_{c1} and upper critical field B_{c2} exhibits a different state called mixed state, in this state there is a partial penetration of flux. To lower the overall magnetic energy, the superconducting material allows the flux bundles to penetrate the material. Even material is partially penetrated the superconducting material is still possessing it's superconducting state. This property of type-II superconductors makes them operate in a high magnetic field which makes them stutable for large scale applications, such as cable or magnets.

12
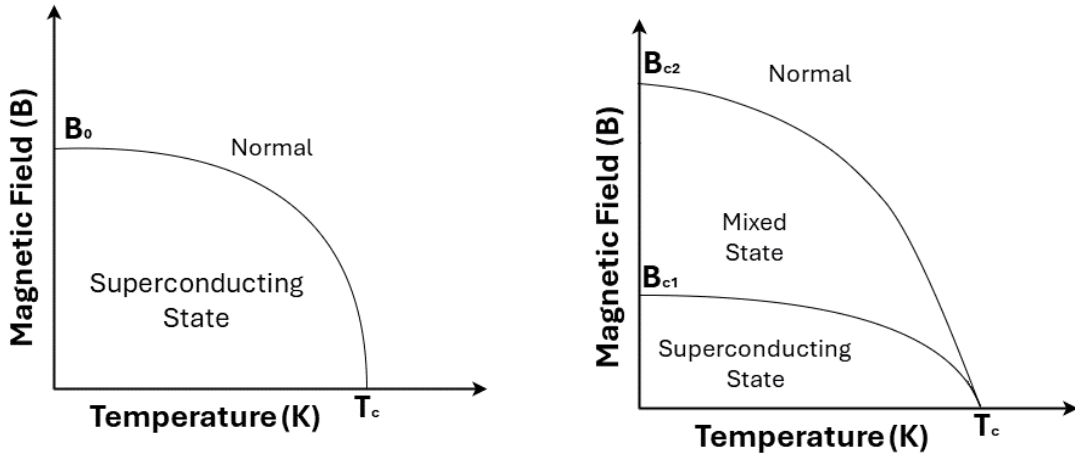
(a) Type-I superconductors possess a single criti- cal field, B_0. Below this field, they exhibit super- conducting properties; above it, they transition to a normal state.

(b) Type-II superconductor is in superconducting state below B_{c1}, enter into mixed state and re- mains superconducting in the mixed state, and becomes normal above B_{c2}.

Figure 2.4: Magnetic phase diagram of type–I and type–II superconductors [2].

2.3 Current flow in the mixed state and magnetization of type-II superconductors

2.3.1 Current dynamics in the mixed state

In type-II superconductors, the mixed state occurs between the lower critical field B_{c1} and the upper critical field B_{c2}, as shown in figure 2.5. The superconductor enters the mixed state due to an increase in the external magnetic field B_a, which exceeds the lower critical field. In the mixed state, flux lines carrying a unit quantum of flux, $\Phi_0 = (h/2e)$, and parallel to the applied field, penetrate the superconductor material. These flux lines form a normal core with a diameter on the order of 2ξ, and the radius of the circulating current is equal to the penetration depth, λ. The optimal arrangement for these normal cores penetrating the superconductor in a cylindrical shape with the highest surface-to-volume ratio, aligned parallel to the applied magnetic field. Each flux line originates from a vortex of persistent current that rotates in the opposite direction to the surface screening current [43]. As the

13
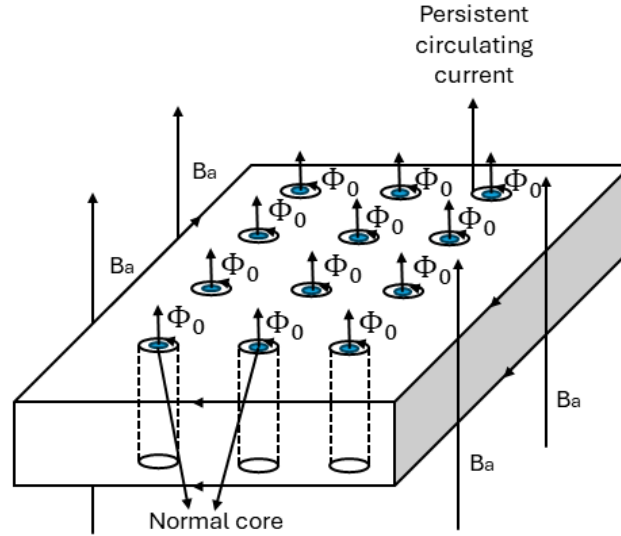
Figure 2.5: In the range between B_{c1} and B_{c2}, a type II superconductor enters a mixed state where the material is penetrated by flux lines Φ_0, created by vortices of persistent current [2].

applied field (B_a) increases, the density of normal cores rises, reducing the superconducting volume fraction until, at the upper critical field B_{c2}, the superconducting structure collapses, turning the superconducting material to normal.

In mixed state, the current J flows through the superconductor without being affected by the flux lines as size of core (2ξ) is very small. The vortices repel each other, keeping the normal cores confined to a small area, allowing the current to pass unobstructed as long as it doesn't disturb the vortices. Current pass through the superconductor seamlessly until flux lines subject to Lorentz force F_L, due to the transport current (J) and a perpendicular field [43, 44, 45], as shown in figure 2.6. Lorentz force acting on vortex can be calculated with:

$$F_L = J \times \Phi_0 \tag{2.2}$$

The movement of flux lines produces a measurable voltage, introducing resistance. However, the crystal lattice counters this movement with a pinning force, F_P. To enhance this force, imperfections, defects, and impurities are introduced into the superconductor, creating more pinning sites and significantly boosting the pinning force. This allows the superconduc-

tor can handle a much higher current. The flux lines remain stationary until the Lorentz force equals the pinning force, occurring at a specific current density known as the critical current density, J_c. Surpassing J_c causes the flux lines to move, generating voltage and transitioning the material to a normal state.
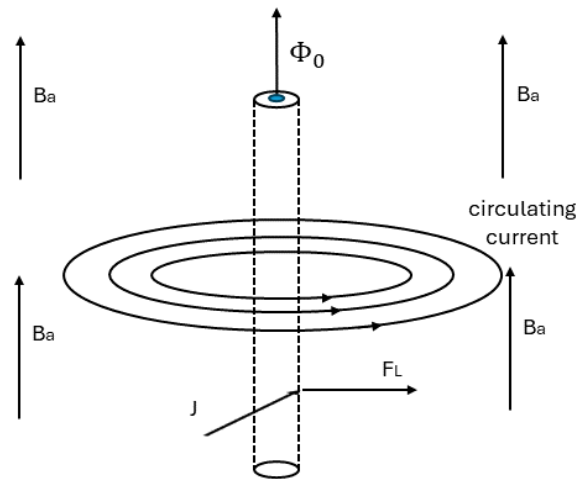
Figure 2.6: The structure of a single vortex, experienced Lorentz force F_L due to transport current [3].

2.3.2   Magnetization in type-II superconductor

Type II superconductors behave like type-I superconductors when subjected to magnetic fields below the lower critical threshold, known as B_{c1}. In this state, they manifest the characteristics of a perfect diamagnet. This perfect diamagnetic state persists until the system encounters the lower critical field, B_{c1}. Beyond this critical juncture, the superconductor transitions into the mixed state, characterized by the penetration of flux lines into the superconductor, marking a transition from the zero magnetic flux state in figure 2.7a. As the external magnetic field is gradually increased from B_{c1}, the superconductor experiences an increase in magnetic flux density. This process continues until the magnetic field reaches another critical point, B_{c2}. At this upper critical field, the superconductor is completely penetrated, transition into the

normal state.
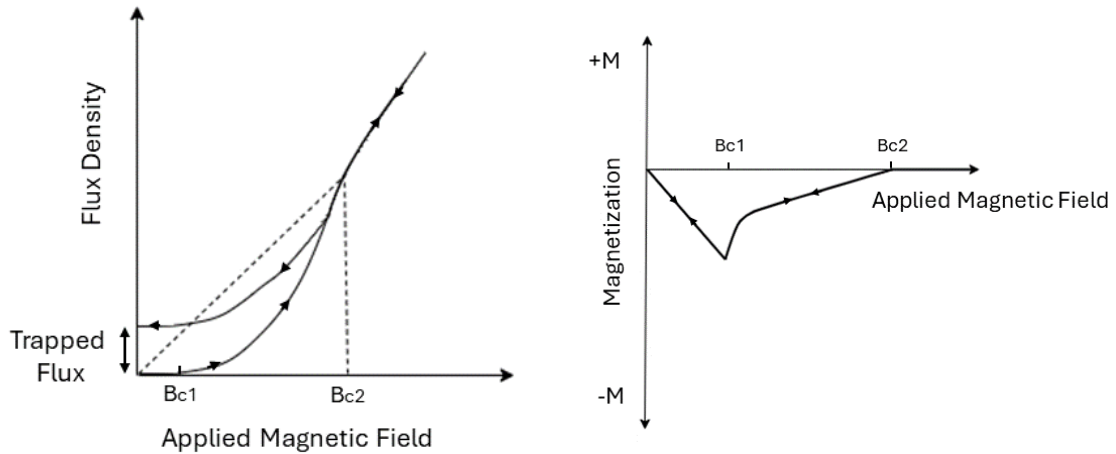
(a) Type II superconductors, magnetic flux density stays zero until B_{c1}, then increasing after B_{c1}, fully penetrating the material at B_{c2}.

(b) Magnetization decreases with increasing magnetic field, reaching a peak at B_{c1}, and then drops to zero by B_{c2}. Both processes are reversible in pure, ideal materials.

Figure 2.7: Magnetization phenomena in perfect type-II superconductors [2].

Interestingly, in an ideal, or pure, superconductor, the transition curve that describes the relationship between magnetization and applied magnetic field retraces its steps in the reverse direction, illustrating a symmetrical behaviour. This phenomenon and the corresponding magnetization versus magnetic field relationship are depicted in figure 2.7b. Here, it is shown that the magnetization of the superconductor increases in response to the magnetic field up until the lower critical field, B_{c1}. Beyond this point, as the field strength surpasses B_{c1}, magnetization begins decrease; a trend that persists until magnetization becomes 0 at the upper critical field, B_{c2} [2].

The density of flux lines within the superconductor is balanced by the reduction in free energy and the mutual repulsion between vortices. As the applied magnetic field continues to rise, the normal cores are forced closer together, increasing in the average magnetic flux density within the superconductor while simultaneously causing a reduction in its overall magnetisation. This dynamic culminates at B_{c2}, where a discontinuous change in the slope of both the flux density and the magnetization curve is observed. At this point, the superconductor losses its superconducting properties entirely, transitioning into a normal state. In this state,

the flux density aligns with $\mu_0 B_a$, and the magnetization effectively drops to zero, marking a stark transformation that underscores the complex interplay between magnetic fields and superconducting materials.

2.3.3 Irreversible Magnetization

In type-II superconductors with pinning imperfections, magnetisation behaviour is irreversible as shown in figure 2.8 [46, 47]. Unlike type-II pure superconductor whose magnetisation behaviour is reversible, as shown in figure 2.7. Magnetic irreversibility in type-II superconductors occurs because flux lines, or normal cores, are immobilised within the material through pinning by imperfections, preventing free movement of the flux lines. This immobilization means that upon increasing the field from zero, flux does not suddenly penetrate the material at B_{c1}, leading to a smoothing effect in the flux density and magnetization curves around B_{c1}. Similarly, when the field is decreased from above B_{c2}, the curves exhibit hysteresis instead of retracing their initial paths, indicating that some flux lines remain permanently trapped, as shown in figure 2.8a. This trapped flux is due to the pinning by imperfections such as dislocations, grain boundaries, and impurities. To reduce the magnetisation M to zero, the magnetic field must be reversed; however, achieving a state at $B = 0$ without any trapped flux requires heating the material to its normal state. These imperfections due to pinning helps to increase the critical current of the superconductor and make them useful for high current application.

2.3.4 Critical state model of type-II superconductors and Magnetization

Critical state models calculate the magnetisation curve for type-II superconductors. When a type-II superconductor experiences a field above the critical field, B_{c1}, it enters a mixed state, and supercurrent penetrates the surface of the superconductor. The critical state model assumes that the current penetrates the superconductor with a current density equal to the critical current density, J_c. The region of the superconductor that is penetrated is in a critical state with a current density $J = J_c$. In the critical state, there is no flux flow, and the flux
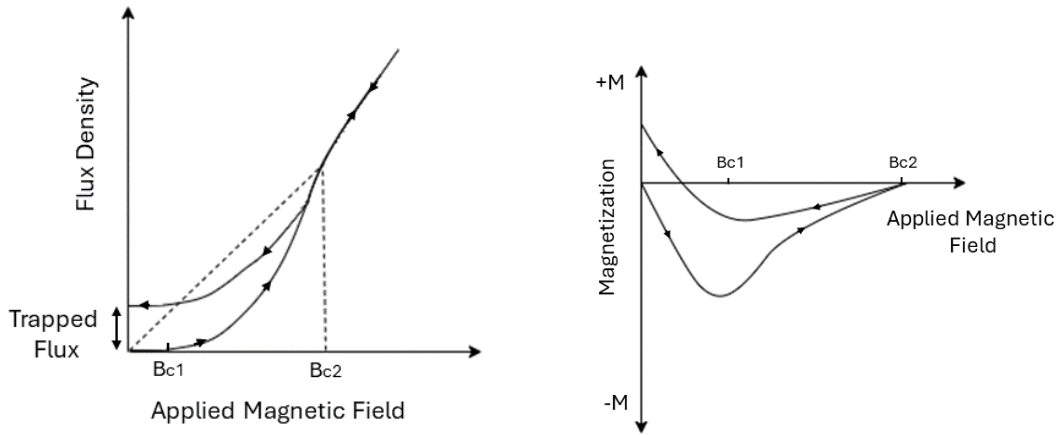
(a) A practical type-II superconductor, due to imperfections, exhibits magnetic irreversibility in its flux density.

(b) In a real type-II superconductor, the material remains magnetized even after the field is reduced to zero.

Figure 2.8: Magnetic irreversibly phenomena in imperfect type-II superconductors [2].

lines are in equilibrium. However, in practical, changes in the magnetic field are very slow, and the sample can be considered in a quasi-equilibrium state. Thus, a sufficiently accurate magnetization curve can be calculated using the critical state model. Two critical states models are used to calculate magnetization in type-II superconductor's: Bean's model and Kim's model.

Bean's model

Bean's theory was the first phenomenological theory of magnetization [48, 49]. In Bean's model, it is assumed that the critical current density doesn't depend on the magnetic field. To simplify calculations, Bean adopted the Mendelssohn sponge model [50]. In this model, the mesh is made up of filaments whose diameter is smaller than the London penetration depth. Supercurrent sustains in these filaments up to J_c (critical current density), J_c is a function of magnetic field, and $J_c = 0$, at critical field of filament. The sponge model portrays a highly interconnected internal structure of material with a high critical field, surrounded by a matrix of soft superconductor possessing a low critical magnetic field B_c. Bean derived the magnetization curve for an unaltered hard superconductor cylinder with radius R in a

magnetic field aligned with the axis. This was achieved by determining the internal field, B_i, as a function of external field, B_e, and the position of the superconductor.

$$4\pi M = \frac{\int_0^v (B_i - B)dv}{\int_0^v dv} \tag{2.3}$$

where, volume of sample is v. If radius R is much larger than penetration depth there will be full shielding for field less than B_c, as shown in equation (2.4)

$$B_i = 0, 0 \leq r \leq R and 0 \leq B \leq B_c \tag{2.4}$$

If the background field increases from B_c, the soft superconductor becomes normal which is surrounded by filaments. At higher field strengths, shielding currents are generated in the filaments, and penetrated into the filaments with a penetration depth D_p, as determined by the of Ampere's circuital law.

$$D_p = 10(B - B_c)/4\pi J_c \tag{2.5}$$

Bean's critical finding is that the magnetisation in hard superconductor depends on macroscopic dimension of the sample.

Kim model

Kim *et al.* model represents a more realistic and generalized form of Bean's critical state model; it assumes that the critical current is determined by the local field in the region [51]. As the background field increases, circulating currents begin to generate on the surface of the superconductor to oppose the field. A further increase in background field causes currents to start penetrating the superconductor surface and enters in critical state, and any further increase in field reduces the critical current density. Thus, the critical current density is function of local magnetic field, and $J_c(B)$ can be used to determine state of magnetization. $J_c(B)$ can be defined with the equation (2.6) [52, 53].

$$J_c(B) = \frac{J_{c0}}{1 + \frac{B}{B_0}} \tag{2.6}$$

where, J_{c0} is critical current density during absence of field, and B_0 is constant.

An additional noteworthy finding of the Kim model is that the Lorentz force plays a significant role in determining the critical current density and can be understand with equation (2.8).

$$\alpha(T) = J_{cr}(B + B_0) \tag{2.7}$$

where, $\alpha(T)$ and B_0 are constants. (T), strongly depends upon temperature and in hard superconductor current decays slowly, makes Anderson to propose theory of 'flux creep'.

2.3.5   Flux creep

Flux creep theory, developed by Anderson, builds on Bean's critical state model and Kim's modified model. Anderson's model says that when the critical current J and field B exceed their respective critical values, flux bundles begin to leak through the superconducting material, causing it to return to the critical state. This movement of flux bundles is known as "flux creep" [54]. Anderson's theory describes flux creep as a thermally activated process driven by the Lorentz and pinning forces ($J \times B$). Flux creep leads to the generation of longitudinal resistive voltages within the conductor, a phenomenon caused by the drifting of flux bundles when current flows through the material. As these flux bundles move, they create a resistive voltage along the length of the conductor. This resistive voltage is directly proportional to the average creep velocity of the flux bundles, meaning that as the speed of the flux bundle movement increases, so does the resistive voltage.

Anderson's theory provides a detailed explanation of the significant variation in the critical current density (Jc) with temperature, particularly in the range of 0.5–0.1 Tc. According to this theory, flux bundles within the superconducting material are hindered in their movement by energy barriers at the pinning centers, also known as potential wells. When an external

magnetic field is applied, the flux density within the material does not remain uniform due to the presence of these pinning centers. In the presence of a transport current, the Lorentz force acts on the flux bundles, modifying the local free energy landscape. This force effectively tilts the energy barriers in a 'downhill' direction, creating a 'staircase' pattern in the barrier structure. Consequently, the energy required for the flux bundles to move decreases in specific directions, facilitating their movement. At finite temperatures below the critical temperature (Tc), thermal excitation allows the flux bundles to overcome these barriers. The thermal energy provides the necessary activation energy for the flux bundles to jump over the potential wells. This process occurs at a certain rate, which is influenced by the temperature and the strength of the pinning centers. The rate at which flux bundle jumps is

$$v = V_0 e^{[-U(B,T,J)/k_B T]} \tag{2.8}$$

here is equation (2.8), V_0 is flux bundle characteristic frequency assumed to be $10^5 - 10^{11} s^{-1}$ and U(B, T, J) is activation free energy.

2.4 Conclusion

This chapter provides a comprehensive foundation in the fundamental knowledge of superconductors, covering both basic superconductivity principles and macroscopic electromagnetic theories for type-I and type-II superconducting materials. It delves into the mixed state in type-II superconductors, discussing characteristic lengths, basic vortex dynamics, and pinning forces that are crucial for understanding their behaviour. Additionally, the chapter compares the properties of high-temperature superconductors (HTS) and low-temperature superconductors (LTS), outlining their different critical temperatures and critical current densities, and emphasizing the importance of these properties for various applications. Furthermore, the chapter highlights the various critical temperatures and critical current densities of these materials, underscoring their significance in diverse applications. This foundational knowledge sets the stage for the subsequent chapters, which will focus more specifically on type-II

superconductors. These materials are extensively used in energy storage, power transmission, and medical imaging due to their superior properties. The following chapters will provide an in-depth exploration of type-II superconductors, elaborating on macroscopic electromagnetic theories such as flux creep, flux flow, and critical state models including the Bean and Kim models. These theories are crucial for understanding the practical performance and applications of type-II superconductors. This chapter has laid the groundwork by presenting essential concepts and theories related to superconductors. The detailed discussion on both HTS and LTS properties, as well as the introduction to the behavior of type-II superconductors, is vital for comprehending the advanced topics that will be explored in the rest of the thesis. By summarizing the key takeaways, this chapter underscores the importance of the presented knowledge as a foundation for understanding the more complex phenomena and applications discussed in the subsequent chapters.

3

State of the art of ReBCO tapes for high current applications

3.1   Introduction

ReBCO (rare earth barium copper oxide), represents a class of high-temperature superconductors (HTS) [55], characterized by the general formula $REB_{a2}C_{u3}O_{\delta}$, where RE stands for a rare earth element, (such as Yttrium [56], Y, or other rare earth elements like Gadolinium, Gd [2]). These materials are distinguished by their ability to conduct electricity without resistance at temperatures significantly higher than those required by conventional superconductors, typically above the boiling point of liquid nitrogen (-196°C or 77K), making them more feasible for practical applications. ReBCO superconductors are part of the second generation (2G) of high-temperature superconducting materials. They are known for their high critical temperature (T_c), high critical magnetic field (B_c), and high critical current density (J_c), which remain robust even under strong magnetic fields. These properties are crucial for applications requiring high current capacity and high magnetic field operations, such as magnetic resonance imaging (MRI), particle accelerators, and power transmission lines and cables. Due to their importance in technical applications, such superconductors are also called technical superconductors, which are used in large-scale applications.
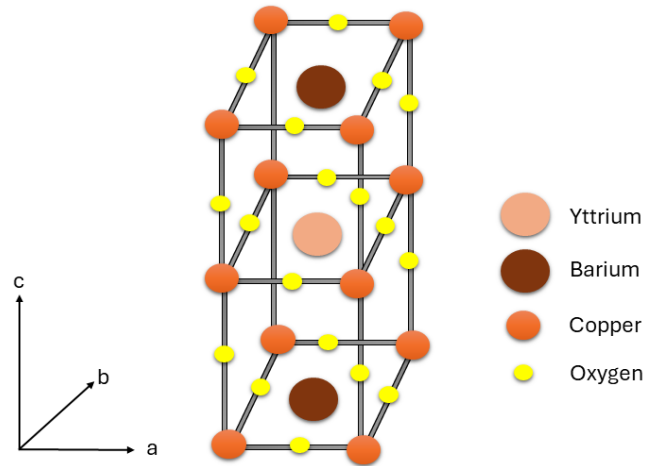
Figure 3.1: Crystal structure of YBCO unit cell [2].

The crystal structure of the YBCO unit cell is shown in figure 3.1. Supercurrent flows within the copper oxide planes of the YBCO crystal and is restricted in the direction perpendicular to these planes, leading to anisotropic electrical current transport characteristics in the superconducting state [57].

3.2   ReBCO tape structure and properties

In polycrystalline ReBCO materials, the ability of superconducting currents to pass from one grain to another is significantly influenced by the angle of the grain boundaries, with current transfer decreasing exponentially as misalignment increases [57]. To mitigate grain misalignment, ReBCO layers are grown on a textured substrate. However, during the growth of the ReBCO layer, defects will unavoidably form, reducing the number of well-aligned grains as the layer's thickness increases. Consequently, the thickness of the ReBCO layer is typically limited to a few microns. To maximise the area available for ReBCO growth, the flat tape geometry has been developed and is now the standard for long-length ReBCO wires.

The structure of ReBCO tape is shown in figure 3.2 and consists of five different layers. A stabilizer surrounds a typical ReBCO tape, providing an additional path for current during transients and aiding in thermal stabilization. The stabilizer layer is generally made up of
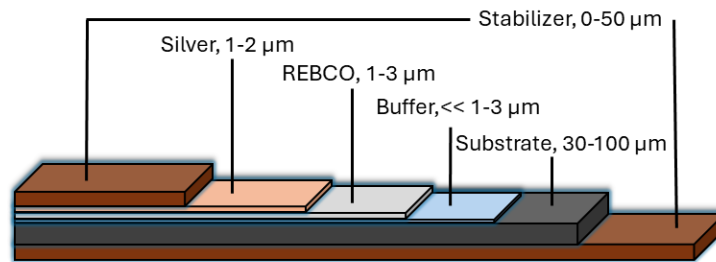
Figure 3.2: Schematic illustration of a standard ReBCO coated conductor tape. The thickness of each layer varies among different manufacturers [4].

metal, which can be copper or steel, depending upon the manufacturer. This outer layer of ReBCO tape also facilitates the soldering of one tape to another and provides armour to the tape. Following the stabilizer is a silver layer that serves as the first layer of protection, offering chemical protection and adjusting the oxygen content in the crystal. Positioned next to the silver layer is the ReBCO layer, which is the superconducting layer responsible for carrying supercurrent. The buffer layer is adjacent to the superconducting layer, separating it from the substrate and providing texture for the ReBCO layer. As current density depends upon the grain boundary angle [58], the substrate helps to keep the angle below $5°$ to enhance the critical current density J_c [59]. Additionally, the substrate layer provides mechanical strength to the tape. More than a dozen companies manufacture and supply ReBCO tapes listed in table 3.1. ReBCO tapes with a range of critical currents from $60A/cm$ to $400A/cm$ are available in the market.

3.2.1 Degradation of critical current in ReBCO tape

Due to ReBCO tape's brittle ceramic structure, ReBCO tapes are fragile and susceptible to critical current degradation when exposed to mechanical forces and high temperatures. How critical current is affected due to mechanical forces and high temperature is explained here:

Effect of mechanical forces: The critical current of ReBCO tape depends on stress; the critical current degrades as stress increases. When multiple tapes are grouped together, stress is exacerbated due to imperfections in the ReBCO tapes. This stress can damage the crystal

Table 3.1: List of companies that manufacture ReBCO, normalized critical current at 77K [5].

Manufacturer	Critical Current / width (A/cm)	Reference
SuperOx	400	[60]
Theva	400	[61]
Bruker HTS	100	[62]
SuperPower	400	[63]
SuNAM	400	[64]
Fujikura	400	[65]
Shanghai Superconductor	300	[66]
American Superconductor	300	[67]
Superconductor Technologies	300	[66]
Deutsche Nanoschicht	300	[68]
Oxolutia	60	[69]
Shanghai Creative Superconductor Tech.	170	[70]
MetOx	300	[71]
SWCC Showa Cable Systems	350	[70]

structure and degrade the critical current. The maximum degradation in the critical current of HTS tapes occurs at the tape's edges. ReBCO tape can withstand stress in the axial direction up to 700 MPa and in the transverse direction, it can endure stress ranging from 20 to 100 MPa [72]. Three techniques of grouping multiple HTS tapes for high-current transmission applications are discussed later in this chapter to reduce the effect of mechanical stress during grouping multiple tapes.

Effect of high temperature: ReBCO tapes can be damaged and lose their superconducting properties when subjected to high temperatures. If a ReBCO tape is exposed to $230°C$ for more than 30 minutes, after 30 minutes there is a 10% degradation of critical current. Similar conditions in vacuum cause degradation in critical current by 30% [73]. In ReBCO (ReBa2Cu3O7x) materials, the superconducting behaviour is primarily observed in the CuO planes, attributed to their distinct crystal arrangement. The composition, especially the balance of copper and oxygen within the structure, plays a pivotal role. Exposing a ReBCO conductor to temperatures exceeding $150°C$ can cause oxygen to leach out through the grain boundaries, adversely affecting its superconducting attributes. When the temperature rises above $250°C$, oxygen begins to exit from the crystal framework itself, leading to rapid deterioration [74].

3.3   Advantages of ReBCO for high current transmission

REBCO tapes have been used for many pilot projects around the world for direct current transmission [75, 76, 77, 78, 79, 80, 81, 82, 83, 84]. The advantages of using REBCO tapes for high-current transmission are discussed.

High current density: ReBCO superconductors are also known as technical superconductors due to their potential for use in large-scale applications such as magnets and cables. This is due to their high current density; for instance, a single ReBCO tape can have a current density up to 400 A/mm^2 at 77K, as shown in table 3.1. Furthermore, reducing the operating temperature can further increase the current densities of ReBCO tapes. Compared to conventional copper busbars which have a current density of nearly 2-3 A/mm^2 [85], ReBCO offers significantly high current densities with less space and weight [86]. These advantages make ReBCO suitable for high-current applications such as in data centres, electric aircraft, and industrial electrolysis.

High critical temperature: ReBCO exhibits superconductivity at high temperatures compared to other superconductors such as MgB_2. These temperatures can be achieved with LN_2 based cooling systems. LN_2 is inexpensive compared to other liquefied gases

like hydrogen and also less complex to work with. A simple two-walled vacuum cryostat is sufficient for the operation.

Zero resistance: In a conventional copper busbar system, the resistance increases with the current flowing through the busbar. On the other hand, superconducting transmission systems exhibit zero losses when carrying DC. Additionally, these superconducting transmission systems feature a low-voltage drop, making them attractive solutions for low-voltage network systems such as in electric aircraft and data centres [87]. The benefits of lower losses and low voltage drop make these systems particularly attractive for railway systems. For instance, the Tokyo railway system requires substations at intervals of every 2-3 km [88]. A superconducting transmission system could significantly reduce the number of substations.

3.4 ReBCO superconductor: A high current transmission approach

The critical current of a superconductor is limited to a few hundred amps. To achieve the desired high current tens or hundreds of ReBCO tapes must be grouped or connected in parallel. Grouping ReBCO tapes is complicated as the geometry of the tape is flat and the critical current of the tape depends upon strain. Techniques used for grouping or cabling are explained here:

3.4.1 Co-axial winding technique

In the co-axial winding technique, ReBCO tapes are wound around a core at a lay angle α. The flat surface of the tape is used to wrap around the central core diameter (d) with a lead (l). The lay angle, which is the angle between the centre of the core and the ReBCO tape, can be calculated as:

$$\alpha = tan^{-1}\left(\frac{\pi d}{l}\right) \tag{3.1}$$
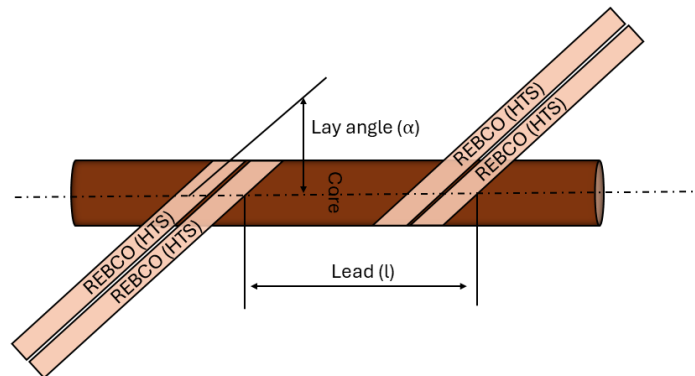
Figure 3.3: Schematic of co-axial (CORC) winding concept [5].

This technique allows for two different cabling approaches. The lay angle depends on the size of the core: a larger core results in a smaller lay angle, while a smaller core leads to a larger lay angle. Kim et al. developed a power cable using the first approach with a large core and small lay angle approach, where the core diameter is d = 35 mm and the lay angle $\alpha = 15°$ [89]. Conversely, van et al. adopted a second approach with a small core and a high lay angle, where the core diameter is d = 5 mm and the lay angle $\alpha = 30°$ [90].

The first approach is used in many pilot projects for AC and DC transmission cables [91, 92, 93, 94, 95, 96]. To minimize the effect of self-field on critical current ReBCO tapes are roughly aligned with cable self-field.

The second approach, developed by Advanced Conductor Technologies (ACT), is named CORC (Conductor on Round Core). Multiple ReBCO tapes are wound on each other over a small core with alternating lay angles to carry high currents. The use of a small core necessitates high lay angles in the cable, which offer minimal bending radii and minimal degradation [90]. CORC cables are among the few high-current conductors commercially available and are attractive options for magnet applications [97]. One disadvantage of this cabling technique is that more than a meter of ReBCO tape is required for a meter-long cable due to the lay angle. The amount of ReBCO tape needed for a given cable length can be calculated as follows:

Figure 3.4: Schematic of Roebel cable consists of 3 tapes [6].

$$L_{ReBCO} = \frac{L_{cable}}{cos\alpha} \tag{3.2}$$

Here in equation (3.2), L_{ReBCO} is the length of the required ReBCO tape, L_{cable}, is the length of the cable, and α, is the lay angle on the core.

3.4.2 Roebel technique

The Roebel cabling technique, a century-old method, is used for creating low-loss cables. In 1997, Martin Wilson first proposed the idea of using the Roebel structure with ReBCO tapes [98]. Siemens then demonstrated the first ReBCO-based Roebel cable, which, as expected, reduced AC losses compared to the stacked concept but also decreased the critical current due to self-field effects [99]. Researchers from the Karlsruhe Institute of Technology (KIT) have developed some advanced Roebel cable designs, and the design process can be found in [6]. The Roebel technique allows for several tapes to be grouped together with a portion of each tape punched out. The geometry of the cable, shown in figure 3.4. The geometry of the Roebel cable offers favourable alignment to the external magnetic field and has good bend ability around the flat side [100].

However, designing cables with the Roebel technique also has disadvantages. The punching process results in material loss, making it costly due to the high price of ReBCO tapes. The edges of the cable can experience degradation from stress, rendering them unsuitable for applications where the cable must operate in a high-stress environment. For high-current applications, the Roebel technique may not be advantageous as scaling up is limited because only a limited number of tapes can fit within one twist pitch [6].
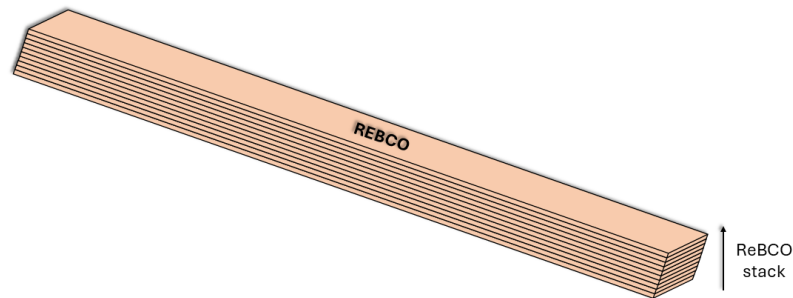
Figure 3.5: Schematic of stack concept which consists of 10 tapes.

3.4.3   Stack technique

The stack technique involves stacking ReBCO tapes on top of each other, flat face to flat face. There are two approaches to implementing this stack concept. In the first approach, the tapes are layered until the desired critical current is achieved. This method is employed by the Japanese National Institute of Fusion Science (NIFS), as it can be easily scaled to very high currents. They have achieved 100kA at 20K with a 5T background field. The design consists of 10 mm wide, 54 ReBCO tapes, and utilizes three adjacent stacks with 18 ReBCO tapes each, with each tape having a critical current of 600 A at 77K in self-field. This prototype was built to demonstrate the feasibility of using the stack technique in a helical fusion reactor[101, 102]. Vision Electric Super Conductors (VESC), in collaboration with KIT, has also adopted this approach to develop a superconducting busbar for an aluminium electrolysis plant. Their superconducting busbar is designed to handle 20 kA of current at 77K. In their prototype design, they used two stacks of HTS tapes, with each stack containing 23 ReBCO tapes[103].

Massachusetts Institute of Technology (MIT) used the second approach of stack technique, in this approach, HTS (High-Temperature Superconductor) tapes are stacked and put inside of a casing to make a round-shaped conductor. Multiple such round-shaped conductors are put together to achieve the desired critical current. This technique was also used to make high-current cables for fusion applications. MIT researchers used this stacking approach, they twisted the stacks around its central axis, to decrease heat dissipation due to decrease in the

AC losses [104]. Swiss Plasma Center (SPC) also uses this approach of twisting ReBCO tape stacks for fusion magnets.

3.4.4 Comparison of stacking techniques

Although depending upon application each technique has its advantages and disadvantages, here the conceptual comparison is done based on bending, tape usage, and joints.

Bending: Bending occurs during cabling, typically with the flat side of the ReBCO tape being wound over a core. During bending, it is difficult to keep the flat surface of the tape in the plane, and it easily goes out of the plane. Bending reduces the critical current of the ReBCO tapes; typically, 95% of the critical current compared to an unbent ReBCO tape is used as a criterion for designing cables. The bending radii depend on the diameter of the core and the lay angle. The coaxial winding concept addresses the directional dependency of the bending radius. By varying the lay angle and lead, the minimum bending radius can be tailored to meet the specific requirements of the application. Conductor on Round Core (CORC) cable concept achieve minimum bending radii between 2.5 cm and 5 cm[97]. The Roebel technique has good out-of-plane bendability with bending radii of 2 cm [105]. The minimum bending radii can be achieved using the stack technique [106].

Tape usage: ReBCO tapes are expensive, so it is important to use the material efficiently in design applications. Nowadays, ReBCO tapes are more isotropic, and their relationship between magnetic field and critical current depends less on tape alignment compared to ReBCO tapes manufactured in the past which are strongly anisotropic. Apart from critical current, it is also very important to consider how much ReBCO tape is required for a unit length of strand design. An accurate estimation of the tape usage is required for an efficient design. For this factor estimation equation (3.3) can be used [58].

$$Factor = \frac{L_{tape}}{L_{strand}} \tag{3.3}$$

For the stack technique, this factor is 1, as the length of the tape and the length of the stack are the same. In terms of tape usage, the stack technique is very efficient, achieving

a unit length of tape that is the same as the unit length of the stack. For the coaxial and Roebel techniques, the unit length of the strand design is not the same as the unit length of the ReBCO tape. In the coaxial technique, the unit length of the strand design depends on the lay angle, whereas in the Roebel technique, it depends on the transposition.

Joints: ReBCO tape lengths are limited to a few meters, and depending on the application, there may be a need for $90°$ and $180°$ joints. Park et al. have demonstrated resistance-free joints in a laboratory environment with ReBCO tapes[107], but this process is not suitable for industrial scale production. The layers associated with the ReBCO tapes introduce resistance when joining tapes together; this resistance should be minimized. Soldering and welding-based methods have been used in the past for joining ReBCO HTS tapes. The stack technique has been implemented with several joint concepts, with resistance ranging from 1 to 100 $n\Omega$ [108, 109]. Jaakko et al. achieved a joint using the Roebel technique with a resistance range of 10 to 20 $n\Omega$ in the laboratory [110]. The coaxial technique poses significant challenges for implementing joints due to the difficult access to ReBCO tapes. In cases where multiple ReBCO tapes are wound over each other, accessing the tapes beneath the outer layers becomes difficult. For a 10-tape CORC cable, joints are implemented by cutting the tapes in a stair-step manner to access all the tapes, achieving a terminal resistance of 30 $n\Omega$ [111].

As outlined above, table 3.2 compares various techniques of cabling in terms of bending, tape usage, and joint capability. The stack technique offers a modular approach, enabling multiple tapes to be stacked to achieve a high critical current. In all-electric aircraft, the superconducting busbar is designed to carry the high currents required by the entire system. Due to the relatively short length of the busbar in such applications, twisting and bending are not necessary. This is advantageous, as the stack concept is not well-suited for handling bending. Since the power distribution system of all-electric aircraft does not demand extensive twisting or bending, the stack technique allows for efficient tape usage in busbar construction. Additionally, the busbar must accommodate joints to connect multiple sources and loads, and the stack concept provides excellent joint capability. For these reasons, the stack technique was selected for the design of the superconducting busbar prototype.

Table 3.2: Comparison of high current conductor technique based on bending, tape usage, and joints.

Technique	Bending	Tape usage	Joints
Co-axial	Good	Bad	Bad
Roebel	Average	Bad	Good
Stack	Bad	Good	Good

3.5   Conclusion

This chapter has provided a comprehensive overview of ReBCO tapes and their application in high-current scenarios. It explains that the challenges and limitations associated with using ReBCO tapes in high-current transmission systems, highlighting the technical and practical hurdles that must be addressed for successful implementation. The chapter explores various existing techniques for cabling ReBCO tapes, presenting a detailed discussion on the advantages and disadvantages of each method. A comparative analysis of these cabling techniques has been included to identify the most effective high-performance strategies. Furthermore, the chapter explains the specific cabling technique chosen for developing the prototypes in this thesis, along with the rationale behind this selection. Importantly, this chapter serves as a foundational platform for the research detailed in the following chapters of this thesis. The upcoming sections will focus on the design, prototyping, and characterization of a superconducting busbar utilizing ReBCO tapes.

4

Superconductivity for all-electric aircraft

4.1 Introduction:

Global CO_2 emissions from the aviation sector account for 2.4%, and this figure is expected to continue growing. The International Air Transport Association (IATA) has forecasted that over the next two decades, civil aviation will grow by 3.5% [112], as will emissions. The majority of CO_2 emissions (81%) come from passenger operations. Many organizations have prepared long-term roadmaps to reduce aviation emissions, such as Clean Sky [113], and Europe's Flightpath 2050 sets an ambitious goal to reduce CO_2 emissions by 75% and nitrogen oxide (NOx) emissions by 90%, with a 65% reduction in noise compared to aircraft in the year 2000 [114]. To achieve such goals, there is a need to reconsider and develop new technologies for future aircraft. Similar to other modes of transportation like road and sea, electrification can be used to achieve these targets.

In previous-generation aircraft, the electrical demand was only a few kW (kilowatts), typically consumed by cabin lights, galley loads, and so on. To increase reliability and reduce weight and fuel consumption, more electrification has been introduced in the new generation of aircraft, where pneumatic and hydraulic systems have been replaced by electric systems. This has increased the power consumption to hundreds of kW in aircraft now referred to as more-electric aircraft (MEA) [115]. The Airbus 380 and Boeing 787 are classified as

MEAs; they are more efficient, lighter, more reliable, and produce less noise compared to previous-generation aircraft. While MEAs set a new era in aviation, they are still not sufficient to achieve emission targets [116]. To meet the emission target, fuel-based propulsion systems must be replaced with electric propulsion systems [117].

4.2 Electrification in aircraft: role of superconductivity

Electrification in aircraft starts with subsystems and progresses to replacing traditional jet engines with electric propulsion systems. Electric aircraft can be categorized into three types based on the extent of onboard electrification [118, 119].

(1) More Electric Aircraft (MEA), where only traditional subsystems are replaced with electric subsystems, while the jet-propulsion system remains traditional.

(2) Hybrid electric aircraft (HEA), where jet engine produces the required power through an onboard generator. This generated electric power is used to provide thrust through propulsion units.

(3) All-electric aircraft (AEA), where a jet engine is replaced with an onboard source of power, which provides the required thrust through a propulsion unit.

Electrification in aircraft increases the onboard power requirement from kW to MW level [7]. Figure 4.1 shows the required power for different categories of aircraft. In the MW-level class of aircraft, several challenges need to be addressed such as power-to-weight ratio, compact system, low losses, and reliability. Traditional state of the art is not able to meet this criterion and there is a need for the non-conventional system to address such challenge. Superconductivity is a potential solution that provides a compact high power-to-weight ratio with low losses for MW-class power systems, which is essential for aircraft applications [120, 121, 122]. NASA N3-X is a turboelectric distributed propulsion (TeDP) concept whose entire system is supported by the superconducting systems, which includes, a superconducting power distribution system, and superconducting motors as propulsion units [123].
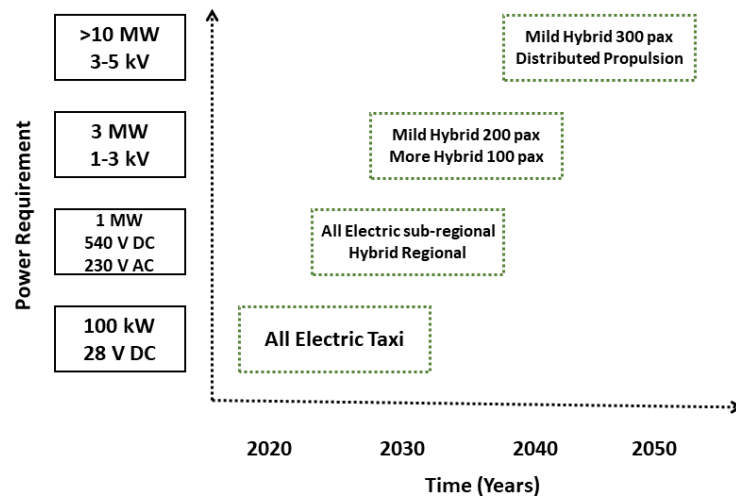
Figure 4.1: Anticipated power requirement for different categories of aircraft [7].

4.2.1 Power distribution system and voltage standards in aircraft

The current power distribution system of aircraft has accepted a maximum value of voltage is ±270 Vdc. This voltage level is a standard practice in aircraft power systems. The criteria for defining voltage standards are based on Paschen's Law, which determines the voltage at which electrical discharge or arcing will commence between two metal plates in the air, depending on the distance between the plates and the pressure. Typically, a minimum of 327 Vdc is required to cause a voltage breakdown for any given product of pressure and distance. Consequently, the voltage levels in aircraft power systems are maintained below 327 Vdc. A simplified schematic of the aircraft power distribution system is shown in figure 4.2.

The power system of aircraft adheres to the MIL-STD-704 standard, which defines the voltage level, frequency, power factor, phase, and ripple for both DC and AC systems. The AC power system consists of single and three-phase configurations with a grounded neutral system. Typically, a fixed 400 Hz system is used, but the standard also allows for a variable frequency and a double voltage system. A variable frequency system operates within a range of 360 to 800 Hz and uses a 115/200 V system. The double voltage system is equipped with 240/400 V at a nominal 400 Hz frequency. The AC system is regulated based on specific
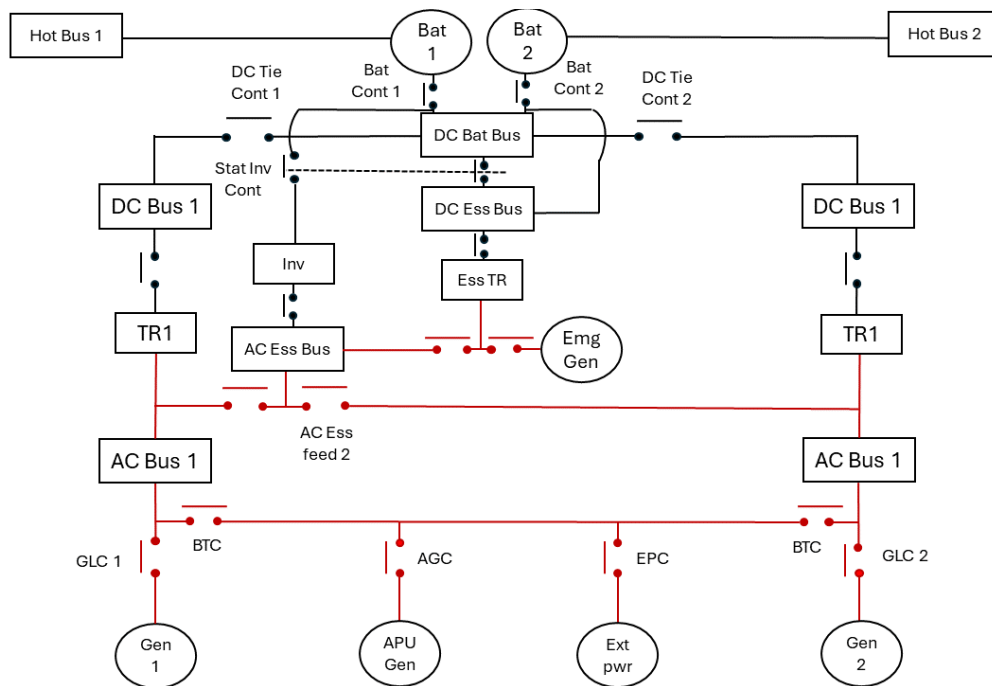
Figure 4.2: Schematic of aircraft electrical power system [8].

characteristics defined for both normal and abnormal operating conditions [123]:

- Steady-state voltage

- Power factor

- Voltage phase

- Distortion factor

- Crest factor

- Voltage unbalance

- Voltage modulation

- DC component

- Frequency modulation

- Transient peak voltage

- Steady-state frequency

- Voltage and frequency recovery time

DC power system also follows MIL-STD-704 standard, a two-wire system is used with a

28 or 270 V system. The characteristics used for DC system operation are:

- Steady-state voltage
- Voltage and frequency recovery time
- Transient voltage
- Distortion factor
- Distortion spectrum
- Ripple amplitude

4.2.2 Power distribution system of all-electric aircraft

For all-electric aircraft, the required power demand is significantly higher than that of conventional aircraft, often reaching the order of megawatts (MW). An example of a power distribution system architecture for an all-electric aircraft is shown in figure 4.3. As power demand increases, the voltage level also increases to reduce conductor weight. However, increasing the voltage level decreases the current level, but requires thicker insulation, which in turn increases the weight of the conductor. Conventional conductors are not suitable for such applications due to their low power-to-weight ratio and bulky size. In contrast, superconductors offer a high power-to-weight ratio and are compact in size. Superconductors operate at cryogenic temperatures, where voltage breakdown is a function of temperature. At lower temperatures, the breakdown voltage increases, potentially allowing for an increase in the voltage level in the electric aircraft power system.

In the CHEETA project, a hydrogen fuel cell-based propulsion system is proposed, featuring a drivetrain rated at 40 MW of power, with a voltage level of 1 kV and a current capacity of 40 kA [124]. The project compares three technical solutions for the aircraft power distribution system: Cuponal ($Cu_{0.15}Al_{0.85}$), Hyperconductor (Al 99.999%) and a superconductor-based system (YB_aCuo or MgB_2). Their analysis indicates that the superconductor solution is superior to the others in terms of weight, heat loss, and protection risk.
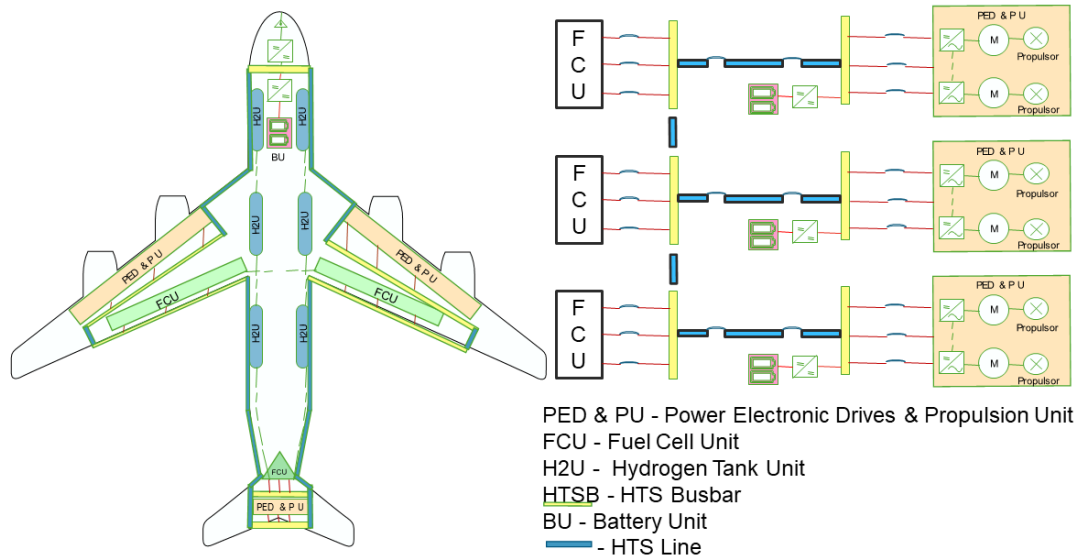
Figure 4.3: Example of an all-electric aircraft power distribution system with supporting components.

4.3 DC transmission through superconductors

DC transmission is highly efficient when using superconductors, especially with bulk power transmission [125]. DC transmission through superconductor offers almost no resistance compare to AC transmission. In AC transmission there are ac losses in the superconductor which makes the operation inefficient [126, 127]. Due to this several superconducting DC transmission systems have been installed worldwide, as shown in table 4.1. These superconducting transmission systems have current ratings ranging from 1 kA to 20 kA and voltage ratings from 1.3 kV to 80 kV. A list of the projects which ulitize HTS tapes to carry DC current is mentioned in table 4.1, most of these systems are cooled with liquid nitrogen and utilize YBCO and BSCCO materials to fabricate transmission cables. These projects demonstrate that bulk power transmission through superconductors offers a small carbon footprint with higher efficiency and reliability compared to existing power transmission systems. Despite the high cost of superconductors the low losses in the transmission makes the system cost effective for long run. As advancements in superconductor materials continue,

Table 4.1: Projects of DC power transmission through superconductors [5].

Year	Current (A)/ Voltage (kV)	HTS Material	Location	Ref
2017	20000 / 1	REBCO	Germany	[128]
2006	2200 / 20	BSCCO	Japan	[129]
2015	3250 / 80	REBCO	Korea	[130]
2012	10000 / 1.3	BSCCO	China	[131]
2014	20000 / -	MgB2	Switzerland	[132]
2018	2500 / 20	BSCCO	Russia	[133]

low voltage and high current systems are emerging. The Electric Power Research Institute (EPRI) has set a target for future superconducting power transmission systems to achieve 100 kA, with an operating voltage of around 250 V or $\pm 125 V$.

4.4 Superconducting busbar for electric aircraft

The DC distribution system is highly favoured in all-electric aircraft primarily due to the advanced technical maturity of power converters, which effectively manage power flow. NASA proposed an electric distributed propulsion system [123], power is distributed to each propulsion unit via individual converter, highlighting the critical need for a robust and efficient power management system. Also in terms of power generation CHEETA project shows that there may be multiple sources or locations of the fuel situated on board [124]. A similar kind of power distribution system is illustrated in figure 4.3.

A superconducting busbar is essential to integrate and manage multiple power sources and propulsion units within the aircraft's power distribution system. A superconducting busbar will transfer high power efficiently from power on-board sources to the loads/ propulsion units. A superconducting busbar will carry the high current and distribute among the loads based on the requirement, an illustration of a superconducting busbar is shown in figure 4.4. A conventional busbar used in a power distribution system is typically made from copper or
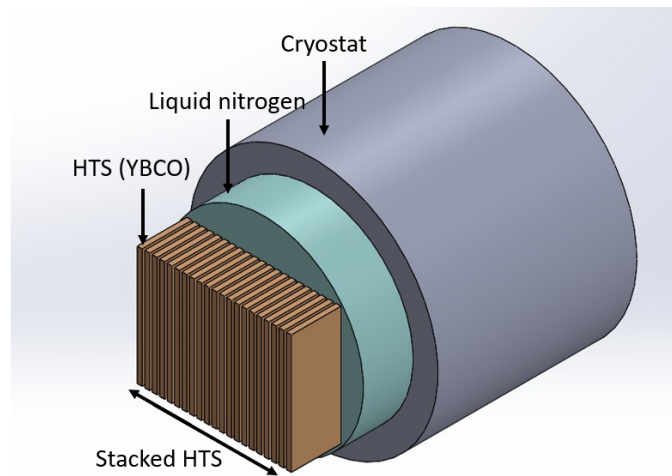
Figure 4.4: Illustration of superconducting busbar with multiple HTS tapes stacked together submerged in liquid nitrogen, and assembly enclosed in a cryostat [5].

aluminium. A busbar in a power distribution system carries current from the entire system and distributes it to different loads. However, conventional busbars are not suitable for all-electric aircraft applications due to their high weight, large size, and high losses. Therefore, a superconducting busbar is required for this distribution system to carry and distribute the current to the required loads efficiently.

4.4.1 Busbar solution comparison

In power distribution systems, a busbar is a critical component used to distribute current efficiently to various loads. It is designed to handle high currents and can easily isolate loads be using circuit breaker devices. A busbar acts as a point of intersection between source and load and helps save the loads during fault conditions. A superconducting busbar is expected to perform similar functions with enhanced efficiency and performance. Traditional busbars are made from copper or aluminium, typically in the form of thick bars and current carrying capacity depends upon the thickness of the bar. Copper and aluminium busbars are not suitable for all-electric aircraft due to their high weight and occupying more space, due to this there is a requirement to develop new technologies. Superconducting busbar is a potential solution for high-current applications, to understand why superconducting busbar a superior solution for

high current transmission is compared to copper and aluminium busbar a comparative study has been done.

A comprehensive comparative analysis between high-temperature superconducting (HTS) busbars and traditional copper and aluminium busbars is presented in table 4.2. This analysis aims to illustrate why superconducting busbars are an efficient and advantageous solution for all-electric aircraft propulsion systems. In this study, the author has used the highest current ratings of copper and aluminium busbars available as single units. The maximum current rating for a single copper busbar is 6.6 kA. ABB is a manufacturer of high-current copper busbars, the data used in this study, was used from the ABB website [134]. For aluminium busbars, the highest current capacity for a single unit is 2300 A. To make a fair comparison, three aluminium busbars are used to match the current capacity of the copper busbar for this study. For the superconducting busbar, 4 mm HTS tapes are used, each with a critical current of 180 A. In total, 36 HTS tapes are used, achieving a combined critical current of 6500 A. This setup allows for a direct comparison of the three busbar solutions—copper, aluminium, and HTS—each rated at approximately 6.5 kA. The comparison considers several key parameters, including current carrying capacity, weight, size, and efficiency. All busbars are evaluated at a temperature of 77K to ensure a consistent and fair basis for comparison. The resistance values for copper and aluminium at 77K are obtained from [135]. The resistance of the superconductor is calculated from the E-J power law.

The table not only highlights the superior current carrying capabilities of HTS busbars but also underscores their significant advantages in terms of weight and efficiency. Traditional copper and aluminium busbars are heavier and less efficient, which makes them not suitable for all-electric aircraft propulsion systems. The calculations provide a clear understanding of why superconducting busbars are more advantageous than traditional busbars. Table 4.2 shows that the joule heat loss in superconducting busbars is significantly lower compared to copper and aluminum busbars. Additionally, the weight and the area of superconducting busbars are also less, which is crucial for applications in all-electric aircraft where weight is a critical factor.

The design of a superconducting busbar incorporates copper tapes in between HTS tapes,

Table 4.2: Comparison of different busbar options.

Parameters at 77K	Copper busbar	Aluminium busbar (*3)	Busbar with HTS tapes (IC = 180A) (4mm) and Copper tapes (4mm) sandwiched between HTS tapes
Rated current (A)	6600	2300*3	6500
Total weight (Kg/m)	25	8.09	0.374
Cross section area (mm^2)	2760	3000	45
Resistivity (Ωm)	$2.03 * 10^{-9}$	$3.10 * 10^{-9}$	$8.04 * 10^{-20}$
Resistance (Ω)	$7.35 * 10^{-7}$	$1.034 * 10^{-6}$	$5.6 * 10^{-13}$
Heat Loss (W/m)	30 (hot)	8.3 (hot)	$2.405 * 10^{-5}$
Number of tapes	N/A	N/A	HTS = 36, CU = 35

which serve two essential purposes. Firstly, the tapes introduce a gap between HTS tapes, which helps to reduce the effect of self-field on critical current. This effect increases the efficiency of the superconducting busbar and reduces the cost. Secondly, it enhances the fault tolerance within the busbar design. Both these aspects are explored in further detail in this thesis. The superior performance of HTS busbars over traditional copper and aluminium busbars is evident from their reduced joule heat loss and lower weight. These attributes make HTS busbars a more viable option for an all-electric aircraft power distribution system.

4.5 Conclusion

This chapter has provided an extensive overview of the crucial role that superconductivity will play in the development of future electric aircraft. These next-generation aircraft's anticipated power requirements highlight the significant energy demands they will face as they transition to fully electric propulsion systems. The chapter outlines the challenges of meeting these

power requirements and the necessity for innovative solutions. The chapter contrasts the established voltage standards of conventional aircraft with the potential new standards that could be implemented for electric aircraft to ensure optimal performance and safety. At present voltage standards, designed for traditional aircraft systems, is not suffice for the higher power demands of electric aircraft. The discussion explores how new voltage standards could better accommodate the electrical needs of these advanced aircraft, thereby enhancing their efficiency and reliability.

Furthermore, this chapter provides a comparative analysis of copper, aluminium, and HTS busbar solutions and demonstrates that superconducting busbars offer a highly efficient, lightweight alternative to conventional busbars, making them an ideal choice for future all-electric aircraft. Superconducting busbars are essential for handling high power efficiently, with minimal energy loss and reduced weight compared to traditional busbars made from materials like copper or aluminium. By exploring the power distribution challenges and the potential of superconducting technology, this chapter lays the groundwork for understanding the benefits of superconducting busbars for all-electric aircraft. In next chapter a design of superconducting busbar is developed through modelling and experiments are conducted to verify modelling results.

5

Design assessment through modelling and experimental analysis

5.1 Introduction

For high-current applications, multiple HTS tapes need to be grouped or stacked together in parallel, as the critical current (IC) of a single HTS tape is limited to a few hundred amps. A careful design is required for efficient operation, as the critical current of the HTS tapes is affected by its magnetic self-field [136, 137, 138]. When multiple tapes are connected in parallel, the stack's IC equals the sum of each individual tape's IC. However, the self-field produced by the current flowing through these multiple HTS tapes cannot be ignored, and this results in a decrease in overall critical current. Calculating the total critical currents of the tape under specific operating conditions without considering the self-field effect leads to an overestimation of the tape's critical current performance. The influence of the magnetic self-field on the critical current depends on the number of HTS tapes connected in parallel and the distance between them. The TA-formulation is applied to investigate the optimal geometry and design for the superconducting busbar. This formulation is used to analyse the impact of the gap between HTS tapes on self-field-dependent critical current and how to reduce this self-field effect on critical current. The TA-formulation is also used to develop an

electromagnetic model of a superconducting busbar; with this model, a study is conducted to assess the design of the busbar. It is observed from the electromagnetic model that, in a multiple HTS tapes design, adding a gap between HTS tapes helps to reduce the effect of self-field on critical current. In this chapter, based on modelling results, the superconducting busbar prototype is developed and tested.

5.2   2-D simulation of superconducting busbar

5.2.1   TA-formulation

The electromagnetic behavior of the superconducting busbar is predicted using TA-formulation. This mathematical model employs Maxwell's equations to develop an electromagnetic model. This method was initially introduced by Zhang *et al* [139, 140]. T-A model primarily relies on the thin strip approximation and involves solving two state variables: calculating the current vector potential (T) within the superconducting layer and determining the magnetic vector potential (A) throughout the entire space. The two state variables, T and A, are utilized to compute the current density (J) and the magnetic flux density (B) with the help of the following equations [9].

$$J = \nabla \times T \tag{5.1}$$

$$B = \nabla \times A \tag{5.2}$$

The E-J power law is applied to model the resistivity of HTS tapes by coupling the local electric field with local current density exclusively within the superconducting domain.

$$E = E_c \frac{J}{J_c(B)} \left(\frac{J}{J_c(B)} \right)^{n-1} \tag{5.3}$$

Here, E_c is electric field criteria $1 \mu V/cm$, J_c is field-dependent critical current density, and n is superconducting n-value which also depends upon the magnetic field.

In the HTS domain Maxwell-Faraday's law is implemented with the following equation.

$$\nabla \times E = -\frac{\partial B}{\partial t} \tag{5.4}$$

Maxwell-Ampere's law is implemented in the whole domain and solved with:

$$\nabla \times \nabla \times A = \mu_0 \mu_r J \tag{5.5}$$

Where μ_0 represents the magnetic permeability of free space, and μ_r denotes the relative permeability, respectively.

The current density is linked to the A formulation through the application of an external surface current density, J_e.

$$J_e = J.d \tag{5.6}$$

where d represents the thickness of the HTS tape. J_e is applied to the tape in units of Am^{-1} to account for the thin strip approximation, effectively disregarding the thickness of the HTS layer.

The transport current that flows through the superconductor is introduced at the terminals of the tape. This can be depicted as the integral of the current density across the conductor's cross-section.

$$I = \iint_S J\, dS = \iint_S \nabla \times T\, ds = \oint_{\partial S} T\, ds. \tag{5.7}$$

Here, S denotes the cross-sectional area of the conductor, while ∂S indicates the boundary edges of that cross section.

5.2.2 2D TA-Formulation

The high aspect ratio of 2G HTS tapes, simulating the entire surface demands extensive computation time. The T-A formulation addresses this challenge by implementing the thin strip approximation for the tape. This method of simplification effectively reduces the HTS
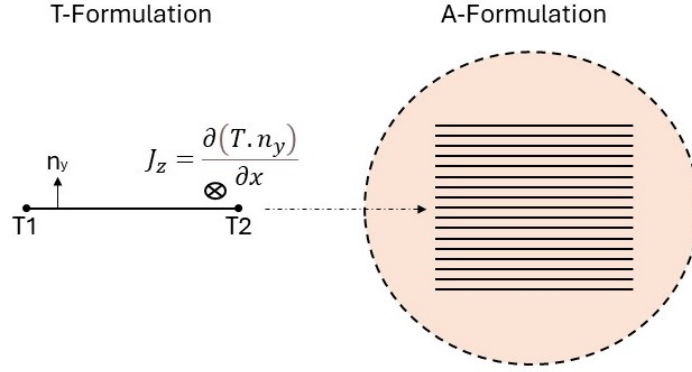
Figure 5.1: T is calculated solely within the superconducting domain (indicated by black lines), whereas A is determined throughout the entire area. The HTS tape's thickness is simplified into a superconducting layer, depicted as a 1D line element. The current is applied through boundary conditions at the tape's edges, T1 and T2 [9].

tape's surface area to a thin sheet, making the simulation process more efficient, as illustrated in figure 5.1.

Consequently, the current flows solely within the superconducting sheet, with T being constrained to the component that is perpendicular to the tape. The current vector potential is thus expressed as $T{\cdot}n$, where n is the normal vector perpendicular to the tape's wide face, represented in both Cartesian n = $[n_x n_y n_z]^T$ and cylindrical $n = [n_r n_\varphi n_z]^T$ coordinates. In a 2D perspective, the HTS tape's surface element is simplified to a 1D line element, allowing equation (5.1) to be reformulated as.

$$ J_z = \frac{\partial(T.n_y)}{\partial_x} - \frac{\partial(T.n_x)}{\partial_y} \tag{5.8} $$

in Cartesian coordinates, or for problems with axial symmetry, in cylindrical coordinates as

$$ J_\varphi = \frac{\partial(T.n_r)}{\partial_z} \tag{5.9} $$

Equation (5.9) describes a general case for a configured tape where the current flows in the φ direction, reducing the current vector potential to $T \cdot nr$. Moreover, when Faraday's law is applied, equation (5.4) can be streamlined to,

$$\begin{bmatrix} \dfrac{\partial E_Z}{\partial y} \\[2em] -\dfrac{\partial E_Z}{\partial x} \end{bmatrix} .n + \begin{bmatrix} \dfrac{\partial B_x}{\partial t} \\[2em] -\dfrac{\partial B_y}{\partial t} \end{bmatrix} .n = 0 \tag{5.10}$$

$$\left[-\dfrac{\partial E_\varphi}{\partial Z} \right] .n + \left[\dfrac{\partial B_r}{\partial t} \right] .n = 0 \tag{5.11}$$

A transport current, as specified in equation (5.7), can subsequently be introduced to the tape's edges using.

$$I = (T_1 - T_2)\delta \tag{5.12}$$

where T1 and T2 represent the current vector potentials at the respective edge points, and δ denotes the thickness of the superconducting tape.

5.2.3   FEA model of superconducting busbar

The superconducting busbar numerical model is developed with the help of Maxwell's equations using the TA-Formulation. COMSOL Multiphysics AC-DC module software is used to develop the model. This approach simplifies by only considering the superconducting layer, which is reasonable due to its significantly low resistivity compared to other layers of the coated conductor. This approach reduces calculation time while maintaining good accuracy when simulating the electromagnetic characteristics of 2G HTS stacks.

One significant limitation of the other formulations, such as the H formulation, is there computational efficiency, particularly when dealing with systems that incorporate a substantial number of superconducting tapes. This issue becomes particularly pronounced with HTS coated conductors, which are characterized by a large width-to-thickness ratio of the super-conducting layer. This specific attribute greatly increases the total number of degrees of

freedom (DOF) required to accurately model the system, making the computational process more demanding.

The T-A formulation has recently proven to be an effective alternative for modeling such complex systems [141]. The T-A approach simplifies the representation of HTS coated conductors by treating the superconducting layer as an infinitely thin sheet. This simplification allows for the assumption that changes in electromagnetic properties across the thickness of the superconducting layer can be largely disregarded, thereby reducing the computational load and enhancing the model's efficiency. This makes the T-A formulation particularly suitable for applications involving large arrays of HTS coated conductors, where traditional methods might struggle with scalability and speed.

Geometry description

A 2D model of a superconducting busbar is developed using the TA formulation, similar to the approach taken by Zhang et al. [139] as explained in the previous section. The model includes HTS tapes and is assumed to be infinitely long along the z-axis. This modelling approach is based on thin strip approximation. This model allows us to solve T (current vector potential) within the superconducting domain and A (magnetic vector potential) throughout the entire domain. Figure 5.2 shows the geometry implemented in COMSOL.

The thin strip approximation reduces the surface area of the HTS tape, this helps to solve the high aspect ratio problem. This helps to reduce the mesh size and speed up the computation process. The mesh structure is shown in figure 5.3.

5.2.4   2D FEA modelling analysis

The superconducting busbar model has been developed. The design focuses on reducing the effect of the self-field on critical current to enhance the efficiency of the superconducting busbar. The critical current of a superconductor depends on the self-field (s.f); as the applied current begins to flow through the superconductor, it generates a magnetic field. As the applied current increases, the field also increases correspondingly. As the self-field increases,
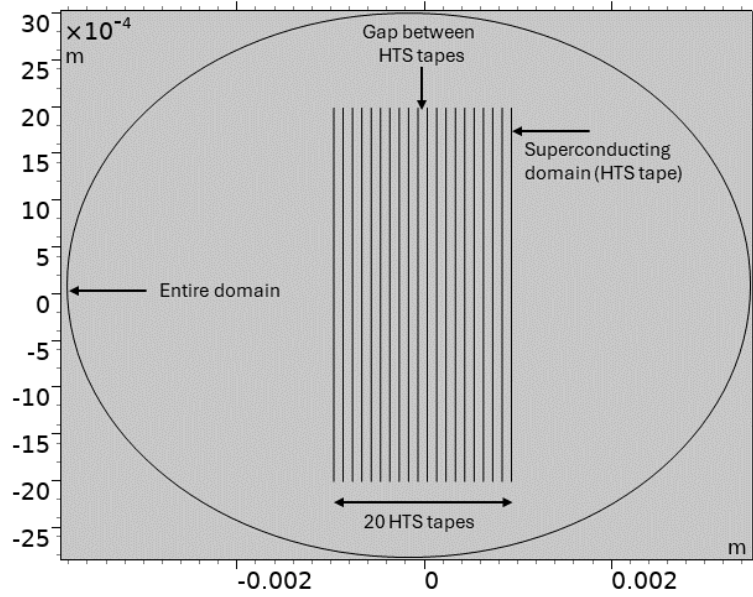
Figure 5.2: Schematic of HTS busbar model. This model considers HTS tape as an HTS layer, multiple such layers are modelled in parallel. The superconducting busbar contains 20 HTS tapes.
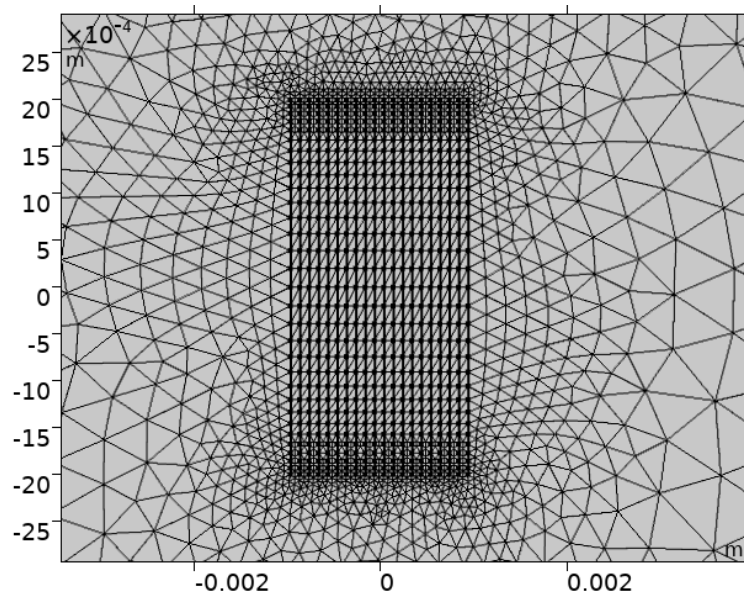
Figure 5.3: Schematic of HTS busbar model with mesh structure. Finalized geometry has 1 domain and 24 boundaries. The whole domain consists of 5126 domain elements.

the critical current begins to decrease. This effect becomes more pronounced in designs involving multiple tapes and high magnitude of the current. Introducing a gap between HTS

Table 5.1: Parameters used in modeling of HTS busbar.

Parameter	5 HTS tape	10 HTS tape	20 HTS tape
Critical current of each Tape	100	100	100
Applied current	0.5 kA	1 kA	2 kA
Operating temperature	77K	77K	77K
Thickness of HTS tape	1 μm	1 μm	1 μm
Gap between HTS tapes	1 μm, 100 μm, 1 mm	1 μm, 100 μm, 1 mm	1 μm, 100 μm, 1 mm
Critical current	465A, 471A, 490A	838A, 878A, 969A	1396A, 1575A, 1920A

tapes reduces the effect of the self-field on the critical current in multiple tape designs. A comparison is made by varying the gap between HTS tapes and the number of HTS tapes in the design to understand the effect on critical current. Three designs, each with 20, 10, and 5 HTS tapes and gaps of 1 μm, 100 μm, and 1 mm between the tapes, are compared.

Effect of gap between HTS tapes on self-field

Nine electromagnetic model results are compared to observe the effect of the gap on the self-field. As critical current depends on the self-field, this analysis demonstrates how a design using multiple HTS tapes can be used for high-current transmission applications. The parameters used in the modelling is shown in table 5.1.

In the first design gap between HTS tapes is 1μm, with 1μm gap three models run with 5, 10, and 20 HTS tapes, as shown in figure 5.4. The second design also has the same number of HTS tapes but with a 100μm gap between them, and the effect on the field due to this gap is shown in figure 5.5. The third design maintains the same number of HTS tapes, but the gap between them is increased to 1 mm. The results clearly show that in a multiple-tape busbar design, the magnitude of the field generated depends on the gap between the HTS

tapes. As figures 5.4, 5.5, and 5.6 demonstrate, increasing the gap between the HTS tapes decreases the magnitude of the self-field generated by the busbar. The effect of the self-field also depends upon the number of HTS tapes in the superconducting busbar, as the number of HTS tapes increases in the busbar the self-field also increases. The critical current of the superconducting busbar depends on the self-field. Simulation analysis shows, that an increase in the gap between HTS tapes reduces the magnitude of self-field. Adding a gap between HTS tapes in multiple tape busbar design can enhance the efficiency of the superconducting busbar design.
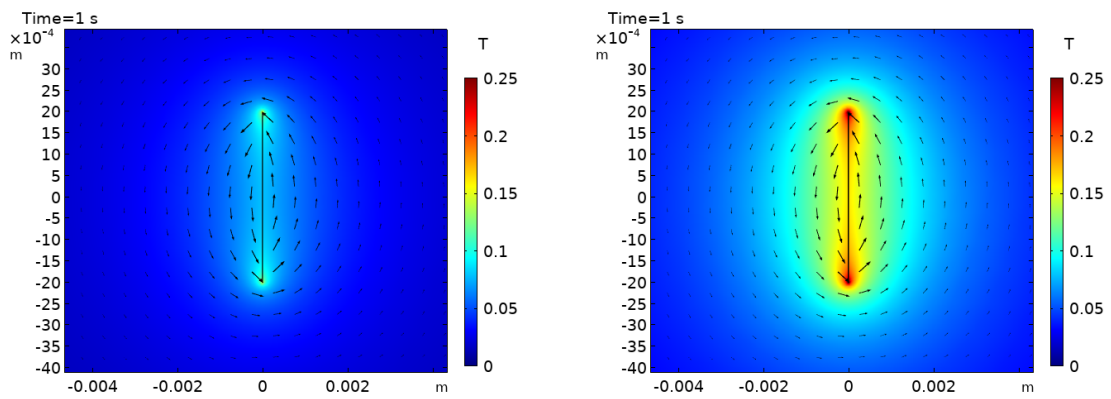
(a) 5 HTS tapes, with 1 μm gap between HTS tapes.

(b) 10 HTS tapes, with 1 μm gap between HTS tapes.
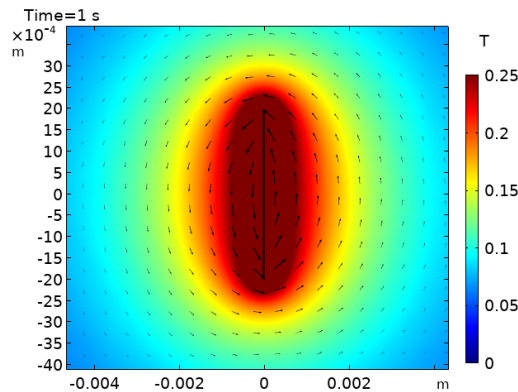
(c) 20 HTS tapes, with 1 μm gap between HTS tapes.

Figure 5.4: Field distribution generated by HTS busbar with 5, 10, and 20 HTS tapes with a gap of 1μm.
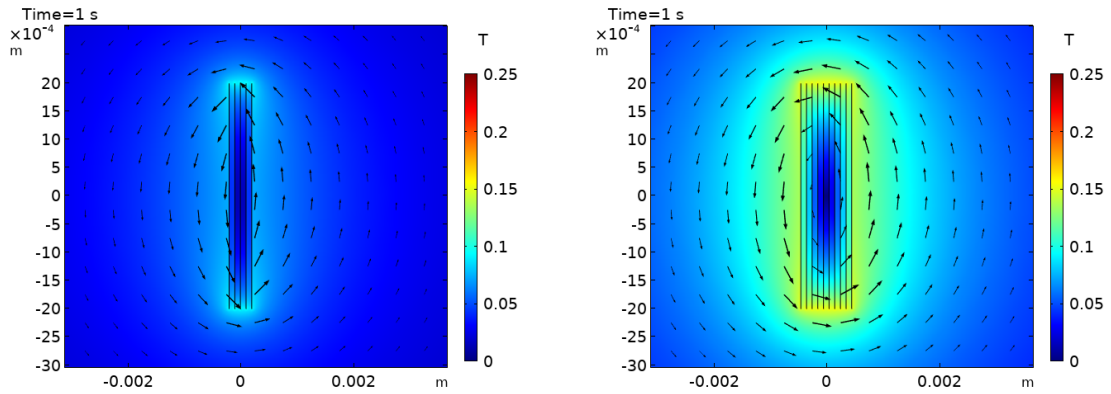
(a) 5 HTS tapes, with 100 μm gap between HTS tapes.

(b) 10 HTS tapes, with 100 μm gap between HTS tapes.
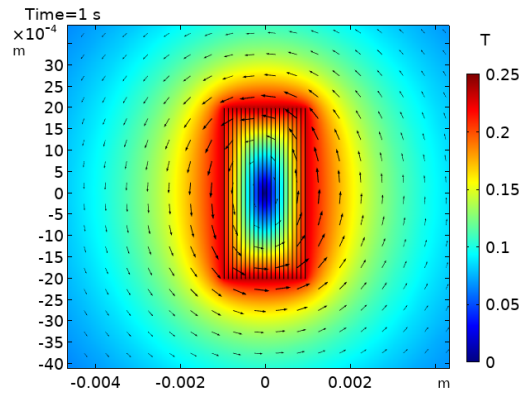
(c) 20 HTS tapes, with 100 μm gap between HTS tapes.

Figure 5.5: Field distribution generated by HTS busbar with 5, 10, and 20 HTS tapes with a gap of 100μm.

Effect of the gap between HTS tapes on critical current

The critical current of the superconducting busbar depends upon the self-field, it is explained in the previous section how the field generated due to the current through the HTS tapes can be reduced. Current distribution is calculated with the equation (5.1), and magnetic field distribution can be calculated through equation (5.2). Critical current is calculated through equation (5.13), delta is $1\mu m$, thickness of the HTS tape and J_c is the field-dependent critical current density and IC is critical current of HTS tape.

(a) 5 HTS tapes, with 1 mm gap between HTS tapes.

(b) 10 HTS tapes, with 1 mm gap between HTS tapes.

(c) 20 HTS tapes, with 1 mm gap between HTS tapes.
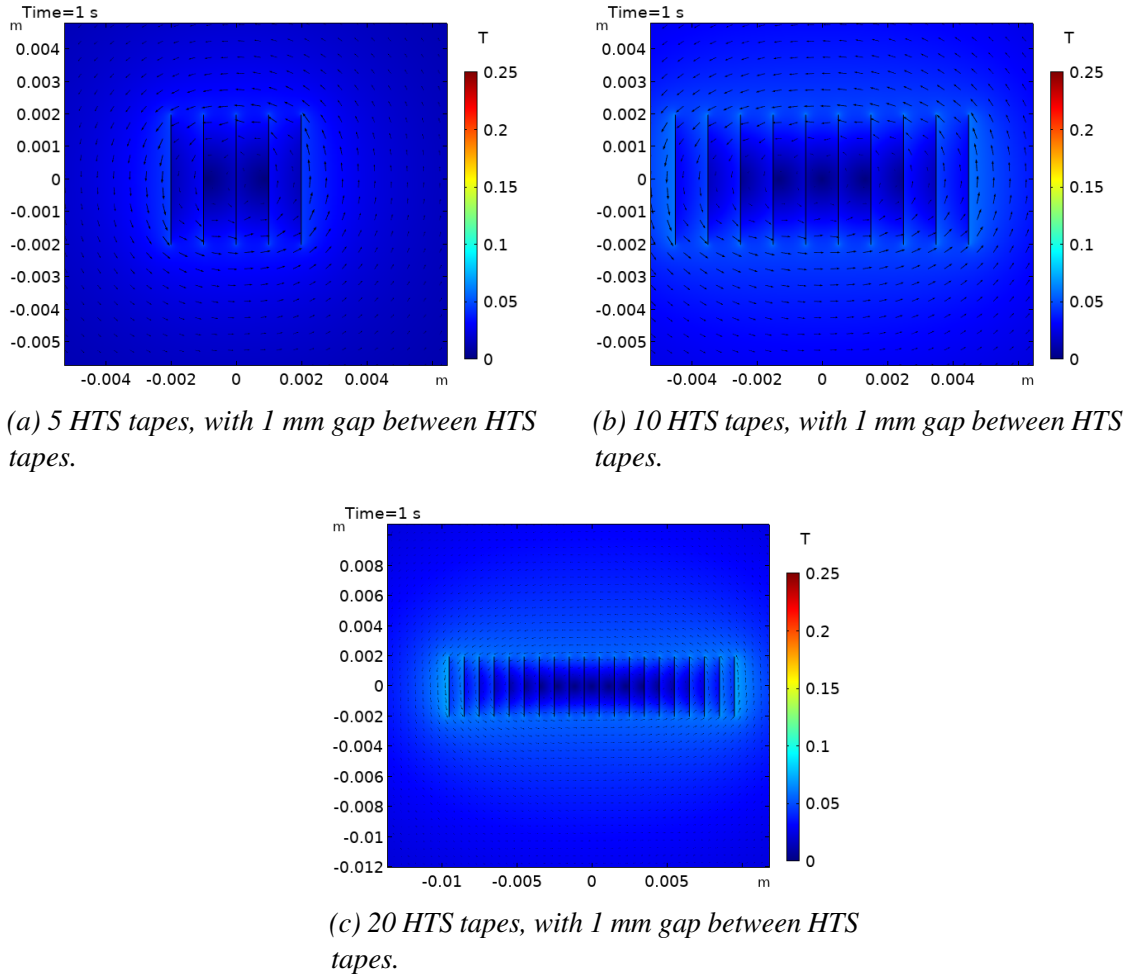
Figure 5.6: Field distribution generated by HTS busbar with 5, 10, and 20 HTS tapes with a gap of 1 mm.

$$\int J_c * delta = IC \tag{5.13}$$

The same models discussed in the above section are used to assess the impact of the gap between HTS tapes on field-dependent critical current. The first design features a $1\mu m$ gap between HTS tapes. With this gap, three models are run with 5, 10, and 20 HTS tapes, as illustrated in figure 5.7. This figure depicts the relationship between the applied current and the field-dependent critical current. As the applied current increases, the self-field, which is a function of the applied current, also increases. Consequently, the field-dependent critical
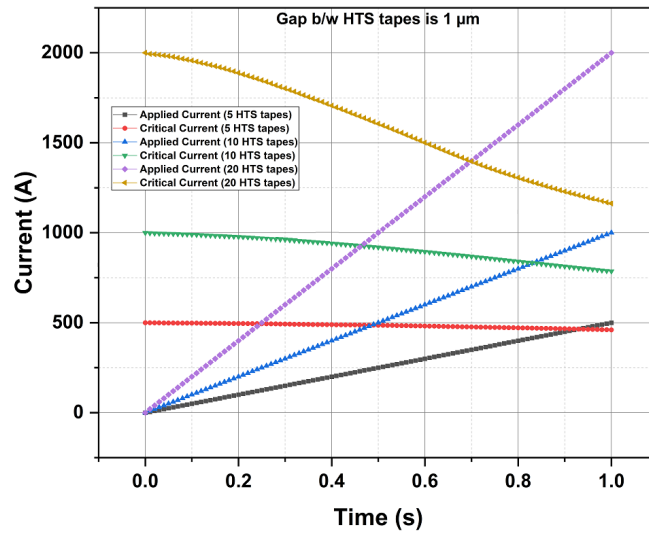
Figure 5.7: Field dependent critical current w.r.t applied current with 1 μm gap between HTS tapes

current begins to decrease as the applied current rises. The critical current depends on the number of HTS tapes and the magnitude of the current. It is evident from figure 5.7 that with a lower magnitude of current and fewer tapes, the effect of the self-field on the critical current is less pronounced. However, in designs using high current and multiple tapes, the impact on the field-dependent critical current is high.

Figure 5.8 shows the relationship between the field-dependent critical current and the applied current when the gap between HTS tapes is 100 μm. The results in figure 5.8 indicate that the field-dependent critical current is higher compared to that in figure 5.7. This increase is due to the larger gap between the HTS tapes, which reduces the magnitude of the field, as shown in figure 5.5.

In figure 5.9, the results for a superconducting busbar with 5, 10, and 20 HTS tapes with a 1 mm gap between the tapes are shown. Compared to figures 5.7 and 5.8, the field-dependent critical current is higher, due to the further increased gap. Table 5.1 compares the field-dependent critical current resulting from different gaps between HTS tapes. The results indicate that for high-current transmission applications where multiple HTS tapes require, increasing the gap between the tapes enhances the efficiency of the design. This also makes the design more cost-friendly due to the high cost of HTS tapes.
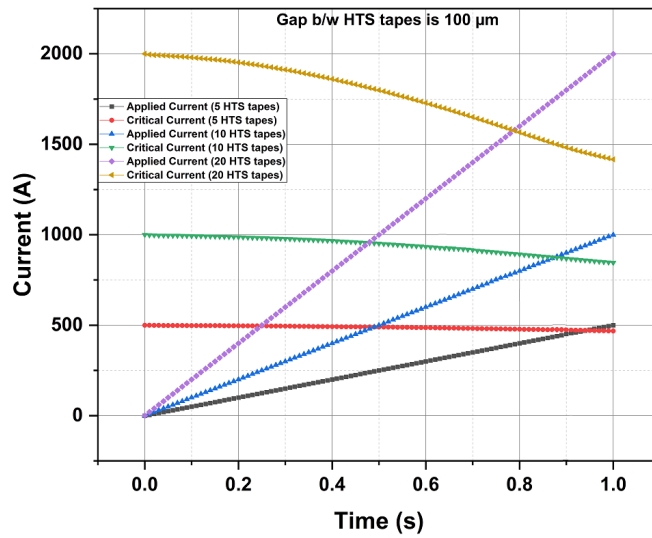
Figure 5.8: Field dependent critical current w.r.t applied current with 100 μm gap between HTS tapes
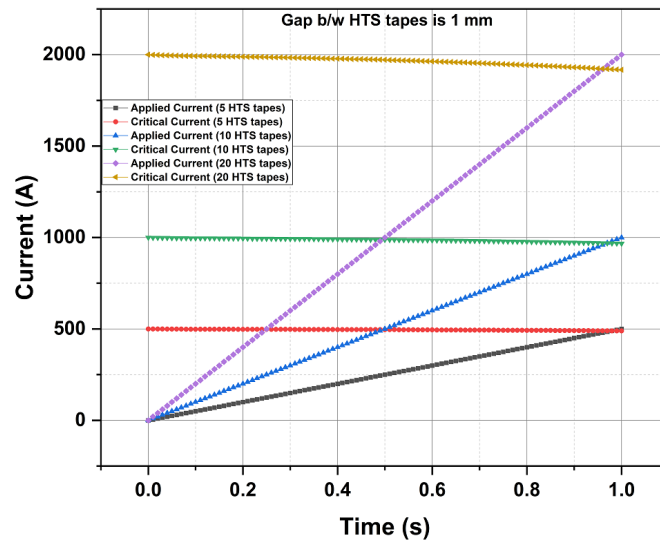
Figure 5.9: Field dependent critical current w.r.t applied current with 100 mm gap between HTS tapes

5.3 Experimental validation and analysis

To verify the observations from the modelling, a prototype has been developed and tested in a laboratory. Details of the superconducting busbar mechanical design, process of prototyping, and experimental results are discussed in this section.

5.3.1 Geometric description and prototyping process of the superconducting busbar

In this study, a design of a superconducting busbar prototype has been developed and tested. The tests confirm that the design effectively reduces the effect of self-field on critical current. Shanghai second-generation YBCO HTS tape with a critical current of 100 A and a thickness of 53 μm is used for the prototyping. The stack technique is employed in the development of the prototypes. The importance of adding a gap between HTS tapes, which was observed from the modelling, is implemented by adding a copper thickness of 100 μm between the HTS tapes. Figure 5.10 shows the schematic of the superconducting busbar. The prototype uses 10 HTS tapes with 9 copper tapes, copper tapes are inserted in between HTS tapes to create a gap between the HTS tapes, as illustrated in figure 5.10. The parameters used to design the HTS busbar are listed in table 5.2.

In this thesis, a copper tape with a thickness of 100 μm was used. This specific thickness was selected to validate that introducing a gap between HTS tapes can lead to an increase in the critical current. Additionally, the use of copper in the design plays a significant role in enhancing the fault tolerance of the system. By incorporating copper, the system becomes more robust, providing additional safety and resilience under fault current conditions, which would not be the case if other material were used, such as aluminum. Also, copper is easy to solder compared to other metals like aluminum. The choice of 100 μm thickness is used for proving the concept. The copper thickness can be adjusted to suit different fault current levels depending on the requirements of the system. This flexibility is crucial for adapting the design to various operational conditions, particularly as there are no established standards for current and voltage levels in all-electric aircraft systems. Given the experimental nature of this work, 100 μm thick copper was deemed an appropriate starting point for the busbar prototypes. It provides a balance between feasibility and functionality, enabling a clear demonstration of the benefits of introducing a gap between HTS tapes and utilizing copper to improve system reliability. Future work can explore varying copper thicknesses to optimize performance for specific applications and fault current scenarios.

Table 5.2: Parameters used in HTS Busbar Prototyping.

Parameter	HTS busbar
Number of HTS tapes	10
Width of HTS tape	4 mm
Critical current of HTS tape	100 A
Thickness of HTS tape	53 μm
Number of copper tapes	9
Width of copper tape	4 mm
Thickness of copper tape	100 μm

(a) Schematic of busbar design   (b) Prototype of superconducting busbar
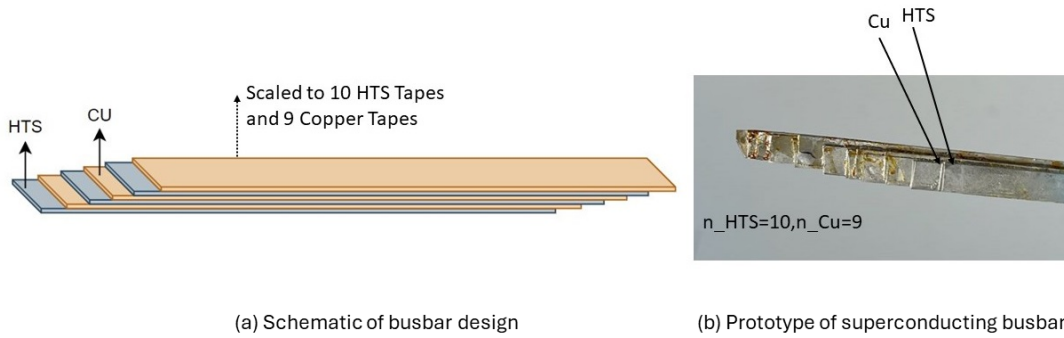
Figure 5.10: (a) Schematic design of superconducting busbar. (b) Prototype of superconducting busbar with 10 HTS tapes and 9 copper tapes sandwiched between HTS tapes.

Prototyping process for superconducting busbar

The HTS busbar prototyping process involves multiple steps. After multiple trials, the author of this thesis concluded that the best way to implement this process is explained here:

Step 1: Select the HTS tape based on your application requirements. Ensure that when selecting an HTS tape, the outer layer is made of a material that can easily be soldered with other tapes. In this work, the author has used HTS tape with an outer layer of copper.

Step 2: Treat the HTS and copper tape surfaces with flux to remove oxidants from the surface and to help spread the solder evenly across the surface of both the HTS and copper tapes.
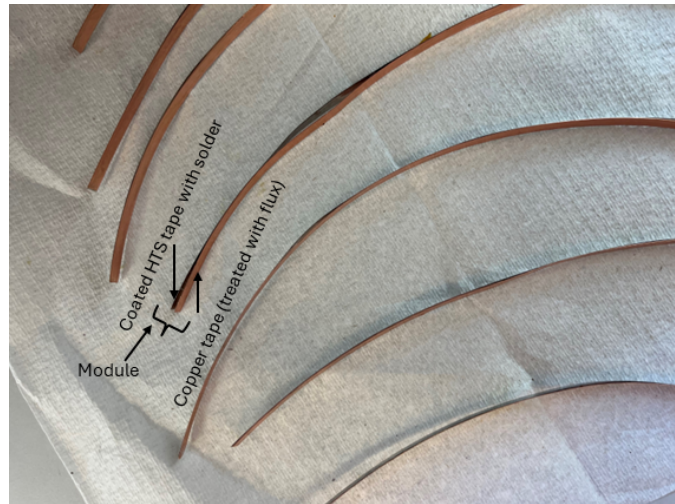
Figure 5.11: Unit Module of the HTS Busbar: Multiple modules are stacked and soldered together to assemble the complete busbar.

Figure 5.12: All modules hold together with Kapton tape before soldering together.

Step 3: Coat the entire surface of HTS tape with Pbsn solder and then treat again with flux.

Step 4: After coating HTS with a soldering layer make modules, each module contains one HTS tape and one copper tape as shown in figure 5.11.

Step 5: Stack all the unit modules and tie them tightly together with Kapton tape, as shown in figure 5.12.

Step 6: Place the assembly in the former; in this case, a copper former is used. Ensure that mechanical pressure is exerted on the assembly through the former.

Step 7: Place the former in a preheated oven at 210°C and let the assembly bake for 20
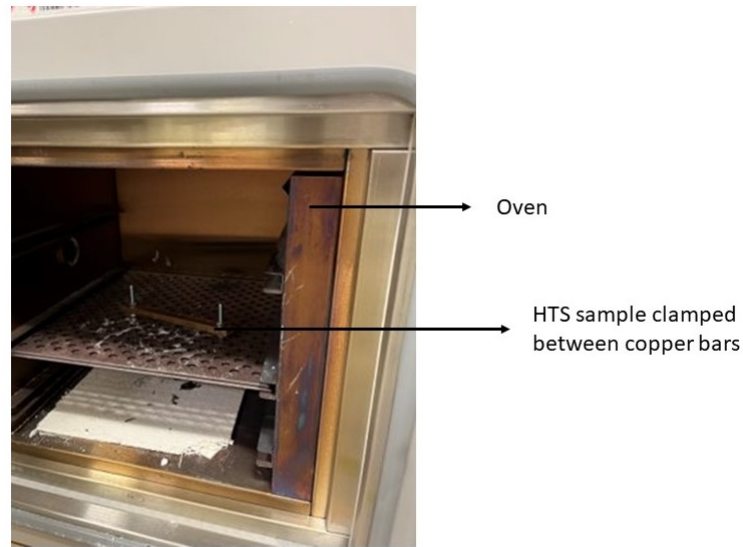
Figure 5.13: Oven used to melt the solder.

minutes. The oven used to bake the samples to melt the solder is shown in figure 5.13.

Step 8: Remove the sample from the oven and let it cool to room temperature before removing the assembly from the former.

Step 9: Once the sample cooled to room temperature and separated from the copper former, remove the Kapton tape from the busbar.

5.3.2   Experimental setup and results

Experimental setup

The schematic of the setup used to conduct experiments is shown in figure 5.14, and the photograph of the laboratory equipment is shown in figure 5.15. Experiments are conducted in a liquid nitrogen (LN2) environment with an open bath cryostat. A DC power supply drives current through the prototype, the current is measured through a shunt, and voltage is measured through voltage taps. An NI (National Instruments) LabVIEW interface is used for real-time data acquisition. A brief explanation of the equipment used in the experiments is provided here in this section.
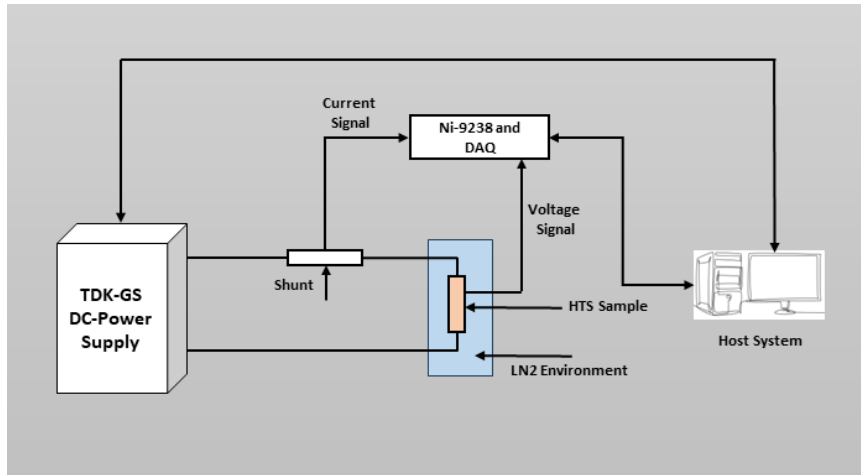
Figure 5.14: Schematic of experimental setup.
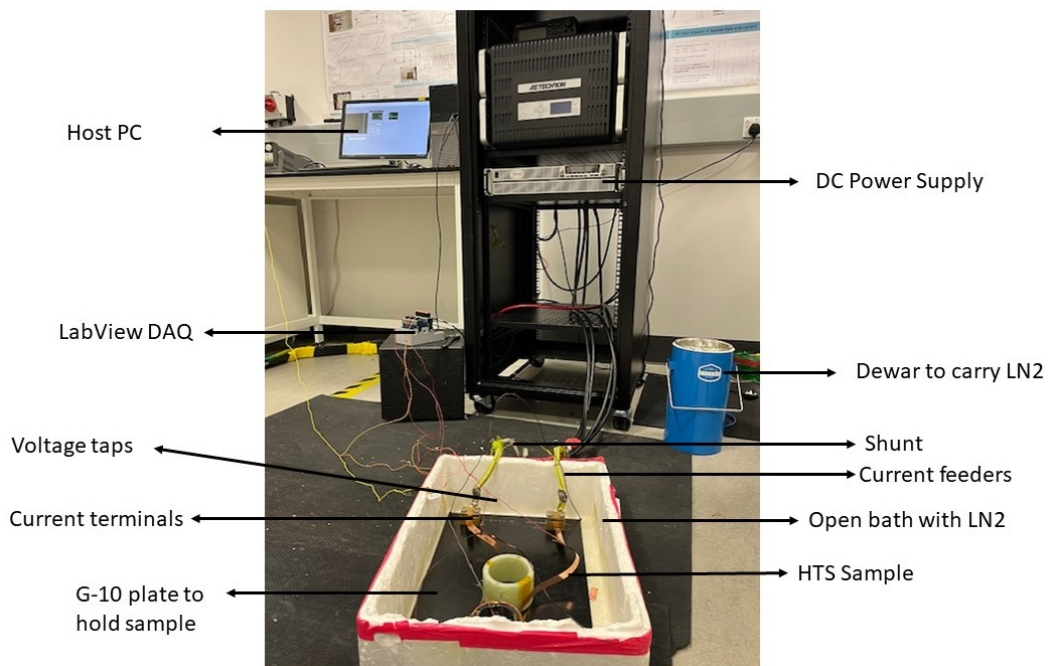
Figure 5.15: Experimental setup used for the experiments.

Power supply

The TDK-Lambda Genesys+ GSP10 DC power supply is used for the experiments. The DC power supply is a programmable switching power supply, with a low-voltage and high-current output which is desirable for superconducting applications. This power supply operates

with a 3-phase input and accommodates an AC input voltage range from 342 to 460 Vac, making it adaptable to various power networks. It also supports an input frequency range from 47 to 63 Hz. The power supply offers a rated output voltage of 10 Vdc and allows adjustments from 0 to 10 Vdc, with a maximum rated output current of 1000 A. The power supply provides an output power of 10 kW and maintains high efficiency at 89.5%. It ensures minimal disturbance in sensitive environments with a voltage ripple noise of 0.008 Vrms and a current ripple noise of 1.2 Arms, both measured from 5 Hz to 1 MHz. The power supply is controlled via its communication channel through a host system. The host system uses LABVIEW software to control and monitor the power supply operation.

Data acquisition system

For data acquisition National Instruments (NI) cDAQ-9174 chassis and NI-9238 module is used. The cDAQ-9174 chassis supports a range of functionalities determined by the C Series I/O modules used. It boasts an analog input FIFO size of 127 samples per slot, with a maximum sample rate and number of channels supported depending on the specific C Series I/O modules. Its timing accuracy is 50 ppm of the sample rate, and it offers a timing resolution of 12.5 ns. For analog output, the chassis allows up to 16 channels with hardware-timed tasks and supports both non-periodic and periodic waveform regeneration modes from onboard memory or the host buffer. The output FIFO (first in first out) size for onboard regeneration is 8,191 samples shared among channels used, and for non-regeneration tasks, it is 127 samples per slot. Additionally, it can handle a maximum update rate of 1.6 MS/s (mega sample per second) for multi-channel aggregate in the regeneration mode.

On the other hand, the NI-9238 module; features four analog input channels with a delta-sigma ADC providing 24-bit resolution. The module supports simultaneous sampling with a data rate range from 1.613 kS/s to 50 kS/s using an internal master time base, and from 390.625 S/s to 51.36 kS/s with an external master time base. It also offers robust input voltage ranges and protections, ensuring reliability and durability across various operating conditions from -40 °C to 70 °C. This combination of detailed technical specifications and flexible operational parameters makes the Compact DAQ system highly suitable for data

acquisition and monitoring applications.

Voltage and current measurement

Voltage measurement For voltage measurement, a 26 AWG twisted wire is used. Crocodile clips attached to this wire make it easy to use. The wire is twisted to reduce electromagnetic noise and improve signal quality during voltage measurement. The crocodile clips provide better quality and more consistent readings compared to soldering the wire directly to the sample for voltage measurement. The crocodile clips are attached directly to the superconducting busbar. The combination of twisted wire and crocodile clips increases the reliability and accuracy of the voltage measurements.

Current measurement A shunt is used for current measurements, an electrical shunt is a device designed to allow current to either pass through or be diverted around a particular point in a circuit by creating a low-resistance path. Electrical shunts are commonly used to measure the flow of DC current.

Ohm's law is applied as follows:

$V = I \times R$

This formula calculates the voltage (V) across a resistance (R in ohms), generated by the current (I in amps) flowing through that resistance.

To measure the voltage drop across a shunt, incorporate a shunt into a circuit specifically set up for measuring current. By evaluating the resistance of the shunt, the current can be calculated based on Ohm's law. This principle is also useful in calibrating the resistance of the shunt to ensure accurate current measurements.

5.3.3   Experimental result

Experiments were conducted to observe the effect of the gap on the critical current of the superconducting busbar. Four prototypes were prepared for testing and comparison. Out of the four, two prototypes use only HTS tapes, with 10 and 5 HTS tapes comprising the busbar samples. In the other two prototypes, copper (Cu) tapes are inserted between the HTS tapes
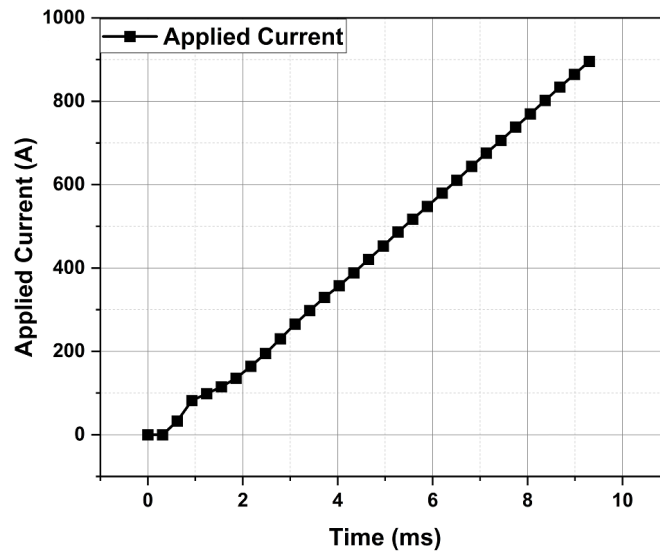
Figure 5.16: Applied current to the superconducting busbar.

to introduce a gap; these prototypes consist of 10 HTS tapes with 9 copper tapes and 5 HTS tapes with 4 Cu tapes, as shown in figure 5.12. The setup used to perform the critical current test is depicted in figure 5.14. A DC power supply pushes the current into the HTS busbar samples, through copper terminals. Copper terminals are used to connect the HTS busbar sample to the power supply. The copper terminals are also immersed in liquid nitrogen to reduce the heat leak between terminals and the superconducting busbar sample. The current generated through DC power supply, which is applied to the superconducting busbar sample, is depicted in figure 5.16.

The 1μV/cm criterion is used to measure the critical current, as shown in figure 5.17, and figure 5.18. The results show that the superconducting busbar design with only HTS tapes has a lower critical current compared to the busbar that includes both HTS and copper tapes. The V-I characteristics in figure 5.17, and figure 5.18 indicate that current flows only through the HTS tapes; no current flows through the copper tape. Given that the V-I characteristic of copper is linear in nature, it can be concluded that the current flows only through the superconductor during a steady state. Results show that adding a gap between HTS tapes helps to increase the field-dependent critical current and makes the design more efficient.

Figure 5.18 shows that, compared to figure 5.17, where both the HTS tapes and the applied

Table 5.3: Comparative analysis of parameters and experimental outcomes.

Parameter	10 HTS tapes	10 HTS and 9 Cu tapes
Number of HTS tapes	10	10
Width of HTS and CU tape	4 mm and NA	4mm and 4mm
Critical current of one HTS tape	100 A	100A
Number of copper tapes	NA	9
Thickness of copper tape	NA	100 μm
Critical current	720 A	840 A
Parameter	**5 HTS tapes**	**5 HTS and 4 Cu tapes**
Critical current	460 A	480 A
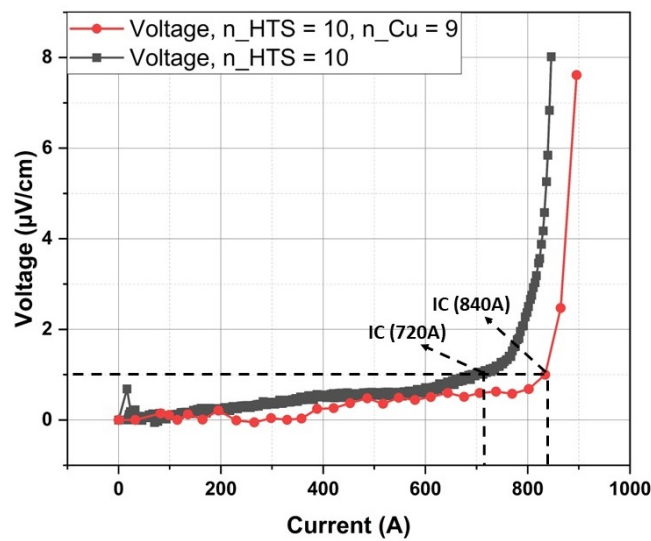
Figure 5.17: V-I Characteristics of HTS Busbar Samples: Comparison Between 10 HTS Tapes Alone and 10 HTS Tapes with 9 Copper Tapes [10].

current are doubled, the effect of self-field on critical current is less pronounced. It shows that the effect of self-field on critical current increases with the increase in current and the number of HTS tapes. For high-current applications where multiple HTS tapes are required, this effect cannot be neglected. Therefore, the approach of adding gaps is more suitable for high currents with multiple tape design, as shown in table 5.3.

Table 5.4: Comparative analysis of simulations and experiments.

Busbar design	Critical current (A) (Simulated)	Critical current (A) (Experimental)
HTS tapes (5) without gap	465	460
HTS tapes (5) with gap in between	471	480
HTS tapes (10) without gap	838	720
HTS tapes (10) with gap in between	878	840

The experimental results align closely with the simulation results, as shown in table 5.4. However, the observed differences in the critical current values, are due to several factors that I have not included in the modelling. The simulation provides an approximation of the critical current and helps to understand the electromagnetic behavior of the superconducting tape. The simulation model does not have the metallic layers in the HTS tape. These metallic layers, often included for mechanical support or stabilization, introduce additional complexities that impact the critical current in experimental conditions. Another significant factor contributing to the discrepancies is terminal resistance. In the experimental setup, terminal resistance generates additional losses when current flows from copper terminals to the superconducting busbar. These losses are not modeled in the simulation, leading to a slight overestimation of the critical current in the simulated results. Additionally, the soldering layers, which are essential for connecting the HTS tapes, also produce losses that are not considered in the modelling. These layers, though seemingly minor, can have a cumulative effect on the overall performance of the system. Thus, while the modelling provides a valuable approximation and predictive tool for analyzing the critical current, the absence of these factors in the simulation introduces a gap between the theoretical and experimental outcomes.
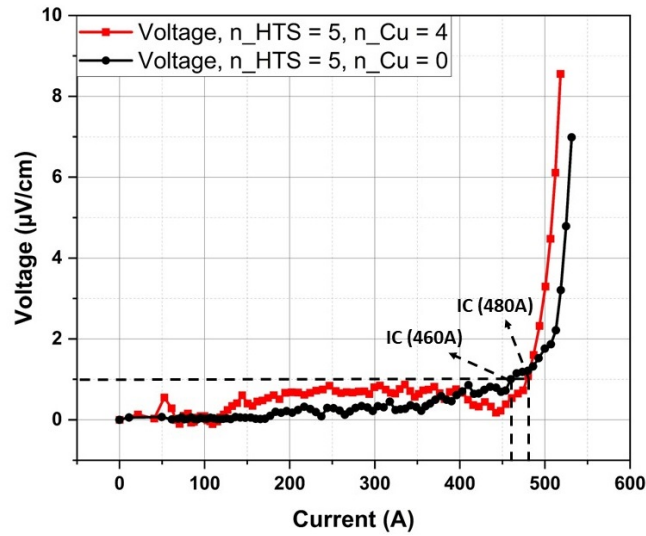
Figure 5.18: V-I Characteristics of HTS Busbar Samples: Comparison Between 5 HTS Tapes Alone and 5 HTS Tapes with 4 Copper Tapes [10].

5.4   Conclusion

This section explores an superconducting busbar design for high-current transmission applications. The critical current of a single HTS tape is limited to a few hundred amps; for high-current transmission, multiple HTS tapes need to be connected in parallel. The electromagnetic model of the superconducting busbar has shown that in the designs where multiple HTS tapes carry high currents, there is a decrease in critical current due to the self-field. This effect intensifies as the number of HTS tapes and the current passing through them increases. This effect not only reduces the efficiency of the busbar but also increases costs since more HTS tapes are needed to enhance the busbar's capacity. An effective method has been implemented to mitigate the effect of the self-field on critical current by introducing gaps between the HTS tapes. This gap is added between the HTS tapes in the busbar assembly is through the copper tapes. The results demonstrate that adding a gap with copper between the HTS tapes can decrease the effect of self-field on critical current. The results show that the current flows only through the superconducting tapes during a steady state, with no current flowing through the copper tape. This design enhances the efficiency of the superconducting

busbar. The design configuration is also modular and can be adapted based on application requirements.

6

Validation of fault-tolerant busbar design through modelling and testing

6.1 Introduction

High-temperature superconductors (HTS) are renowned for their high current-carrying capacity and almost negligible losses while carrying DC current. These advantageous properties make them suitable for high-current applications such as busbars [142, 143, 144, 145]. Superconductivity in superconductors is maintained if they are operated within certain temperature, field, and current density limits; exceeding any of these parameters causes the superconductor to lose its superconducting state. The E-J power law describes how the resistivity of the superconductor sharply increases if the applied current exceeds the critical current. This increase in resistivity leads to heat loss, which can damage the superconductor. For reliable and safe operation, busbar design should incorporate fault tolerance capabilities.

This chapter proposes a fault-tolerant superconducting busbar design that can ride through the fault or transient event. Commonly, copper is used as a stabilizer to carry the excess current during such events. As discussed in the previous chapter, the author has used copper tapes to introduce a gap between HTS tapes, enhancing fault tolerance in the superconducting busbar design. This chapter explores the working mechanism and the results of testing the

superconducting busbar against fault currents.

6.2 Fault-tolerance mechanism

When the applied current in an HTS tape exceeds the critical current, an exponential change in resistance can be observed. This change occurs because the current starts diverting from the superconducting layers to associated layers. Superconductor tapes consist of 5-6 different layers, as shown in section 3.2. During the superconducting state, current flows through the superconducting layer. However, as the current through superconducting layer exceeds the critical current, there is an exponential increase in resistance within the superconducting layer, and the current begins to divert to other layers of the HTS tape, whose resistance is lower at that time compared to the superconducting layer. As the current diverts from one layer to another, a voltage also begins to appear, which is required to push the current through the HTS tapes due to the increased resistance. This resistive behavior of the superconductor can be predicted using the E-J power law, as expressed in equation 6.1.

$$\rho_{sc} = \frac{E_0}{J_c} \left(\frac{J}{J_c} \right)^{(n-1)} \tag{6.1}$$

Here J is the current density and J_c is field dependent current density, E_0 is electric field criterion $(1 \mu V / cm)$.

Fault mitigation

For regular cables, the common fault scenario involves a short circuit, and design guidelines for this are outlined in the IEC 60364-5-54 standard. As far as the authors are aware, there are currently no published guidelines for fault scenarios specifically tailored to superconducting cables. However, it's worth noting that an IEC standard for testing AC superconducting power cables is currently in the drafting phase.

ReBCO tapes have high intrinsic electrical resistivity during the normal conducting state. ReBCO offers high electrical resistance during fault events, leading to high joule heating

during such events, which can potentially damage the cables. A parallel low-resistance stabilizer can be used to control the heat influx and divert the extra current during the fault event into the stabilizer. For this, joule heat can be calculated through:

$$Q_{joule} = R(T) * I^2_{fault} \tag{6.2}$$

R(T), is the temperature-dependent resistance of the stabilizer.

Temperature rise during fault event due to high current in stabilizer can be predicted through adiabatic energy balance

$$A.L \int_{T_{end}}^{T_{start}} c(T) \, dT = \int_{t_{fault}}^{0} \frac{\rho_{el}(T).L}{A} . I^2_{fault} dt \tag{6.3}$$

Here, A is the cross-section area of the stabilizer, with length L, specific resistivity of the stabilizer is $\rho_{el}(T)$, heat capacity of stabilizer is c(T), and maximum temperature is T_{end}.

A ReBCO cable was tested against a fault current of 31500 A for 2 s (as referenced in [146]). During the fault test, the majority of the current flows through the stabilizer. The cross-sectional area of the used stabilizer is 600 mm^2, and the temperature starts at 77.3 K and ends at 80 K.

Working of fault tolerance mechanism

As the current diverts from one layer to another, a parallel path helps carry the extra current and prevents permanent damage to the HTS. The workings of the fault tolerance mechanism are illustrated in figure 6.1. During a steady state, current flows only through the superconducting layer, where the resistance is lowest, allowing the current to follow the path of least resistance. Figures 5.17 and 5.18 show the V-I curve of a superconducting busbar during steady state, with a linear V-I curve for copper, indicating that during steady state, current flows only through the superconducting tape. When the applied current (I) is less than the critical current (IC), the current flows solely through the HTS tape (I_{HTS}). If I exceeds IC, the resistivity of the HTS tape increases compared to that of the copper tape, and current begins to flow through the copper stabilizer tape, as shown in figure 6.1. This configuration where copper is
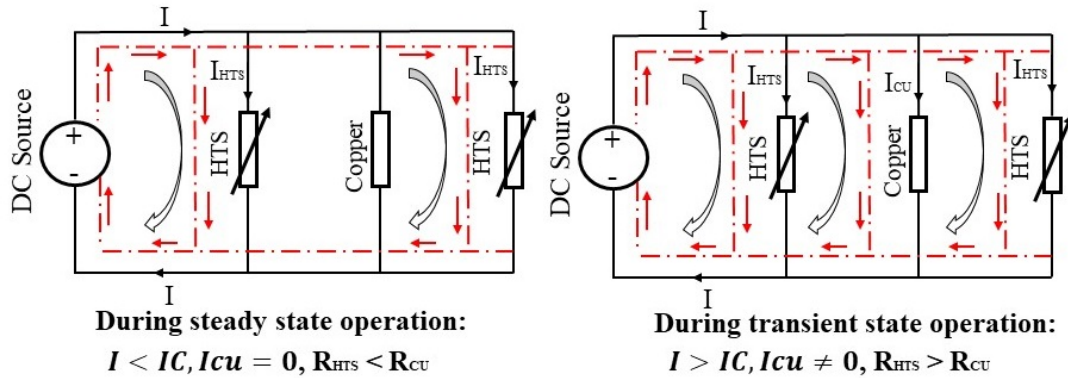
Figure 6.1: Working mechanism of busbar during steady state and fault state[10].

added between HTSt tapes, helps the superconducting busbar ride through the fault events and protects the HTS from burning. The copper tapes in between HTS tapes also increase the surface area of the superconducting busbar, which helps to remove heat during fault events more efficiently.

6.3   Modeling analysis of fault ride-through capability

6.3.1   2D H-formulation

To understand the current sharing among different tapes of superconducting busbar, during both fault (or transient) states as well as steady state, an electromagnetic model was developed using the H-formulation. COMSOL Multiphysics software with AC-DC module was used to develop the model, which is based on the solutions to Maxwell's equations [147, 148, 149, 150, 151, 152]. The electromagnetic model is divided into two domains: the superconducting domain and the air domain. In the H-formulation, other metal layers apart from the superconducting layer are also defined. A set of differential equations defined for each domain is linked through the same dependent variables. The model uses the following equations:

$$B = \mu_0 H \tag{6.4}$$

this is implemented across the entire domain, which includes both the superconducting and air domains, where Maxwell's equation used in the model is:

$$\nabla \times E = -\frac{dB}{dt} = -\mu_0 \frac{dH}{dt} \tag{6.5}$$

$$\nabla \times H = J \tag{6.6}$$

E-J power law is implemented with the following equation:

$$E = E_0 \left(\frac{J}{J_0(B)} \right)^{n-1} \frac{J}{J_c} \tag{6.7}$$

E_0 is the electric field criteria, given by $10^{-4} V m^{-}1$ to define the critical current of the superconductor. J_c is the current density.

H-formulation in 2D cartesian coordinates

he 2D Cartesian model is considered to be infinitely long along the z-axis, and thus the HTS tape model is also considered to be infinitely long in the z-axis. The input current density J in the superconductor flows in the z-axis direction, as shown in figure 6.2. The electric field also moves along the z-axis, which determines the resistivity with $E_z = \rho J_z$, and the magnetic flux lies in the x-y plane.

Ampere's law is defined as:

$$J_z = \frac{\partial H_x}{\partial x} - \frac{\partial H_x}{\partial y} \tag{6.8}$$

For cartesian coordinates use $H = [H_x; H_y]$ and $E = E_z$ into Faraday's law:

$$\begin{bmatrix} \frac{\partial E_z}{\partial y} \\ -\frac{\partial E_z}{\partial x} \end{bmatrix} = -\mu_0 \mu_r \begin{bmatrix} \frac{\partial H_x}{\partial t} \\ \frac{\partial H_y}{\partial t} \end{bmatrix} \tag{6.9}$$

75
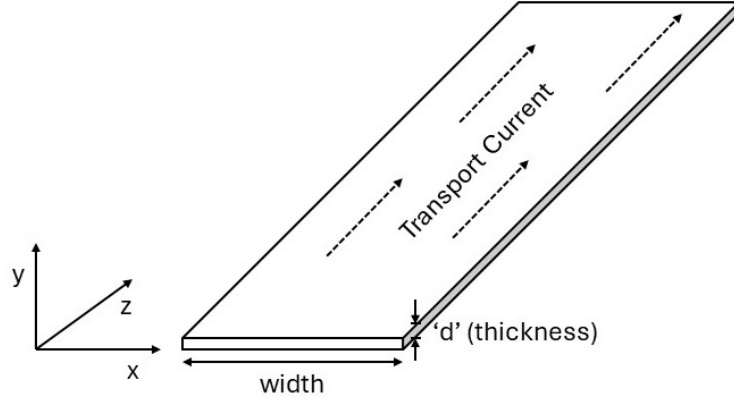
Figure 6.2: Schematic of HTS in a finite element model using H-formulation

$E - J$ power law can be expressed as:

$$E_z = E_0 \left(\frac{J}{J_c} \right)^n \tag{6.10}$$

Substitute equation (6.10) and (6.8) in equation (6.9):

$$\left[\begin{array}{c} \dfrac{\partial \left(E_0 \left(\frac{\frac{\partial H_y}{\partial x} - \frac{\partial H_x}{\partial y}}{J_c} \right)^n \right)}{\partial y} \\[2em] -\dfrac{\partial \left(E_0 \left(\frac{\frac{\partial H_y}{\partial x} - \frac{\partial H_x}{\partial y}}{J_c} \right)^n \right)}{\partial x} \end{array} \right] = -\mu_0 \mu_r \left[\begin{array}{c} \frac{\partial H_x}{\partial t} \\[1em] \frac{\partial H_y}{\partial t} \end{array} \right] \tag{6.11}$$

Equation (6.11), is a partial differential equation with two dependent variables H_x, H_y. With a suitable boundary condition, this equation can be solved with COMSOL FEM software.

6.3.2   Geometrical Overview of 2D FEA Model for Superconducting Busbar

This section describes the geometry of the 2D superconducting busbar developed through a 2D electromagnetic model. The model contains 2 HTS tapes with one copper tape in between the HTS tapes, as shown in figure 6.3. All the associated metal layers of the HTS tape are
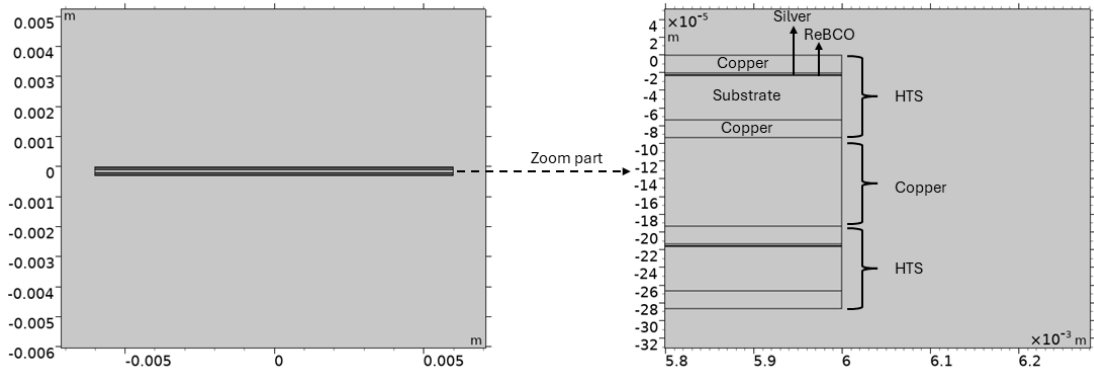
Figure 6.3: Schematic of 2D superconducting busbar model with 2 HTS tapes and 1 copper tape

Table 6.1: Parameters used in 2D model for H-formulation.

Parameter	HTS tapes
Number of HTS tapes	2
Critical current of one tape	100 A
Thickness of copper layer	20 μm
Thickness of silver layer	2 μm
Thickness of substrate	0.2 mm
Thickness of ReBCO layer	1μm
Parameter	**Copper tapes**
Number of copper tape	1
Thickness of copper tape	100μm

also modelled, as depicted in figure 6.3.

The model facilitates the examination of the superconducting busbar's performance under both steady-state and transient conditions. Through modelling analysis, the author has gained insight into the current distribution patterns during steady-state operation and fault conditions. The parameters utilized for modelling are detailed in table 6.1.
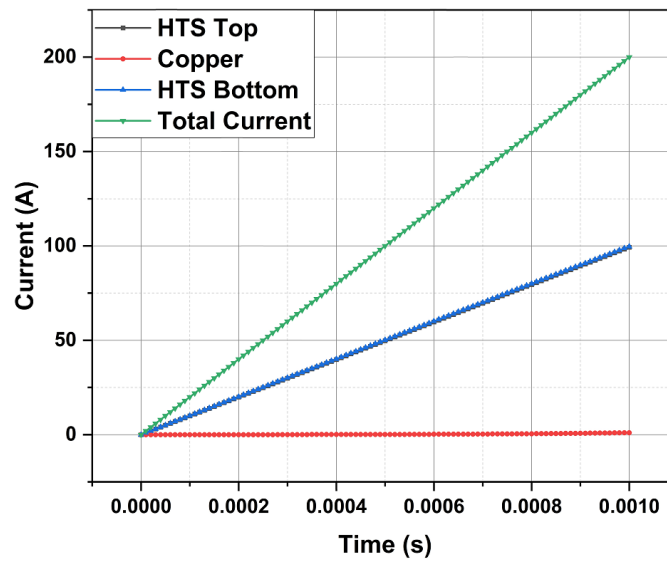
Figure 6.4: Applied current and current in each tape during steady state.

6.3.3   Modelling result analysis

Two models are implemented: one simulating steady-state operation and the other simulating fault-state operation. In the steady-state model, the applied current is less than the critical current, whereas in the fault-state model, the applied current exceeds the critical current. The results of both models are explained here:

Steady state mode:

In the steady-state model, the applied current is 200A, while the critical current of an HTS tape is 100A. Since the model uses 2 HTS tapes, the total critical current is 200A. In this scenario, the applied current does not exceed the critical current, indicating a steady-state operation. Current flows through the HTS tapes during steady-state operation, as the resistance of HTS tape in steady state, is lower than that of the copper tape, as depicted in figure 6.4. No current flows through the copper tape as shown in figure 6.4.

The critical current of the busbar is depicted in figure 6.5. This graph illustrates that the critical current and applied current curves almost coincide but do not intersect. When the applied current curve does not cross the critical current curve, it indicates that the superconductor
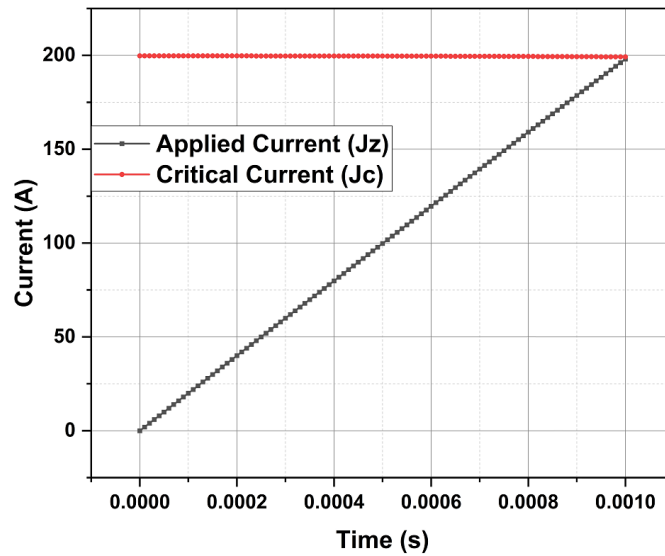
Figure 6.5: Critical current w.r.t applied current during steady state.

remains in its superconducting state.

Fault state mode:

In the fault-state regime, the applied current exceeds the critical current. During a fault state, when the applied current surpasses the critical current, the resistance of the HTS increases, resulting in higher power losses and potential damage to the superconductor. A parallel-connected stabilizer aids in carrying the excess current and enables the superconductor to ride through the fault events. Figure 6.6 illustrates the current distribution through each tape during the fault event. For the fault test, an applied current of 400 A was utilized, while the total critical current of both tapes is 200 A, as shown in figure 6.6. The applied current w.r.t to critical current is shown in figure 6.6, the applied current is 2 times compared to the critical current creating a fault condition.

As the critical current of each HTS tape is 100 A, if the applied current surpasses 100 A, resistance will begin to be generated in the HTS tape and current will start diverting into the copper tape. Figure 6.6 illustrates that above 100 A of applied current, current diversion into the copper tape occurs. This helps to reduce the current in the HTS tapes, as depicted in figure 6.7. In figure 6.7, it is clear that the current is restricted in HTS due to an increase
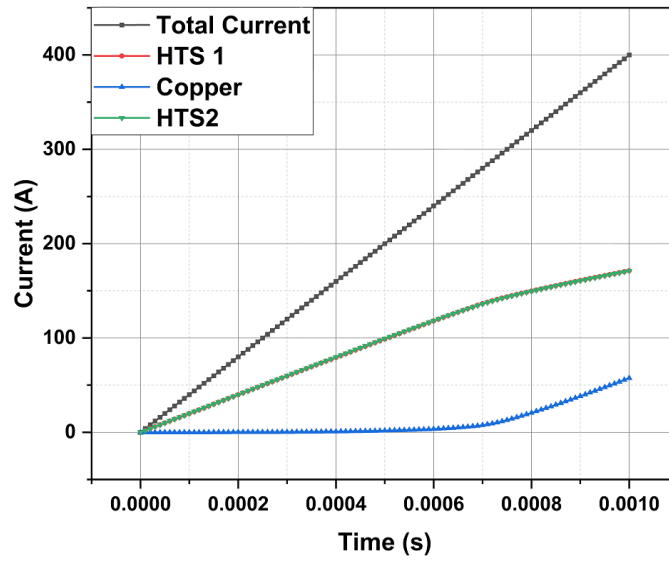
Figure 6.6: Applied current and current in each tape during fault state.
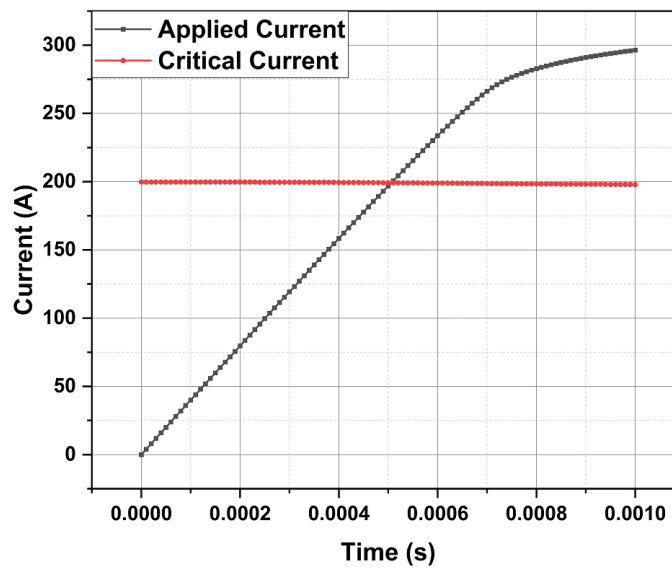
Figure 6.7: Critical current w.r.t applied current during fault state.

in resistance, prompting the diversion of current to the copper tape. This mechanism aids in reducing the current in the HTS tape, facilitating the HTS busbar to ride through the fault event

6.4   Experimental analysis of fault-tolerant design

The same experimental setup used to assess the effect of the gap on the field-dependent critical current is used for testing the fault tolerance of the busbar, as depicted in figure 5.14. Fault currents are generated via a programmable DC power supply for a duration of 1 ms. The power supply can operate under a range of slew rates, from 0.0001 to 999.99 A/msec. The time period of the current pulse is adjusted through the slew rate. The operation of the power supply is controlled through LabVIEW software. The superconducting busbar is connected to the power supply in series, as shown in figure 5.14. Data acquisition is also conducted using the same setup as explained in section 5.3.2.

6.4.1   Geometrical description

The geometries of the superconducting busbars are shown in figure 6.8. The two superconducting busbar prototypes are developed and tested against fault currents. Both superconducting busbar designs are compared based on the experimental results. The steps of superconducting busbar prototyping are explained in section 5.3.1. The fault-tolerant busbar consists of 5 HTS tapes and 4 copper tapes, whereas the other design consists of only 5 HTS tapes. The parameters used for designing the superconducting busbar are mentioned in table 6.2.
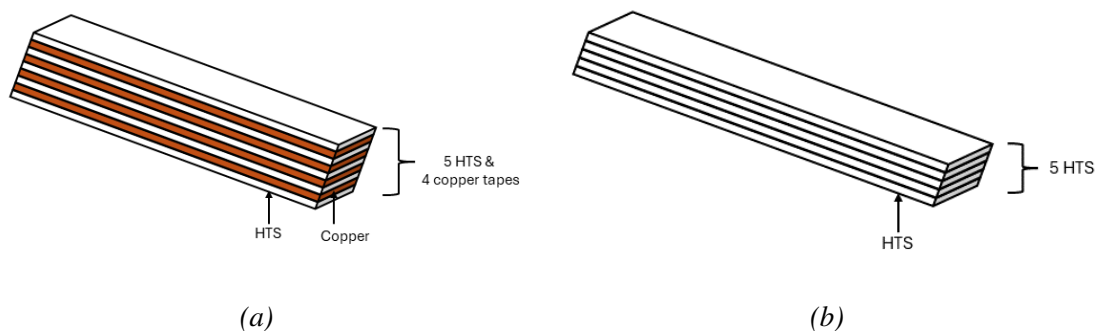
Figure 6.8: Geometries of both samples tested against faults. (a) Busbar with 5 HTS tapes and 4 copper tapes design, (b) Busbar with 5 HTS tapes design.

81

Table 6.2: Result comparison [10].

Parameter	5 HTS tapes	5 HTS tapes and 4 Cu tapes
Manufacturer	Shanghai Superconductor	Shanghai Superconductor and RS component
Critical current	460 A	480 A
Maximum fault tolerance	90 A	420 A
Width of HTS	4 mm	4 mm
Width of Cu	NA	4 mm
Thickness of Cu	NA	100 μm
Fault tolerance compares to IC	19.5 %	87.5 %
Maximum power loss tolerance	0.20 W/cm	76 W/cm

6.4.2   Experimental analysis

Experiments are conducted on both samples against fault current. Initially, critical current tests are conducted to determine the maximum current carrying capacity of both busbars. The figure illustrates that the maximum current safely carried by the superconducting busbar consisting of 5 HTS tapes is 460 A, while the busbar consisting of 5 HTS and 4 copper tapes can carry 480 A safely. Current values exceeding these thresholds are considered as fault current, as indicated in table 6.2. Below the threshold current value, the busbar operates in a steady-state condition, with current flowing only in HTS tapes, as shown in figure 5.18. The V-I curve in figure 5.18 demonstrates that current flows solely in HTS tapes, as the copper V-I curve is linear. However, once the current exceeds the critical current or threshold value, the operating state changes from steady state to fault state. During this state, current starts diverting from HTS tapes to copper tapes due to the high resistance offered by the HTS tapes. This section draws a comparison between steady state and fault state to assess the efficiency of fault tolerant busbar design, with results summarized in table 6.2.
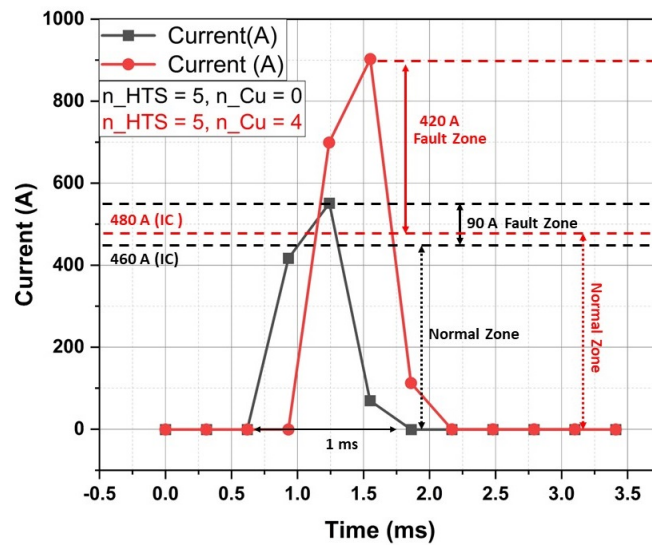
Figure 6.9: Fault test on 5 HTS tapes and 4 Cu tapes sandwiched between 5 HTS tapes [10].

Fault test

Multiple fault tests have been conducted on busbar samples, with the fault current pulse magnitude increasing step by step. Initially, fault currents are of the magnitude equal to the critical current, then progressively increased until busbar samples burn. This approach aids in determining the maximum magnitude of fault current that superconducting busbar samples can withstand, and also ensures that the superconducting busbar accommodates multiple fault events below a threshold magnitude of fault. Figure 6.9 illustrates the comparison of maximum fault tolerance exhibited by both designs during the fault test. The sample rate is set to 500 Hz for the fault pulses.

The threshold criteria for critical current, according to 1 $\mu V/cm$, are 460 A and 480 A for both designs, represented by black and red dotted lines, as shown in figure 6.9. Above this threshold line, the superconducting busbar undergoes a fault event. The busbar with only HTS tape design demonstrates a fault tolerance of 19.4% compared to critical current; this fault tolerance is due to the other layers associated with the superconducting layer. In the fault tolerance design, the busbar with 5 HTS tape and 4 copper tapes design demonstrates an 87.5% fault tolerance compared to critical current. These are the maximum peak fault current limits: above this, the busbar samples will burn. The results show that the busbar design with
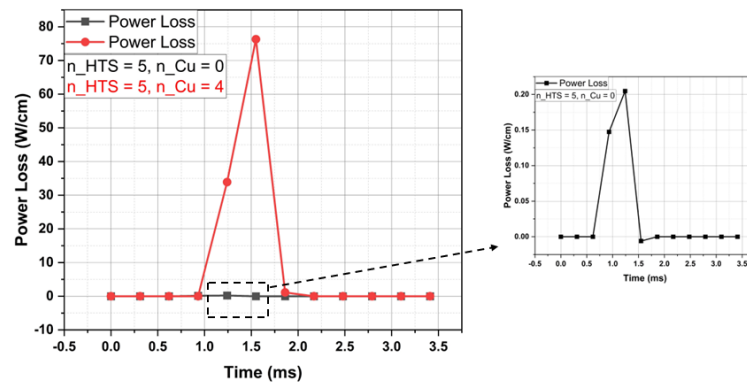
Figure 6.10: Power loss during fault test.

extra copper in between HTS tapes is more fault-tolerant compared to the busbar design with only HTS tapes.

The power loss during the fault test is shown in figure 6.10. This represents the maximum power loss tolerated by both designs. The maximum power tolerated by the superconducting busbar design with only HTS tapes is $0.20\ W/cm$, whereas the superconducting busbar design with copper sandwiched between HTS tapes is $76\ W/cm$. The results show that the busbar with 5 HTS and 4 copper tapes is capable of tolerating more power loss compared to the busbar with only HTS tapes design.

6.5   Conclusion

In this chapter, a fault-tolerant design for superconducting busbars is presented and tested against fault currents. During fault event the current through the HTS tape exceeds it's critical current limit and forcing current to jump from superconducting layer to metal layers. During fault event HTS offers very high resistance, which produce high joule heating due to high current flowing through the metal part of the tape that could damage the tape. To prevent damage during a fault event, the busbar design is equipped with a fault ride-through mechanism. The fault ride-through mechanism is supported through copper tapes added in between the HTS tapes, during fault event when HTS offers high resistance the current starts flowing through the copper tape and saves HTS from burning. In this section, multiple HTS

tape busbar design is tested against fault currents. Two prototypes are developed: one with a fault-tolerant design, consisting of 4 copper tapes sandwiched between 5 HTS tapes, and the other with 5 HTS tapes. The fault-tolerant design includes an extra copper stabiliser tape connected in parallel to the superconductor, which accommodates extra current during a fault and helps dissipate extra power, thus protecting the superconductor from damage. The design is also tested against multiple fault currents of different magnitudes, demonstrating the reliability of the superconducting busbar. The results clearly indicate that the fault-tolerant design is not only able to ride through fault events but also tolerate more power loss compared busbar that contains only HTS tapes.

7

Low-resistive joints for superconducting
busbars

7.1   Introduction

Superconductors offer promising solutions for high-current transmission applications due
to their high power density and almost zero power loss when carrying DC power. These
advantages are highly desirable for applications requiring high current transmission, such as
in aluminium electrolysis plants [153], substation links [154], chlorine electrolysis [155], and
potentially in all-electric aircraft power distribution systems. Due to the crystal structure of
superconductors, the length of the HTS tape is limited, necessitating the need to join them.
While joining the HTS tapes together, it is important to minimize the resistance of the joint.
High joint resistance can result in high joule heating, which may reduce the critical current
over the joint area and increase the cooling penalty during operation. This underscores the
critical importance of the joint, necessitating a thorough investigation and characterisation.

 Few groups are working on soldered joints with 2G HTS tapes [156, 157, 158, 159, 155].
Two types of joints are reported in the literature for joining HTS tapes: the lap-to-lap joint,
also known as the bridge joint, and the butt joint, also known as the edge joint. Lap-to-lap
joints are the most commonly used and successful due to metallic interfaces, whereas butt

joints are more susceptible to mechanical damage [160, 161]. Joint resistance also varies from manufacturer to manufacturer as different manufacturers have different coatings that vary joint resistance ranging from $2 - 300\ n\Omega - cm^2$ [161].

This chapter explores joints for superconducting busbars. A busbar is a component in power distribution systems that connects the power source to the load, and there may be multiple loads connected through the busbar. As a result, joints are required to connect multiple sources to multiple loads. In this work, the author has designed joints to ensure that the busbar maintains both fault tolerance and reduced effects of self-field on critical current. In electric aircraft applications, superconducting busbars will be used to connect the power source to the load (propulsion unit), as illustrated in figure 4.3. The author has implemented $180°$ and $90°$ joints on the superconducting busbar. To ensure the reliability and durability of the superconducting busbar, power and thermal cycling tests have been conducted to check for any potential degradation in the resistivity of the joints.

7.2   Fabrication process of busbar with $180°$ and $90°$ joints

7.2.1   Joint process

Two types of joints were implemented, resulting in the development of two prototypes. In one prototype, $180°$ joints were used to join 5 HTS tapes together, with 4 copper tapes sandwiched between the HTS tapes. In the second prototype, $90°$ joints were implemented to join 5 HTS tapes, again with 4 copper tapes sandwiched between them. Shanghai 2G YBCO 4 mm wide tapes were used for the prototypes. The superconducting busbar follows the same design advantages as explained in previous sections, which include a reduced effect of the self-field on critical current and fault tolerance.

The steps to fabricate the joints are developed by the author of this thesis during this PhD project. The steps to join HTS tapes are explained here:

Step 1: Understanding the superconducting layer of HTS tape is crucial for fabricating low-resistive joints, ensuring that current does not flow through the substrate side of the HTS

tape, which would lead to high resistance. Join the superconducting side of the HTS tape with the superconducting side of the other HTS tape.

Step 2: Coat the HTS and copper tape with flux to remove oxidants from the surface of the tapes.

Step 3: Apply Pbsn-based solder and coat the surface of the HTS and copper tapes with it.

Step 4: Coat the HTS and copper tapes with flux again, so that they can easily stick together for further process.

Step 5: Arrange the HTS tapes and copper tapes according to the geometry as shown in figure 7.1, and 7.5.

Step 6: Tied the HTS and copper tapes assembly with the Kapton tape, so that the tapes will be secure together.

Step 7: Put the assembly in the respective copper former and apply mechanical pressure with the help of the screws as shown in figure 7.2, and 7.6.

Step 8: Place the former in the preheated oven and set the temperature to 220°C.

Step 9: Let the sample bake for 20-25 minutes, then take it out and let it cool to room temperature before demoulding it from the former.

7.2.2 Mechanical structure of $180°$ joint busbar

$180°$ lap-to-lap joint is implemented to connect 5 HTS tapes, the mechanical structure of the superconducting busbar with $180°$ joint is shown in figure 7.1. The design incorporates a stacking concept, where HTS tapes and copper tapes are layered together. This stack not only facilitates the effective conduction of electricity but also provides structural integrity to the busbar. The careful integration of copper tapes is vital, as they help dissipate heat generated during operation, thereby protecting the HTS tapes from thermal stress and potential degradation, as explained in section 6.

A copper former is essential for housing the superconducting busbar assembly, applying mechanical pressure, and then baking the assembly in the oven to achieve the desired mechanical and electrical properties. The design and shape of the former are critical, as they provide
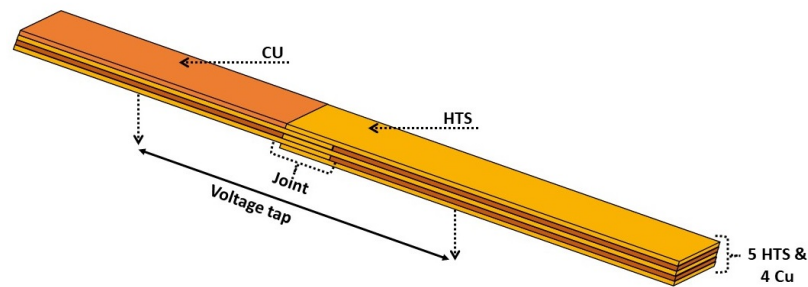
Figure 7.1: 5 HTS tapes joins with $180°$ lap-to-lap joint with 4 copper tapes sandwiched between HTS tapes.

the necessary mechanical structure and support to the busbar. For a $180°$ joint, the former is illustrated in figure 7.2. The length of the former is determined by the size of the required superconducting busbar and the dimensions of the oven used for the heating process.

To prevent the busbar from soldering to the copper former during the heating process, Kapton tape is applied to the surface of the former. This high-temperature-resistant tape acts as a protective barrier, ensuring that the molten solder does not bond the busbar to the copper former. The application of Kapton tape is a crucial step, as it maintains the integrity of the busbar assembly and allows for easy removal of the former after the baking process.

During the heating process, mechanical pressure is applied to the superconducting busbar using a combination of nuts and screws. This pressure ensures that the HTS tapes and copper tapes are tightly joined, creating a robust and reliable electrical connection. The mechanical pressure helps to eliminate any gaps or misalignments between the tapes, which could otherwise lead to increased electrical resistance or mechanical failure. The role of the copper former goes beyond merely holding the assembly together; it also aids in the even distribution of heat during the baking process. An even heat distribution is essential for ensuring that the solder flows correctly and that all components of the busbar are properly bonded. The former's design must therefore account for thermal expansion and other factors that could affect the uniformity of the heating process.
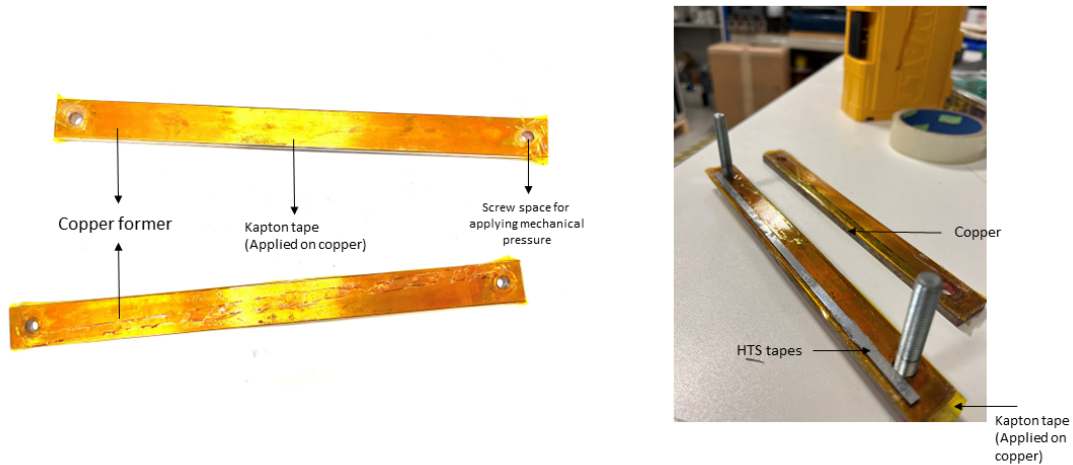
Figure 7.2: Copper former for $180°$ lap-to-lap joint.

Assessment $180°$ lap-to-lap joint length

To assess the length of the $180°$ joint, a range of experiments was conducted with joint lengths from 1 cm to 4 cm. The lap-to-lap joint length was adjusted within this range, and the V-I characteristics were measured and compared with HTS tape having no joint, as shown in figure 7.3. During the DC test figure 7.3 shows that, according to the $1\mu V$ criterion, the voltage of the 3-4 cm joint is comparable to that of the HTS tape with no joint. The joint within this length range not only matches the critical current of a jointless tape but also exhibits superior electrical performance in terms of resistance and power loss.

During the DC test, the resistance and power loss of the joints is measured, as shown in figure 7.4. The results reveal a clear trend: the resistance of the joint decreases as the joint area increases. The resistance of 3 cm to 4 cm joints was lower, measured at 100 $n\Omega$, and the power loss was reduced, measured at 0.001 W. This performance is superior compared to shorter joints, with 1 cm to 2 cm range, which exhibited higher resistance and more power loss. Longer joint lengths provide better electrical connectivity, which in turn reduces resistance and minimizes power loss. This is crucial for maintaining the efficiency and reliability of superconducting systems, especially in high-performance applications.
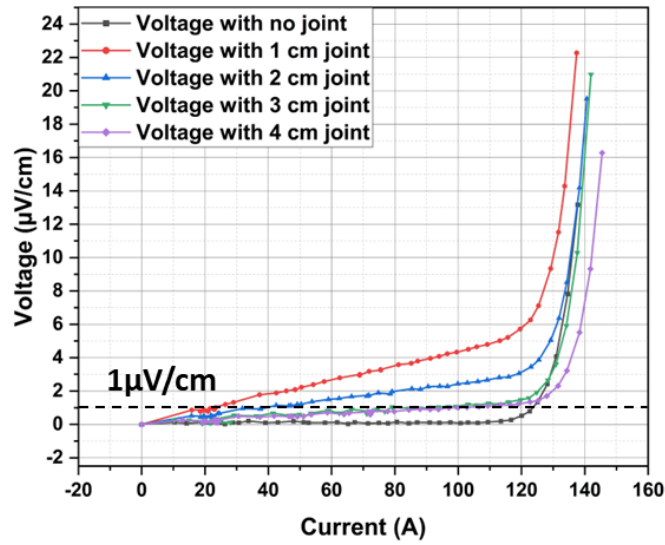
Figure 7.3: V-I characteristics of HTS tape without joints and HTS tapes with $180°$ *lap-to-lap joints, varying in length from 1 cm to 4 cm.*
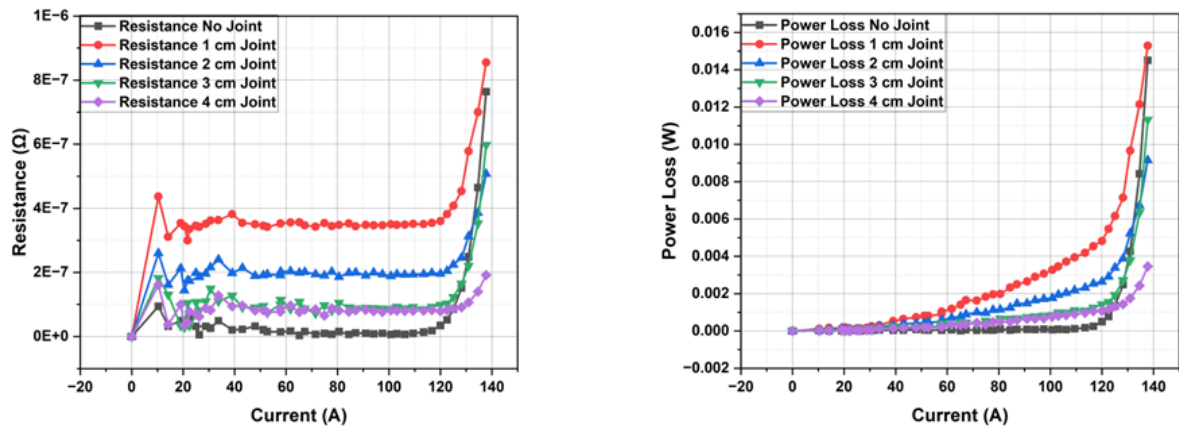
Figure 7.4: Resistance and power loss w.r.t current of HTS tape without joints and HTS tapes with $180°$ *lap-to-lap joints, varying in length from 1 cm to 4 cm.*

In light of these results, the $180°$ lap-to-lap joint with a length of 3-4 cm is used for subsequent prototypes.

7.2.3   Mechanical structure of $90°$ joint busbar

A $90°$ lap-to-lap joint is implemented to connect 5 HTS tapes with 4 copper tapes. The mechanical structure of the busbar, which includes these joints, is illustrated in figure 7.5. Two $90°$ joints are implemented, the design of the $90°$ joint is inherently more complex compared to the $180°$ joint due to the spatial arrangement and interaction between the HTS and copper tapes. In the $90°$ joint configuration, the copper tapes between the HTS tapes tend to overlap at the points of intersection near joints 1 and 2, as shown in figure 7.5. This overlapping poses a significant challenge because it can cause damage to the HTS tape during the mechanical pressing process, which is a critical step in forming the joint. The mechanical pressing is necessary to ensure that the HTS tapes and copper tapes are securely joined, but any misalignment or overlapping can compromise the integrity of the HTS tapes. To address this issue, the copper tapes must be cut with precision to prevent any overlap at the intersections. Each copper tape needs to be measured and trimmed accurately to fit within the designated space without interfering with the HTS tapes. The precise cutting and placement of the copper tapes are essential to maintaining the structural and electrical integrity of the joint. Additionally, the complexity of the $90°$ joint design demands careful consideration of the thermal and mechanical stresses that the joint will endure during operation. Ensuring that the copper tapes do not overlap not only prevents physical damage but also minimizes potential electrical resistance and heat generation at the joint. These factors are crucial for the reliable performance of the superconducting busbar in its intended application.

Copper formers are employed to house the $90°$ joint busbar assembly, as illustrated in figure 7.6. These formers play a crucial role in providing structural support and ensuring the proper alignment of the busbar components during the assembly process. To prevent the solder from inadvertently bonding the busbar to the copper former during the heating process, Kapton tape is applied to the surfaces of the copper former. This precaution is necessary because there is a high likelihood that the solder will melt from the tapes and come into contact with the copper. By layering Kapton tape on the surfaces of the copper former, a protective barrier is created that prevents this unwanted adhesion.
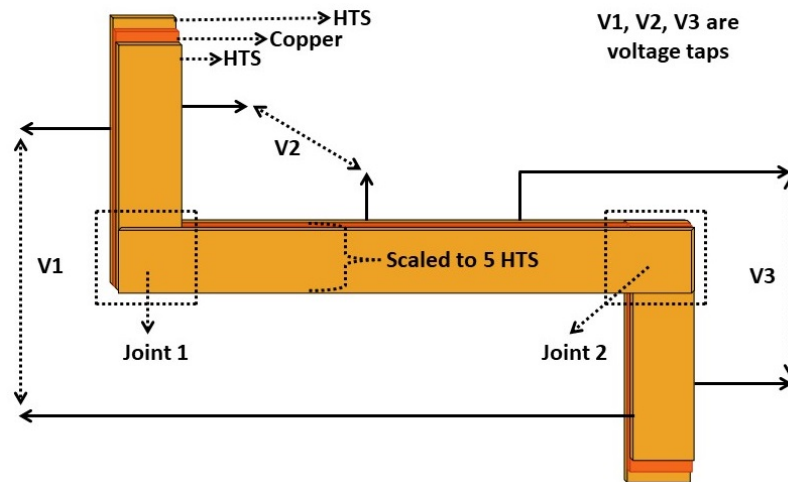
Figure 7.5: 5 HTS tapes joins with $90°$ lap-to-lap joint with 4 copper tapes sandwiched between HTS tapes.

During the assembly process, screws are used to apply mechanical pressure to the HTS tapes, ensuring they are firmly joined together while undergoing heat treatment. This mechanical pressure is essential for achieving a strong, reliable joint. Unlike the $180°$ joints, the $90°$ joints present a unique challenge due to spatial area. Due to the design constraints and the spatial limitations around the joint area, there is no available room to alter the area of the joint. Consequently, all $90°$ joints have a fixed area of 0.16 cm^2.

However, in the busbar design, copper tapes also need to be integrated alongside the HTS tapes. This integration introduces significant challenges when using angles other than $90°$ or $180°$. Specifically, for alternative angles, the copper tapes must be precisely cut and positioned to fit seamlessly between the HTS tapes while ensuring that the copper does not become part of the superconducting joint itself. This precision cutting and fitting process can be exceedingly complex and may lead to design inefficiencies.

Furthermore, $180°$ and $90°$ joints have been demonstrated to offer superior mechanical strength compared to joints created at other angles. This mechanical robustness is critical for maintaining the structural integrity of the busbar, especially under operational stresses such as thermal cycling and fault currents. The mechanical strength provided by these joint angles also simplifies the manufacturing process, as they allow for a more straightforward integration
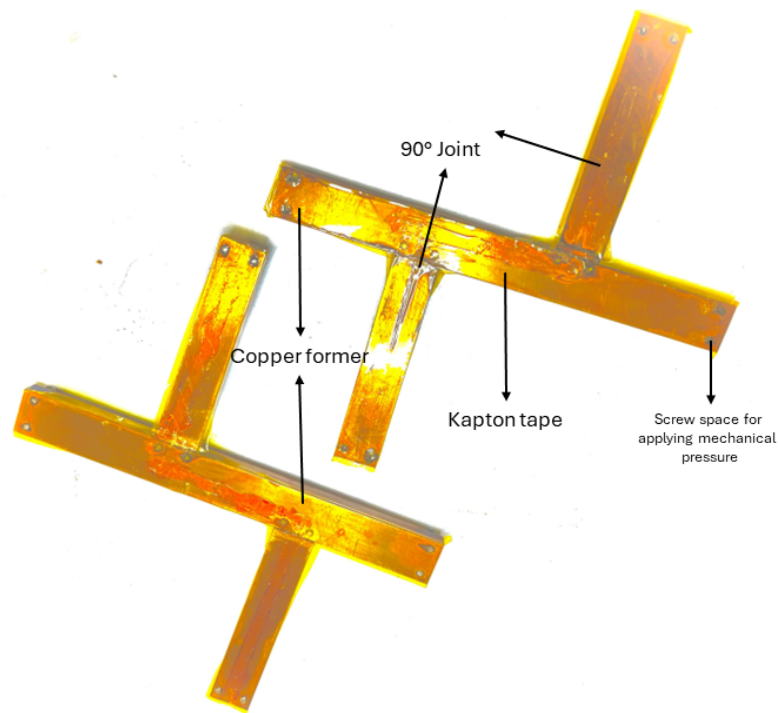
Figure 7.6: Copper former for two $90°$ *lap-to-lap joints.*

of copper and HTS tapes without compromising the joint's performance or reliability.

Given these considerations, 90° and 180° joints were prioritized in the busbar design due to their practicality, mechanical strength, and compatibility with the integration of copper tapes. Future investigations may further explore the feasibility and benefits of alternative angles, but the current approach ensures an optimal balance between ease of manufacturing, mechanical reliability, and electrical performance.

7.3   Experimental results

The superconducting busbar with 180° and 90° joints was tested to evaluate its performance and durability. Initially, the busbar was subjected to DC current tests to assess its immediate electrical properties. Following these tests, the busbar underwent a series of power and thermal cycling to identify any potential degradation in its electrical parameters over time. The power cycling test involves subjecting the busbar to its critical current of 600A while undergoing

thermal cycling. During the thermal cycle, the busbar is immersed in liquid nitrogen (LN2) at a temperature of 77K, and the current is applied until it reaches to it's critical current. After each test cycle, the busbar is warmed back to room temperature before being re-immersed in LN2 for the next cycle. This process of alternating between power application and thermal cycling is repeated a total of 11 times to evaluate the busbar's performance and reliability under these conditions.

During the power cycling tests, the busbar was subjected to electric currents 11 times, allowing us to observe how repeated electrical loading impacts its performance. Simultaneously, the thermal cycling process exposed the busbar to temperature fluctuations 11 times, replicating the thermal stresses. This dual testing approach was critical in providing a comprehensive assessment of the busbar's reliability and robustness under both electrical and thermal stress.

After completing these rigorous tests, the results were compared to the baseline measurements taken before the cycling processes. The electrical parameters, including resistance, critical current, and any signs of performance degradation, were carefully observed and recorded. This thorough evaluation aimed to ensure that the superconducting busbar maintains its high performance and reliability even after prolonged exposure to varying operational conditions. The data gathered from these tests are crucial for confirming the suitability of the busbar for practical applications, particularly in demanding environments where both electrical and thermal stability are essential.

7.3.1   Superconducting busbar with $180°$ joint

In the developed prototype, 5 HTS tapes are joined together using a $180°$ lap-to-lap joint, as shown in figure 7.7. A 4 cm lap-to-lap joint is employed to ensure a robust connection between the HTS tapes. The same experimental setup described in section 5.3.2 is utilized for these tests. During the test, a DC current of 600 A is passed through the busbar prototype to measure the V-I characteristics. The V-I characteristics obtained during the test are presented in figure 7.8.

Figure 7.7: 5 HTS tapes with 4 copper tapes sandwiched between HTS tapes, join with $180°$ lap-to-lap joint.

Figure 7.8: V-I characteristics of 5 HTS tapes with 4 copper tapes sandwiched between HTS tapes, joined with $180°$ lap-to-lap joint.

The parameters recorded during the testing are detailed in table 7.1. Additionally, the resistance and power loss measured during the test are illustrated in figure 7.9. The results indicate that the joint resistance is less than 100 $n\Omega$, and the power loss across the joint is approximately 0.05 W. These measurements confirm the efficiency and reliability of the $180°$ lap-to-lap joint in maintaining low resistance and minimal power loss, which are critical for the optimal performance of the superconducting busbar in high-current applications.
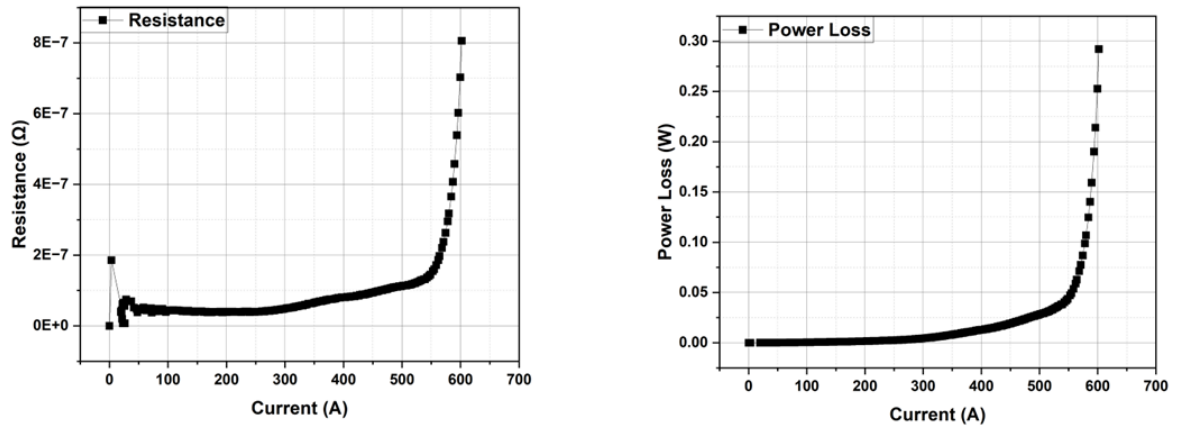
Figure 7.9: Resistance and power loss across 180° *lap-to-lap joint.*

Table 7.1: Measured electrical parameters during testing of superconducting busbar.

Parameter	Busbar with 180° joint	Busbar with 90° joint
Total applied current	600 A	600 A
Number of HTS and copper tapes	5 and 4	5 and 4
Resistance	100 $n\Omega$	-
Power loss	0.03 W	-
Resistance (joint 1)	-	800 $n\Omega$
Power loss (joint 1)	-	0.2 W
Resistance (joint 2)	-	800 $n\Omega$
Power loss (joint 2)	-	0.2 W
Total resistance	-	1.6 $\mu\Omega$
Total power loss	-	0.4 W

Thermal and power cycling

For ensuring the reliability and durability of the busbar, it was subjected to both power and thermal cycling. During power cycling, the busbar underwent electric loading by passing current through it 11 times. In thermal cycling, the busbar was exposed to thermal fluctuations, subjecting it to thermal stress 11 times to observe any potential degradation in its electrical

Figure 7.10: V-I characteristics of 5 HTS tapes with 4 copper tapes sandwiched between HTS tapes, joined with a $180°$ lap-to-lap joint, compared during power and thermal cycling.

parameters.

To evaluate the effects of these cycles, the V-I characteristics were compared to detect any degradation. To avoid excessive repetition and maintain clarity, only the results from test 1, test 5, and test 11 were compared, as shown in figure 7.10. Similarly, the resistance and power loss were analyzed and are presented in figure 7.11. Here too, results from tests 1, 5, and 11 were selected to provide a clear distinction among the different curves without redundant data.

The patterns of the curves remained consistent, indicating minimal degradation throughout the tests. The resistance remains below 100 $n\Omega$ and power loss below 0.03 W during testing, as shown in figure 7.11. The results demonstrate that there was no significant change in resistance or power loss across the joint during the power and thermal cycling. This consistency in performance indicates that the joint is both reliable and durable, maintaining its integrity and efficiency under repeated electrical and thermal stresses. These findings confirm that the $180°$ lap-to-lap joint can withstand the demanding conditions it would encounter in practical applications, ensuring long-term functionality and stability.

Figure 7.11: Comparison of resistance and power loss across $180°$ *lap-to-lap joint during power and thermal cycling.*

7.3.2   Superconducting busbar with $90°$ joint

A prototype has been developed featuring two $90°$ joints, as illustrated in figure 7.12. These joints are implemented to join 5 HTS tapes with 4 copper tapes sandwiched between them. Similar to the $180°$ joint busbar, the $90°$ joint busbar was tested using the same setup described in section 5.3.2. During testing, a DC current of 600 A was passed through the busbar, and the corresponding V-I characteristics were measured. As depicted in figure 7.12, six voltage taps were used to measure the voltage across each individual joint (joint 1 and joint 2) and the overall voltage across both joints. The results of these measurements are detailed in table 7.1. Each joint was carefully monitored to assess its electrical behavior under high current conditions. The voltage taps provided critical data on the voltage drop across each joint, allowing for a detailed analysis of the joint's performance.

The V-I characteristics obtained during the test are shown in figure 7.13. This figure presents both the total voltage across the two joints and the voltage across each individual joint. As expected, the total voltage across both joints is the sum of the voltages across each joint.

The resistance and power loss measured during the test are illustrated in figure 7.14. These results are detailed in table 7.1. During testing, the resistance across joint 1 and joint 2 was
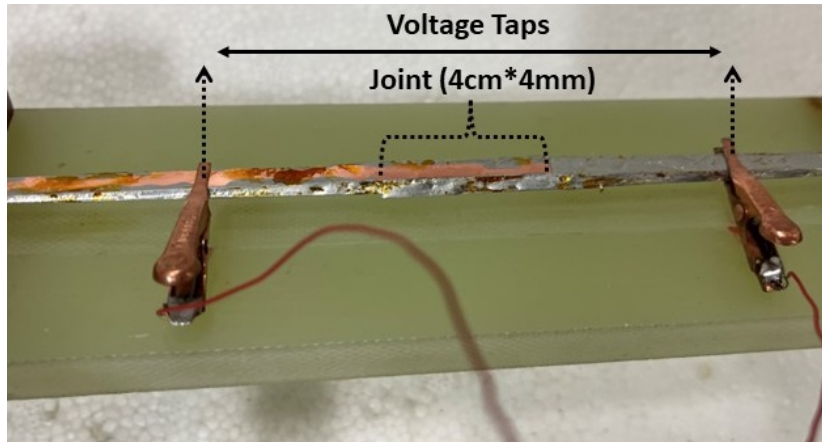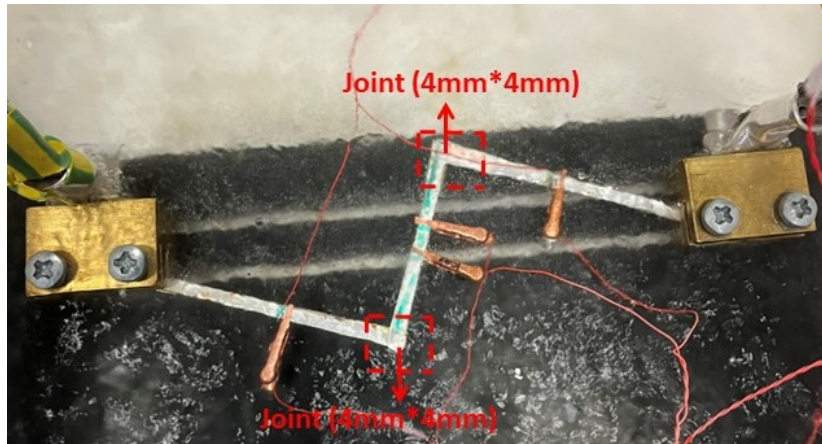
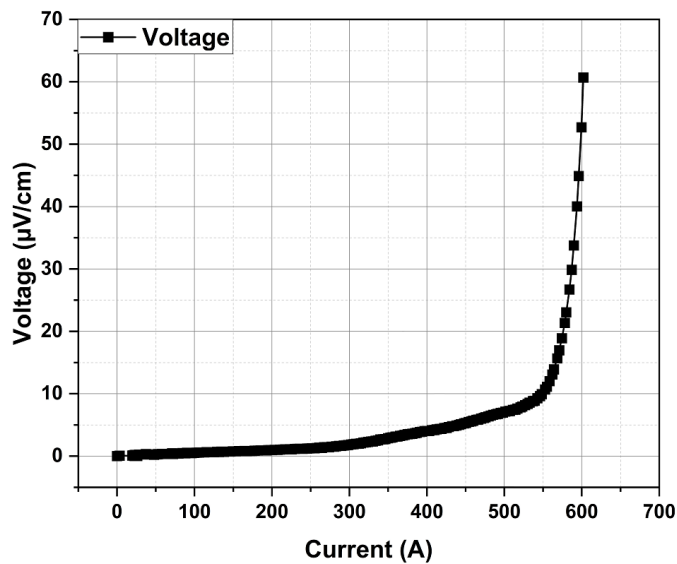*Figure 7.12: 5 HTS tapes with 4 copper tapes sandwiched between HTS tapes, joined with two $90°$ lap-to-lap joints.*
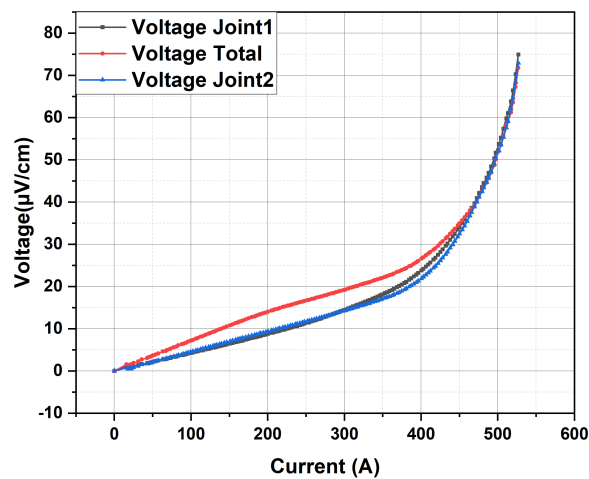
Figure 7.13: V-I characteristics of 5 HTS tapes with 4 copper tapes sandwiched between HTS tapes, joined with a $90°$ lap-to-lap joint.

measured at 800 $n\Omega$ each, while the power loss was recorded at 0.2 W for each joint, as shown in figure 7.14. Consequently, the total resistance across both joints was 1.6 $\mu\Omega$, and the total power loss was 0.4 W.

The consistent V-I characteristics and low resistance values are crucial for the reliability and efficiency of the superconducting busbar in practical applications. The data obtained from these tests provide valuable insights into the busbar's performance. However, the resistance of
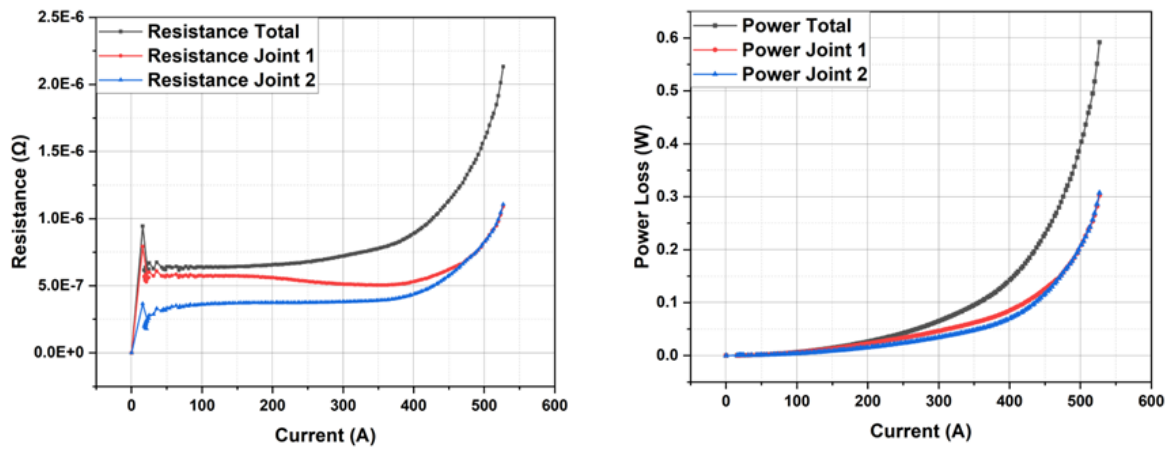
Figure 7.14: Resistance and power loss across $90°$ *lap-to-lap joint.*

the $90°$ joint busbar is higher compared to the $180°$ joint busbar, primarily due to the smaller effective area available for the joints. Figure 7.14 shows that the total resistance across both joints is equal to the sum of the resistances of each joint.

Power and thermal cycling

The busbar was subjected to thermal and power cycling to ensure the reliability and durability of the superconducting busbar joints. The testing process, similar to that described in section 7.3.1, involved repeating thermal and power cycles 11 times. During power cycling, the current was pushed through the superconducting busbar prototype 11 times, while during thermal cycling, the busbar was subjected to temperature fluctuations 11 times. This process tested the effects of electrical loading and thermal stress on the joints of the superconducting busbar. The power and thermal cycling also test the durability and reliability of the joints of superconducting busbar.

V-I characteristics were measured throughout the testing, as shown in figure 7.15. To avoid excessive repetition, results from test 1, test 5, and test 11 were compared. This comparison was conducted to observe any changes in the voltage curve due to power and thermal cycling. Figure 7.15 demonstrates that there was not much change in the behavior of the curve, indicating no degradation in the busbar's performance.
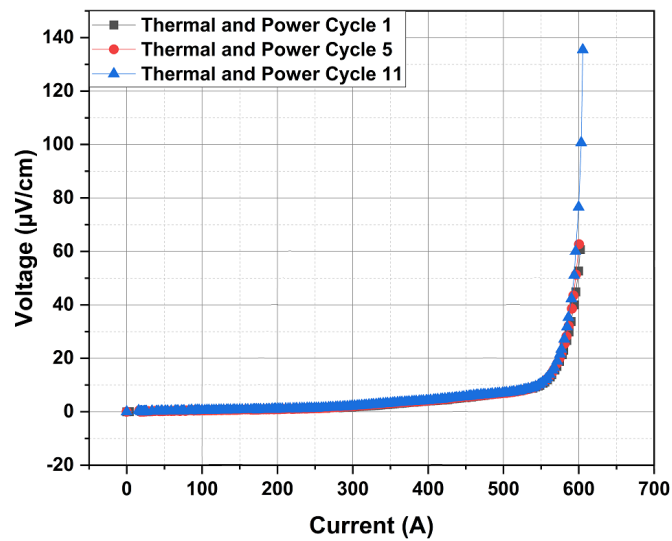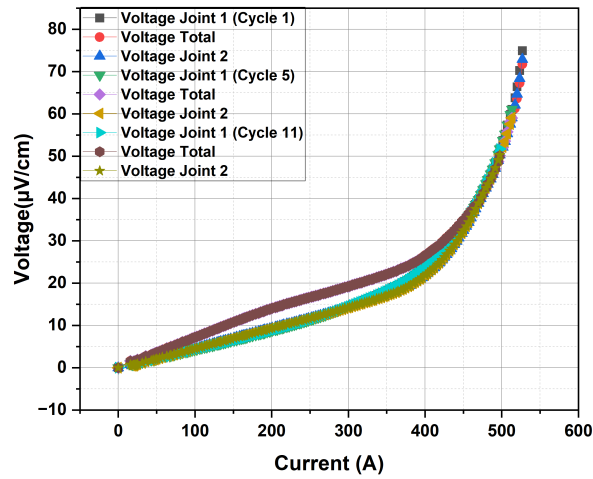
Figure 7.15: V-I characteristics of 5 HTS tapes with 4 copper tapes sandwiched between HTS tapes, joined with two 90° lap-to-lap joints, compared during power and thermal cycling.
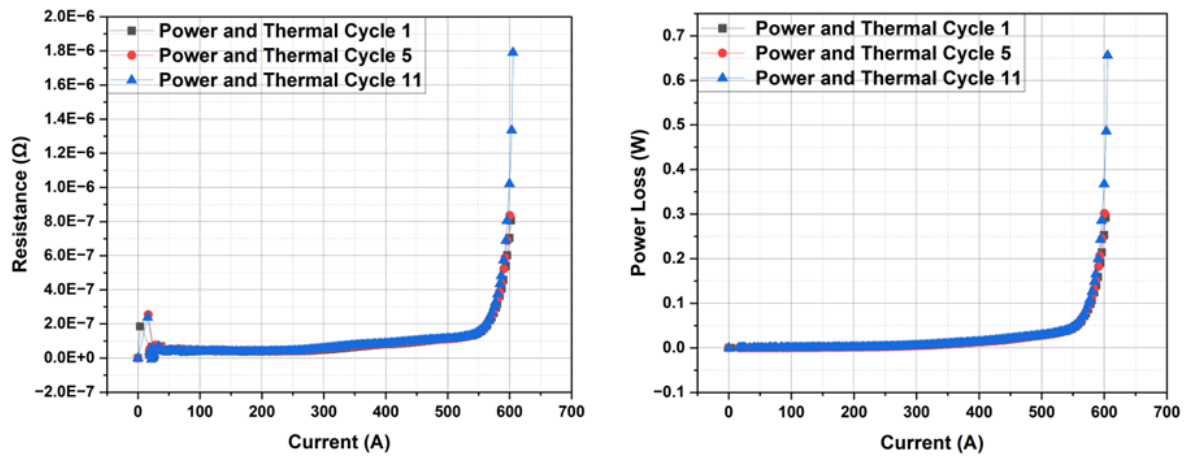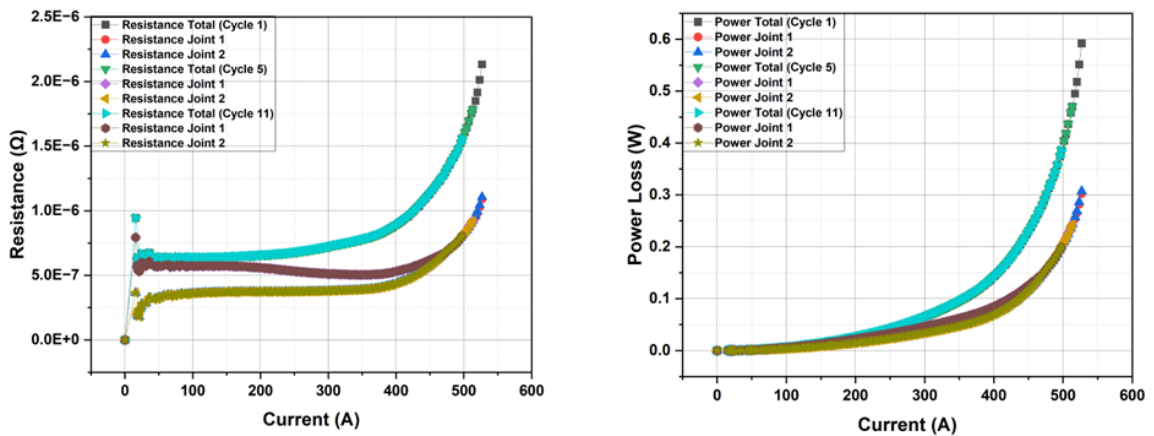

Figure 7.16: Comparison of resistance and power loss across 90° lap-to-lap joint during power and thermal cycling

The resistance and power loss during testing are shown in figure 7.16. This figure displays the resistance across each joint and the total resistance across both joints on the y-axis, while the power loss across both joints and each joint is on the z-axes relative to the current on the x-axis. The resistance and power loss curves were consistent, showing no degradation in resistance during thermal and power cycling. The results indicate that the busbar is reliable and durable.

These consistent findings across multiple tests underscore the robustness of the busbar design. The ability of the joints to maintain low resistance and stable V-I characteristics under repeated electrical and thermal stress confirms the reliability of the superconducting busbar for practical applications. The data obtained provides valuable insights into the long-term performance and durability of the busbar, reinforcing its suitability for high-demand environments

7.4 Conclusion

In this chapter, the author has developed and tested a compact high-temperature superconductor (HTS) busbar design featuring $90°$ and $180°$ joints. Multiple HTS tapes are connected using these joints, which are integral to the busbar's role in a power distribution system, as it carries the current of the entire system and distributes it to various loads. To achieve this, the busbar design incorporates $180°$ and $90°$ joints to join multiple tapes together. The superconducting busbar was tested with DC currents. For the $180°$ joint busbar, the resistance across the joint was measured at 100 $n\Omega$, while the power loss during testing was 0.03 W. The $180°$ joint was tested with different lengths of the lap-to-lap joint. The V-I characteristics of joints of various lengths were compared with those of HTS tape with no joint. It's clear from the experiments that the V-I curve of a 3 cm to 4 cm joint was comparable to that of the HTS tape with no joint. The experimental results also show that the joint resistance depends upon the area of the joint, with an increase in the area of the joint resistance of the joint decreases. For prototypes, a 4 cm long lap-to-lap $180°$ joint was implemented to join 5 HTS tapes together. The busbar was also subjected to thermal and power cycling to assess any potential degradation in electrical parameters. The results indicate little degradation, demonstrating the reliability and durability of the superconducting busbar joints.

Unlike the $180°$ joint, the $90°$ joint can't assessed due to the lack of room to change the joint area. The area of the $90°$ joint could only be increased by using wider HTS tape, such as 6 mm or 12 mm wide HTS tape, but the same 4 mm HTS tape was used for all experiments. Two $90°$ joints were integrated into the superconducting busbar design and tested in a liquid

nitrogen (LN2) environment with DC current. The resistance across each $90°$ joint was measured 800 $n\Omega$, and the power loss across each joint was 0.2 W. The total resistance across both joints was 1.6 $\mu\Omega$, and the total power loss was 0.4 W. The superconducting busbar with $90°$ joints was also subjected to thermal and power cycling to verify the reliability and durability of the joints. The busbar underwent 11 cycles of electrical loading and 11 cycles of thermal fluctuations. No degradation in electrical parameters was observed during testing, further confirming the reliability and durability of the superconducting busbar. These results demonstrate that the busbar, with its low-resistive joints, offers low power loss and can be used in practical applications. The robustness and efficiency of the joints make the busbar suitable for high-performance and reliable power distribution systems.

8

Conclusion and future work

8.1 Introduction

This chapter presents the main findings and conclusions of the thesis, summarising the insights gained and the research contributions made. Furthermore, it provides recommendations for future research at the end of the chapter.

8.2 Summary and conclusions

This thesis presents a thorough investigation into the design of a compact superconducting busbar for high-current applications. The goal is to develop an efficient superconducting busbar design that minimizes the effect of self-field on critical current and ride through fault events. Additionally, the busbar is equipped with $90°$ and $180°$ joints to enhance its performance and versatility.

For high-current applications, HTS tapes offer an efficient solution due to their high current density and low weight. However, the critical current of each HTS tape is limited to a few hundred amps, necessitating the parallel connection of multiple HTS tapes to handle higher currents. When multiple HTS tapes are connected in parallel and carry high current, the resulting magnetic self-field reduces the critical current. This self-field effect cannot

be ignored in high-current scenarios, where multiple HTS tapes are essential for designing a superconducting busbar. To reduce the effect of self-field on critical current, a gap is introduced between the HTS tapes. Using T-A formulation, an electromagnetic model was developed through Finite Element Analysis (FEA). The model revealed that introducing a gap between HTS tapes helps reduce the self-field effect on critical current. This increases the efficiency of the busbar and reduces costs, as fewer HTS tapes are needed to carry the current. To verify the modelling results, experiments were conducted. Prototypes were developed and tested in a liquid nitrogen environment. In these prototypes, the gap was introduced using copper tapes placed between the HTS tapes. The experimental results confirmed that adding a gap between the HTS tapes helps reduce the self-field effect on critical current. This validation underscores the practical benefits of the design, demonstrating that the efficiency of the superconducting busbar can be enhanced, leading to cost savings by requiring fewer HTS tapes to achieve the desired performance. This research highlights the potential of HTS tape configurations to improve the performance and cost-effectiveness of superconducting busbars for high-current applications. The findings contribute to the advancement of superconducting technology, offering a robust and practical approach to addressing the challenges posed by high current densities.

This thesis also explores a busbar design equipped with a fault tolerance mechanism to protect the HTS tapes damage from joule heating. HTS tapes exhibit exponentially increasing resistivity if they exit their superconducting state, a condition that can occur due to critical values being exceeded in current, temperature, or magnetic field. When any of these parameters surpass their critical thresholds, the superconductor transitions to a high-resistance state. The fault ride-through capability of the superconducting busbar ensures that it maintains functionality and reliability during fault events. In the design of author, the copper placed between the HTS tapes serves a dual purpose. Firstly, it reduces the effect of the self-field on the critical current, thus enhancing the busbar's efficiency. Secondly, during fault events, the copper conducts the current and dissipates the heat generated, preventing the HTS tapes from overheating and sustaining damage. To validate this design, two superconducting busbar prototypes were developed and tested against fault current pulses. The first prototype

consisted solely of HTS tapes, while the second prototype incorporated copper tapes between the HTS tapes. Experimental results demonstrated that the second prototype exhibited an 87.5% improvement in fault tolerance compared to the critical current of the busbar. This improved design not only handled higher fault currents but also tolerated more power and Joule heat loss compared to the prototype with only HTS tapes. These findings underscore the significance of integrating copper tapes into the superconducting busbar design. The copper not only enhances the electrical and thermal stability of the busbar but also significantly boosts its fault tolerance, ensuring that the system remains operational and reliable even under adverse conditions. This innovative approach provides a robust solution for high-current applications, where maintaining superconductivity and preventing damage during fault events. This research project contributes valuable insights into the design of superconducting busbars, highlighting the importance of fault tolerance mechanisms in enhancing the performance and durability of HTS-based power distribution systems. The results pave the way for more resilient and efficient superconducting technologies, suitable for a wide range of high-current applications such as electric aircraft.

This thesis also explores the implementation of joints for superconducting busbars, specifically $180°$ and $90°$ joints, used to connect multiple HTS tapes in parallel. In a power distribution system, the primary function of a busbar is to carry the entire system's current and distribute it to various loads. To achieve this, the busbar design is equipped with robust joints. Two prototypes were developed and tested against DC currents. The first prototype featured a $180°$ joint where 5 HTS tapes were joined. In the second prototype, two $90°$ joints were implemented, each connecting 5 HTS tapes. Both prototypes incorporated copper tapes between the HTS tapes to reduce the self-field effect on critical current and to enhance fault tolerance. For the $180°$ joint busbar, the resistance across the joint was measured at 100 $n\Omega$, with a power loss of 0.03 W during testing. The resistance across each $90°$ joint was measured at 800 $n\Omega$, and the power loss for each joint was 0.2 W. The total resistance across both $90°$ joints was 1.6 $\mu\Omega$, with a total power loss of 0.4 W. Both busbar prototypes were subjected to power and thermal cycling. During power cycling, the busbars underwent electrical loading 11 times, while during thermal cycling, they were subjected to temperature fluctuations 11

times. The results from each cycle were compared to detect any potential degradation in electrical parameters due to the cycling. The results showed no degradation in electrical parameters during testing, confirming the reliability and durability of the superconducting busbar. These findings demonstrate that superconducting busbars with low-resistive joints offer low power loss and are suitable for practical applications. The robustness and efficiency of the joints make these busbars ideal for high-current applications. By addressing both the design and testing of $180°$ and $90°$ joints in superconducting busbars, this thesis provides valuable insights into the HTS tape connections. The integration of copper tapes not only enhances electrical performance by reducing self-field effects but also improves thermal management and fault tolerance. This comprehensive approach ensures that the busbar can withstand demanding operational conditions, making it a reliable component for the power distribution system.

The results and findings presented in this thesis contribute significantly to the ongoing efforts to enhance the performance and reliability of superconducting busbars. By addressing the specific challenges associated with ReBCO tapes and exploring innovative solutions, this research aims to make superconducting busbars more viable for practical applications. The detailed investigations and experimental validations provided in the thesis will offer valuable insights and potentially pave the way for advancements in the field of superconducting technology.

8.3   Future work

The results presented in this research thesis provide valuable insights into the design of an efficient superconducting busbar for high-current applications. These findings demonstrate how to enhance the performance of the superconducting busbar for high-current scenarios. Based on these findings, several recommendations can be proposed for those pursuing the development of high-current superconducting busbars.

Scaling up the busbar for high currents

The superconducting busbar design presented in this thesis is highly modular and can be scaled up or down based on the specific requirements of different applications. This flexibility allows for a wide range of customization options to meet varying power demands. The modular nature of the design means that components can be added or removed as needed, facilitating easy adaptation to different use cases without the need for a complete redesign. An important aspect of this design is the ability to modify the HTS tapes used within the busbar. While this research primarily utilized 4 mm wide tapes, the design can accommodate wider tapes, such as 12 mm, to increase the current-carrying capacity. By simply adjusting the width of the HTS tapes, the busbar's design current capability can be significantly enhanced. This scalability makes the design highly versatile, capable of being tailored to a broad spectrum of current requirements.

For instance, if larger current capacities are needed for applications such as fusion magnets, the busbar can be tested with wider HTS tapes to handle the extreme current demands. Fusion magnets require exceptionally high current densities to generate the powerful magnetic fields necessary for plasma confinement. Testing the busbar design under such high-current conditions would provide valuable insights into its performance limits and potential enhancements. It would be particularly interesting to observe the performance of the superconducting busbar at these elevated current levels. Such tests could reveal critical information about the thermal and electrical stability of the busbar, the effectiveness of its cooling systems, and its overall efficiency. Additionally, these experiments could highlight any potential areas for improvement, guiding future developments in superconducting technology for high-current applications.

Test the busbar at low temperatures

In this thesis, the superconducting busbar was tested in a liquid nitrogen environment, which is approximately 77 K. At this temperature, the superconducting materials exhibit high performance, but the efficiency and critical current of the superconductor can further increase

with a decrease in temperature. It would be highly informative to conduct additional tests at even lower temperatures to assess how much the efficiency of the busbar design improves compared to its performance at 77 K. For instance, testing the busbar in liquid helium, which can reach temperatures as low as 4.2 K, could provide valuable data on the upper limits of the busbar's performance. These tests would help determine the maximum critical current capacity and overall efficiency of the superconducting busbar under optimal conditions.

Understanding the performance improvements at lower temperatures is crucial for several reasons. Firstly, it would enable a more precise determination of the cooling requirements for various applications. Different superconducting applications, such as power transmission, magnetic resonance imaging (MRI), or fusion reactors, have specific cooling needs based on their operational environments and performance criteria. By identifying the temperature at which the busbar performs optimally, engineers can design more efficient and cost-effective cooling systems tailored to each application's requirements.

Secondly, this knowledge could lead to significant advancements in the design and application of superconducting busbars. For instance, if a particular application demands the highest possible current capacity, operating the busbar at a lower temperature might be necessary. Conversely, for applications where moderate performance is sufficient, maintaining the busbar at 77 K could be more economical and practical.

Optimisation of busbar design

The superconducting busbar design can be further optimized by addressing the resistance of 90-degree joints and conducting extended power and thermal testing to evaluate its long-term performance. Joint resistance between two HTS tapes is directly influenced by the joint area—larger areas result in lower resistance. Consequently, 180-degree joints typically have lower resistance compared to 90-degree joints. To reduce the resistance in 90-degree joints, future research could explore increasing tape width, such as using 12 mm tapes instead of 4 mm tapes. Another approach would be to investigate alternative joining materials, like indium, applied through mechanical pressing to minimize resistance while maintaining joint integrity.

The critical current of HTS tapes decreases with increasing temperature. When exposed

to temperatures above 200^0C, the critical current is reduced. Conventional soldering, which involves high heat to melt solder, poses a risk of degrading the critical current. To mitigate this, mechanical joining methods may provide a viable alternative. However, excessive mechanical stress can also reduce the critical current of HTS tapes. Future work should focus on identifying an optimal joining method that balances thermal and mechanical impacts while preserving the tape's critical current.

The current study subjected the busbar to 11 thermal and power cycles. While these tests provide initial insights, they are insufficient to fully assess the busbar's long-term performance. Future research should subject the busbar to an increased number of cycles to monitor potential degradation in its electrical performance over time. This extended testing will yield valuable data to refine and optimize the busbar design, resulting in a robust, high-performance superconducting busbar suitable for practical applications.

References

[1] Thomas J. Dolan. *"Magnetic Fusion Technology"*. Springer London, 2014.

[2] R.G. Sharma. *"Superconductivity: Basics and Applications to Magnets"*. Springer Cham, 2015.

[3] CP Poole Jr and HA Farach. "R, J. Creswick, Superconductivity", 1996.

[4] Jong O. Kang, Onyou Lee, Young Kyu Mo, Junil Kim, Seungmin Bang, Hongseok Lee, Jae-Hun Lee, Cheolyeong Jang, and Hyoungku Kang. "Degradation characteristics of 2G HTS tapes with respect to an electrical breakdown". *Progress in Superconductivity and Cryogenics*, 17:48–52, 2015.

[5] Alan Preuß. "Development of high-temperature superconductor cables for high direct current applications". `https://library.oapen.org/handle/20.500.12657/46709#:~:text=A%20design%20process%20for%20HTS,tested%20individually%20at%2077%20K.`, 2021. [PhD Thesis].

[6] Wilfried Goldacker, Francesco Grilli, Enric Pardo, Anna Kario, Sonja I Schlachter, and Michal Vojenčiak. "Roebel cables from REBCO coated conductors: a one-century-old concept for the superconductivity of the future". *Superconductor Science and Technology*, 27(9):093001, aug 2014.

[7] Giampaolo Buticchi, Pat Wheeler, and Dushan Boroyevich. "The More-Electric Aircraft and Beyond". *Proceedings of the IEEE*, 111(4):356–370, 2023.

[8] Airbus. "Airbus Technical Notes". `https://hursts.org.uk/airbus-technical/html/index.html`. [Online].

[9] Felix Huber, Wenjuan Song, Min Zhang, and Francesco Grilli. "The T-A formulation: an efficient approach to model the macroscopic electromagnetic behaviour of HTS coated conductor applications". *Superconductor Science and Technology*, 35(4):043003, mar 2022.

[10] Gaurav Gautam, Min Zhang, Weijia Yuan, Graeme Burt, and Daniel Malkin. "Fault Tolerant Superconducting Busbar With Reduced Self-Field Effect on Critical Current Design for All Electric Aircraft". *IEEE Transactions on Applied Superconductivity*, 34(3):1–5, 2024.

[11] TK; Isaksen ISA; Mao H; Liang XZ; Wang WC Fuglestvedt, JS; Berntsen. "Climatic forcing of nitrogen oxides through changes in tropospheric ozone and methane: Global 3D model studies". *Journal Article*, 33:961–978, 1999.

[12] David S. Lee. "The current state of scientific understanding of the non-CO2 effects of aviation on climate ". `https://assets.publishing.service.gov.uk/media/5d19c4fc40f0b609cfd97461/non-CO2-effects-report.pdf`, 2018. [Online].

[13] Directorate-General for Mobility, Directorate-General for Research Transport (European Commission), and Innovation (European Commission. "Flightpath 2050 Europe's Vision for Aviation"". `https://op.europa.eu/en/publication-detail/-/publication/296a9bd7-fef9-4ae8-82c4-a21ff48be673/language-en#`, 2011. [Online].

[14] Pat Wheeler and Sergei Bozhko. "The More Electric Aircraft: Technology and challenges". *IEEE Electrification Magazine*, 2(4):6–12, 2014.

[15] Carlo Cecati, Shoujun Song, and Giampaolo Buticchi. "Special Issue on More Electric Aircraft". *IEEE Transactions on Transportation Electrification*, 6(4):1382–1385, 2020.

[16] Ashkan Barzkar and Mona Ghassemi. "Electric Power Systems in More and All Electric Aircraft: A Review". *IEEE Access*, 8:169314–169332, 2020.

[17] Giampaolo Buticchi, Pat Wheeler, and Dushan Boroyevich. "The More-Electric Aircraft and Beyond". *Proceedings of the IEEE*, 111(4):356–370, 2023.

[18] Aerospace Technology Institute's. "INSIGHT". `https://www.ati.org.uk/wp-content/uploads/2021/09/insight_07-electrical-power-systems.pdf`, 2018. [Online].

[19] Tania C. Cano, Ignacio Castro, Alberto Rodríguez, Diego G. Lamar, Yehia F. Khalil, Laura Albiol-Tendillo, and Parag Kshirsagar. "Future of Electrical Aircraft Energy Power Systems: An Architecture Review". *IEEE Transactions on Transportation Electrification*, 7(3):1915–1929, 2021.

[20] Hendrik Schefer, Leon Fauth, Tobias H. Kopp, Regine Mallwitz, Jens Friebe, and Michael Kurrat. "Discussion on Electric Power Supply Systems for All Electric Aircraft". *IEEE Access*, 8:84188–84216, 2020.

[21] David C. Loder, Andrew Bollman, and Michael J. Armstrong. "Turbo-electric Distributed Aircraft Propulsion: Microgrid Architecture and Evaluation for ECO-150". In *2018 IEEE Transportation Electrification Conference and Expo (ITEC)*, pages 550–557, 2018.

[22] Ryota Sugouchi, Masataka Komiya, Shun Miura, Masataka Iwakuma, Koichi Yoshida, Teruyoshi Sasayama, Takashi Yoshida, Kaoru Yamamoto, Yuichiro Sasamori, Hirokazu Honda, Yoshiji Hase, Masao Shuto, Masayuki Konno, and Teruo Izumi. "Conceptual Design and Electromagnetic Analysis of 2 MW Fully Superconducting Synchronous Motors With Superconducting Magnetic Shields for Turbo-Electric Propulsion System". *IEEE Transactions on Applied Superconductivity*, 30(4):1–5, 2020.

[23] S. Zanegin, N. Ivanov, D. Shishov, I. Shishov, K. Kovalev, and V. Zubko. "Manufacturing and Testing of AC HTS-2 Coil for Small Electrical Motor". *Journal of Superconductivity and Novel Magnetism*, 33(2):355–359, 2020.

[24] Fangjing Weng, Min Zhang, Tian Lan, Yawei Wang, and Weijia Yuan. "Fully superconducting machine for electric aircraft propulsion: study of AC loss for HTS stator". *Superconductor Science and Technology*, 33(10):104002, aug 2020.

[25] Yinka Leo Ogundiran, Antonio Griffo, Jiabin Wang, Shubham Sundeep, Florian Bruder-Mandler, and Tobias Groh. "Insulation Monitoring in Ungrounded Electrical System for More Electric Aircrafts". In *"2023 IEEE Workshop on Electrical Machines Design, Control and Diagnosis (WEMDCD)"*, pages 1–5, 2023.

[26] Michael J. Wolf, Walter H. Fietz, Christoph M. Bayer, Sonja I. Schlachter, Reinhard Heller, and Klaus-Peter Weiss. "HTS CroCo: A Stacked HTS Conductor Optimized for High Currents and Long-Length Production". *IEEE Transactions on Applied Superconductivity*, 26(2):19–24, 2016.

[27] S I Schlachter, J Brand, S Elschner, S Fink, B Holzapfel, A Kudymow, and J Willms. "Test of a DC-HTS Busbar Demonstrator for Power Distribution in Hybrid-Electric Propulsion Systems for Aircraft". *IOP Conference Series: Materials Science and Engineering*, 1241(1):012037, may 2022.

[28] Steffen Elschner, Joerg Brand, Wilfried Goldacker, Markus Hollik, Andrej Kudymow, Severin Strauss, Victor Zermeno, Claus Hanebeck, Stefan Huwer, Wolfgang Reiser, and Mathias Noe. "3S–Superconducting DC-Busbar for High Current Applications". *IEEE Transactions on Applied Superconductivity*, 28(4):1–5, 2018.

[29] H. Kamerlingh Onnes. *"Further experiments with Liquid Helium. G. On the Electrical Resistance of Pure Metals, etc. VI. On the Sudden Change in the Rate at which the Resistance of Mercury Disappears."*, pages 267–272. Springer Netherlands, Dordrecht, 1991.

[30] Adam Mann. "High-temperature superconductivity at 25: Still in suspense". *Nature*, 475(7356):280–282, 2011.

[31] A. A. Abrikosov. "On the Magnetic properties of superconductors of the second group", journal = "sov. phys. jetp", volume = "5", pages = "1174–1182", year = "1957".

[32] J. G. Bednorz and K. A. Müller. "Possible highTc superconductivity in the BaLaCuO system". *Zeitschrift für Physik B Condensed Matter*, 64(2):189–193, 1986.

[33] M. K. Wu, J. R. Ashburn, C. J. Torng, P. H. Hor, R. L. Meng, L. Gao, Z. J. Huang, Y. Q. Wang, and C. W. Chu. "Superconductivity at 93 K in a new mixed-phase Y-Ba-Cu-O compound system at ambient pressure". *Phys. Rev. Lett.*, 58:908–910, Mar 1987.

[34] Jun Nagamatsu, Norimasa Nakagawa, Takahiro Muranaka, Yuji Zenitani, and Jun Akimitsu. "Superconductivity at 39 K in magnesium diboride". *Nature*, 410(6824):63–64, 2001.

[35] Yoichi Kamihara, Hidenori Hiramatsu, Masahiro Hirano, Ryuto Kawamura, Hiroshi Yanagi, Toshio Kamiya, and Hideo Hosono. "Iron-Based Layered Superconductor: LaOFeP". *Journal of the American Chemical Society*, 128(31):10012–10013, 2006. doi: 10.1021/ja063355c.

[36] Zhi-An Ren, Guang-Can Che, Xiao-Li Dong, Jie Yang, Wei Lu, Wei Yi, Xiao-Li Shen, Zheng-Cai Li, Li-Ling Sun, Fang Zhou, and Zhong-Xian Zhao. "Superconductivity and phase diagram in iron-based arsenic-oxides ReFeAsO1 (Re = rare-earth metal) without fluorine doping". *Europhysics Letters*, 83(1):17002, jun 2008.

[37] Hiroki Takahashi, Kazumi Igawa, Kazunobu Arii, Yoichi Kamihara, Masahiro Hirano, and Hideo Hosono. "Superconductivity at 43 K in an iron-based layered compound LaO1-xFxFeAs". *Nature*, 453(7193):376–378, 2008.

[38] A. P. Drozdov, M. I. Eremets, I. A. Troyan, V. Ksenofontov, and S. I. Shylin. "Conventional superconductivity at 203 kelvin at high pressures in the sulfur hydride system". *Nature*, 525(7567):73–76, 2015.

[39] A. P. Drozdov, P. P. Kong, V. S. Minkov, S. P. Besedin, M. A. Kuzovnikov, S. Mozaffari, L. Balicas, F. F. Balakirev, D. E. Graf, V. B. Prakapenka, E. Greenberg, D. A. Knyazev, M. Tkacz, and M. I. Eremets. "Superconductivity at 250 K in lanthanum hydride under high pressures". *Nature*, 569(7757):528–531, 2019.

[40] Francesco Grilli, Frédéric Sirois, Victor M. R. Zermeño, and Michal Vojenčiak. "Self-

Consistent Modeling of the I_c of HTS Devices: How Accurate do Models Really Need to Be?” *IEEE Transactions on Applied Superconductivity*, 24(6):1–8, 2014.

[41] Peter Capper Safa Kasap, editor. pages XXXVI, 1536. Springer Cham, 2017.

[42] David Larbalestier, Alex Gurevich, D. Matthew Feldmann, and Anatoly Polyanskii. “High-Tc superconducting materials for electric power applications”. *Nature*, 414(6861):368–377, 2001.

[43] Günter Fuchs, Wolf-Rüdiger Canders, Hardo May, Ryszard Palka, and Gernot Krabbes. *“High Temperature Superconductor Bulk Materials: Fundamentals, Processing, Properties Control, Application Aspects”*. John Wiley & Sons, 2006.

[44] EM Chudnovsky. “Pinning by oxygen vacancies in high-Tc superconductors”. *Physical review letters*, 65(24):3060, 1990.

[45] David R Nelson and VM Vinokur. “Boson localization and pinning by correlated disorder in high-temperature superconductors”. *Physical review letters*, 68(15):2398, 1992.

[46] Ch. Heinzel, Ch. Neumann, and P. Ziemann. “Anisotropy of the Irreversible Magnetic Behaviour of YBaCuO and TlBaCaCuO Single Crystals–A Comparative a.c.-Susceptibility Study”. *Europhysics Letters*, 13(6):531, nov 1990.

[47] V. Hardy, J. Provost, D. Groult, M. Hervieu, B. Raveau, S. Durčok, E. Pollert, J.C. Frison, J.P. Chaminade, and M. Pouchard. “Strong shift of the irreversibility line in bismuth and thallium based 2212 HTSC single crystals irradiated by 6.0 GeV Pb ions”. *Physica C: Superconductivity*, 191(1):85–96, 1992.

[48] C. P. Bean. “Magnetization of Hard Superconductors”. *Phys. Rev. Lett.*, 8:250–253, Mar 1962.

[49] CHARLES P. BEAN. “Magnetization of High-Field Superconductors”. *Rev. Mod. Phys.*, 36:31–39, Jan 1964.

[50] K Mendelssohn. "Patterns of superconductivity". *Cryogenics*, 3(3):129–140, 1963.

[51] Y. B. Kim, C. F. Hempstead, and A. R. Strnad. "Magnetization and Critical Supercurrents". *Phys. Rev.*, 129:528–535, Jan 1963.

[52] YB Kim, CF Hempstead, and AR Strnad. "Critical persistent currents in hard superconductors". *Physical Review Letters*, 9(7):306, 1962.

[53] Philip W Anderson and YB Kim. "Hard superconductivity: theory of the motion of Abrikosov flux lines". *Reviews of modern physics*, 36(1):39, 1964.

[54] P. W. Anderson. "Theory of Flux Creep in Hard Superconductors". *Phys. Rev. Lett.*, 9:309–311, Oct 1962.

[55] Z. Fisk, J.D. Thompson, E. Zirngiebl, J.L. Smith, and S-W. Cheong. "Superconductivity of rare earth-barium-copper oxides". *Solid State Communications*, 62(11):743–744, 1987.

[56] M. K. Wu, J. R. Ashburn, C. J. Torng, P. H. Hor, R. L. Meng, L. Gao, Z. J. Huang, Y. Q. Wang, and C. W. Chu. "Superconductivity at 93 K in a new mixed-phase Y-Ba-Cu-O compound system at ambient pressure". *Phys. Rev. Lett.*, 58:908–910, Mar 1987.

[57] Peter Capper Safa Kasap, editor. pages XXXVI, 1536. Springer Cham, 2017.

[58] D. Dimos, P. Chaudhari, J. Mannhart, and F. K. LeGoues. "Orientation Dependence of Grain-Boundary Critical Currents in $YBa_2Cu_3O_{7-\delta}$ Bicrystals". *Phys. Rev. Lett.*, 61:219–222, Jul 1988.

[59] D. T. Verebelyi, D. K. Christen, R. Feenstra, C. Cantoni, A. Goyal, D. F. Lee, M. Paranthaman, P. N. Arendt, R. F. DePaula, J. R. Groves, and C. Prouteau. "Low angle grain boundary transport in YBa2Cu3O7 coated conductors". *Applied Physics Letters*, 76(13):1755–1757, 03 2000.

[60] A. Molodyk. "Development of 2G HTS wire production at SuperOx", howpublished = "`https://indico.cern.ch/event/659554/contributions/`

`2708207/attachments/1525929/2385959/2MO404_Alexander_` `Molodyk_Room_34.pdf`", year = 2017, note = "[online]".

[61] Markus Bauer. "Coated conductor HTS tape for energy and magnet applications". `https://indico.cern.ch/event/659554/contributions/` `2716305/attachments/1526325/2386699/1MP7-22_Bauer_Markus.` `pdf`, 2017. [Online].

[62] Alexander Usoskin, Ulrich Betz, Frank Hofacker, Alexander Rutt, Klaus Schlenga, Burkhard Prause, Lucio Rossi, Luca Bottura, Amalia Ballarino, Carmine Senatore, Anna Kario, Wilfried Goldacker, Alexander Meledin, Dmytro Abraimov, and David Larbalestier. "Double-Disordered HTS-Coated Conductors and Their Assemblies Aimed for Ultra-High Fields: Large Area Tapes". *IEEE Transactions on Applied Superconductivity*, 28(4):1–6, 2018.

[63] Drew W. Hazelton. "Progress of Wire Development and Process Improvement on 2G HTS at SuperPower". `https://indico.cern.ch/event/` `659554/contributions/2708203/attachments/1525927/2385960/` `2MO4-02_Drew_Hazelton_Room_34.pdf`, 2017. [Online].

[64] Jae-Hun Lee. "Progress in SuNAM's Coated Conductor Manufacturing". `https://indico.cern.ch/event/659554/contributions/` `2708208/attachments/1525931/2385968/2MO4-05_Hunju_Lee_` `Room_34.pdf`, 2017. [Online].

[65] S. Fujita et al. "Developement of long-length BMO doped REBCO coated conductors by hot-wall PLD process". `https://indico.cern.ch/event/` `659554/contributions/2708204/attachments/1525930/2385967/` `2MO4-03_Shinji_Fujita_Room_34.pdf`, 2017. [Online].

[66] Stuart Wimbush. "A high-temperature superconducting (HTS) wire critical current database". `https://figshare.com/collections/A_high_`

`temperature_superconducting_HTS_wire_critical_current_database/2861821/2`, 2016. [Online].

[67] K. Tsuchiya, A. Kikuchi, A. Terashima, K. Norimoto, M. Uchida, M. Tawada, M. Masuzawa, N. Ohuchi, X. Wang, T. Takao, and S. Fujita. "Critical current measurement of commercial REBCO conductors at 4.2K". *Cryogenics*, 85:1–7, 2017.

[68] Brygida Wojtyniak et al. "Cost-effective production of HTS wires by chemical solution deposition". `https://indico.cern.ch/event/659554/contributions/2708209/attachments/1525932/2385971/2MO406_Michael_Baecker_Room_34.pdf`, 2017. [Online].

[69] Valentina Roxana Vlad, Elena Bartolomé, Marta Vilardell, Albert Calleja, Alexander Meledin, Xavier Obradors, Teresa Puig, Susagna Ricart, Gustaaf Van Tendeloo, Alexander Usoskin, Sergey Lee, Valery Petrykin, and Alexander Molodyk. "Inkjet Printing Multideposited YBCO on CGO/LMO/MgO/Y2O3/Al2 O3/Hastelloy Tape for 2G-Coated Conductors". *IEEE Transactions on Applied Superconductivity*, 28(4):1–5, 2018.

[70] K. Tsuchiya, A. Kikuchi, A. Terashima, K. Norimoto, M. Uchida, M. Tawada, M. Masuzawa, N. Ohuchi, X. Wang, T. Takao, and S. Fujita. "Critical current measurement of commercial REBCO conductors at 4.2K'''. *Cryogenics*, 85:1–7, 2017.

[71] MetOx. "Revolutionary Technology – MetOx." `https://www.metoxtech.com/technology`. [Online].

[72] F. Bloch. "Zum elektrischen Widerstandsgesetz bei tiefen Temperaturen". *Zeitschrift für Physik*, 59(3):208–214, 1930.

[73] Alan Preuss, Walter H. Fietz, Fabian Immel, Sandra Kauffmann-Weiss, and Michael J. Wolf. "Critical Current Degradation of Coated Conductors Under Soldering Conditions". *IEEE Transactions on Applied Superconductivity*, 28(4):1–5, 2018.

[74] Marco Bonura, Pablo Cayado, Konstantina Konstantopoulou, Matteo Alessandrini, and Carmine Senatore. "Heating-Induced Performance Degradation of REBa2Cu3O7–x Coated Conductors: An Oxygen Out-Diffusion Scenario with Two Activation Energies". *ACS Applied Electronic Materials*, 4(3):1318–1326, 2022. doi: 10.1021/acsaelm.2c00065.

[75] Byeongmo Yang, Jiwon Kang, Seungryul Lee, Changlyul Choi, and Younghyun Moon. "Qualification Test of a 80 kV 500 MW HTS DC Cable for Applying Into Real Grid". *IEEE Transactions on Applied Superconductivity*, 25(3):1–5, 2015.

[76] Steffen Elschner, Joerg Brand, Wilfried Goldacker, Markus Hollik, Andrej Kudymow, Severin Strauss, Victor Zermeno, Claus Hanebeck, Stefan Huwer, Wolfgang Reiser, and Mathias Noe. "3S–Superconducting DC-Busbar for High Current Applications". *IEEE Transactions on Applied Superconductivity*, 28(4):1–5, 2018.

[77] Michael J. Wolf, Walter H. Fietz, Christoph M. Bayer, Sonja I. Schlachter, Reinhard Heller, and Klaus-Peter Weiss. "HTS CroCo: A Stacked HTS Conductor Optimized for High Currents and Long-Length Production". *IEEE Transactions on Applied Superconductivity*, 26(2):19–24, 2016.

[78] Shaotao Dai, Liye Xiao, Hongen Zhang, Yuping Teng, Xuemin Liang, Naihao Song, Zhicheng Cao, Zhiqin Zhu, Zhiyuan Gao, Tao Ma, Dong Zhang, Fengyuan Zhang, Zhifeng Zhang, Xi Xu, and Liangzhen Lin. "Testing and Demonstration of a 10-kA HTS DC Power Cable". *IEEE Transactions on Applied Superconductivity*, 24(2):99–102, 2014.

[79] V. E. Sytnikov, S. E. Bemert, Yu. V. Ivanov, S. I. Kopylov, I. V. Krivetskiy, D. S. Rimorov, M. S. Romashov, Yu. G. Shakaryan, R. N. Berdnikov, Yu. A. Dementyev, Yu. A. Goryushin, and D. G. Timofeev. "HTS DC Cable Line Project: On-Going Activities in Russia". *IEEE Transactions on Applied Superconductivity*, 23(3):5401904–5401904, 2013.

[80] J. F. Maguire, J. Yuan, W. Romanosky, F. Schmidt, R. Soika, S. Bratt, F. Durand, C. King, J. McNamara, and T. E. Welsh. "Progress and Status of a 2G HTS Power Cable to Be Installed in the Long Island Power Authority (LIPA) Grid". *IEEE Transactions on Applied Superconductivity*, 21(3):961–966, 2011.

[81] Makoto Hamabe, Hirofumi Watanabe, Jian Sun, Norimasa Yamamoto, Toshio Kawahara, and Satarou Yamaguchi. "Status of a 200-Meter DC Superconducting Power Transmission Cable After Cooling Cycles". *IEEE Transactions on Applied Superconductivity*, 23(3):5400204–5400204, 2013.

[82] Liye Xiao, Shaotao Dai, Liangzhen Lin, Zhifeng Zhang, and Jingye Zhang. "HTS Power Technology for Future DC Power Grid". *IEEE Transactions on Applied Superconductivity*, 23(3):5401506–5401506, 2013.

[83] Liye Xiao, Shaotao Dai, Liangzhen Lin, Yuping Teng, Hongen Zhang, Xueming Liang, Zhiyuan Gao, Dong Zhang, Naihao Song, Zhiqing Zhu, Fengyuan Zhang, Zhifeng Zhang, Xiaochun Li, Zhicheng Cao, Xi Xu, Weiwei Zhou, and Yubao Lin. "Development of a 10 kA HTS DC Power Cable". *IEEE Transactions on Applied Superconductivity*, 22(3):5800404–5800404, 2012.

[84] Xuemin Liang, Shaotao Dai, Zhiyuan Gao, Naihao Song, Yinshun Wang, Dong Zhang, Zhifeng Zhang, Fengyuan Zhang, Zhiqin Zhu, Xi Xu, Tianbin Huang, Xiaochun Li, Zhicheng Cao, Yubao Lin, Liangzhen Lin, and Liye Xiao. "Design of a 380 m DC HTS Power Cable". *IEEE Transactions on Applied Superconductivity*, 20(3):1259–1262, 2010.

[85] Xiaoyuan Chen, Shan Jiang, Yu Chen, Yi Lei, Donghui Zhang, Mingshun Zhang, Huayu Gou, and Boyang Shen. "A 10 MW class data center with ultra-dense high-efficiency energy distribution: Design and economic evaluation of superconducting DC busbar networks". *Energy*, 250:123820, 2022.

[86] Philip C. Michael, Leslie Bromberg, Anthony J. Dietz, Kenneth J. Cragin, and Calman

Gold. "Design and Test of a Prototype 20 kA HTS DC Power Transmission Cable". *IEEE Transactions on Applied Superconductivity*, 25(3):1–5, 2015.

[87] Annabelle Pratt, Pavan Kumar, and Tomm V. Aldridge. "Evaluation of 400V DC distribution in telco and data centers to improve energy efficiency". In *"INTELEC 07 - 29th International Telecommunications Energy Conference"*, pages 32–39, 2007.

[88] M. Tomita, M. Muralidhar, K. Suzuki, Y. Fukumoto, and A. Ishihara. "Development of 10 kA high temperature superconducting power cable for railway systems". *Journal of Applied Physics*, 111(6):063910, 03 2012.

[89] Sung-Kyu Kim, Sun-Kyoung Ha, Jin-Geun Kim, Bo-Geun Jang, Minwon Park, In-Keun Yu, Sangjin Lee, Kideok Sim, and A.-Rong Kim. "Development and Performance Analysis of a 22.9 kV/50 MVA Tri-axial HTS Power Cable Core". *IEEE Transactions on Applied Superconductivity*, 23(3):5400804–5400804, 2013.

[90] D C van der Laan, L F Goodrich, and T J Haugan. "High-current dc power transmission in flexible RE–Ba2Cu3O7 coated conductor cables". *Superconductor Science and Technology*, 25(1):014003, dec 2011.

[91] H. Yumura, Y. Ashibe, H. Itoh, M. Ohya, M. Watanabe, T. Masuda, and C. S. Weber. "Phase II of the Albany HTS Cable Project". *IEEE Transactions on Applied Superconductivity*, 19(3):1698–1701, 2009.

[92] T. Masuda, H. Yumura, M. Watanabe, H. Takigawa, Y. Ashibe, C. Suzawa, T. Kato, Y. Yamada, K. Sato, S. Isojima, C. Weber, A. Dada, and J.R. Spadafore. "Design and experimental results for Albany HTS cable". *IEEE Transactions on Applied Superconductivity*, 15(2):1806–1809, 2005.

[93] Y. S. Choi, D. L. Kim, H. S. Yang, S. H. Sohn, J. H. Lim, and S. D. Hwang. "Progress on the Performance Test of KEPCO HTS Power Cable". *IEEE Transactions on Applied Superconductivity*, 21(3):1034–1037, 2011.

[94] S. Lee, J. Yoon, B. Lee, and B. Yang. "Modeling of a 22.9kV 50MVA superconducting power cable based on PSCAD/EMTDC for application to the Icheon substation in Korea". *Physica C: Superconductivity and its Applications*, 471(21):1283–1289, 2011. The 23rd International Symposium on Superconductivity.

[95] Satarou Yamaguchi, Hiromi Koshizuka, Kazuhiko Hayashi, and Toru Sawamura. "Concept and Design of 500 Meter and 1000 Meter DC Superconducting Power Cables in Ishikari, Japan". *IEEE Transactions on Applied Superconductivity*, 25(3):1–4, 2015.

[96] Byeongmo Yang, Jiwon Kang, Seungryul Lee, Changlyul Choi, and Younghyun Moon. "Qualification Test of a 80 kV 500 MW HTS DC Cable for Applying Into Real Grid". *IEEE Transactions on Applied Superconductivity*, 25(3):1–5, 2015.

[97] C Barth, D C van der Laan, N Bagrets, C M Bayer, K-P Weiss, and C Lange. "Temperature- and field-dependent characterization of a conductor on round core cable". *Superconductor Science and Technology*, 28(6):065007, apr 2015.

[98] W. Goldacker, A. Frank, R. Heller, B. Ringsdorf, S. I. Schlachter, A. Kling, and C. Schmidt. "CRITICAL CURRENTS IN ROEBEL ASSEMBLED COATED CONDUCTORS (RACC)". *AIP Conference Proceedings*, 986(1):461–470, 03 2008.

[99] M. Leghissa, B. Gromoll, J. Rieger, M. Oomen, H.-W. Neumüller, R. Schlosser, H. Schmidt, W. Knorr, M. Meinert, and U. Henning. "Development and application of superconducting transformers". *Physica C: Superconductivity*, 372-376:1688–1693, 2002.

[100] Simon Otten, Anna Kario, Andrea Kling, and Wilfried Goldacker. "Bending properties of different REBCO coated conductor tapes and Roebel cables at T=77 K". *Superconductor Science and Technology*, 29(12):125003, oct 2016.

[101] Y. Terazaki, N. Yanagi, S. Ito, Y. Seino, S. Hamaguchi, H. Tamura, T. Mito, H. Hashizume, and A. Sagara. "Measurement and Analysis of Critical Current of

100-kA Class Simply-Stacked HTS Conductors". *IEEE Transactions on Applied Superconductivity*, 25(3):1–5, 2015.

[102] Y. Terazaki, N. Yanagi, S. Ito, K. Kawai, Y. Seino, T. Ohinata, Y. Tanno, K. Natsume, S. Hamaguchi, H. Noguchi, H. Tamura, T. Mito, H. Hashizume, and A. Sagara. "Critical Current Measurement of 30 kA-Class HTS Conductor Samples". *IEEE Transactions on Applied Superconductivity*, 24(3):1–5, 2014.

[103] Steffen Elschner, Joerg Brand, Wilfried Goldacker, Markus Hollik, Andrej Kudymow, Severin Strauss, Victor Zermeno, Claus Hanebeck, Stefan Huwer, Wolfgang Reiser, and Mathias Noe. "3S–Superconducting DC-Busbar for High Current Applications". *IEEE Transactions on Applied Superconductivity*, 28(4):1–5, 2018.

[104] M. Takayasu, J. V. Minervini, L. Bromberg, M. K. Rudziak, and T. Wong. "Investigation of twisted stacked-tape cable conductor". *AIP Conference Proceedings*, 1435(1):273–280, 06 2012.

[105] Simon Otten, Anna Kario, Andrea Kling, and Wilfried Goldacker. "Bending properties of different REBCO coated conductor tapes and Roebel cables at T=77 K". *Superconductor Science and Technology*, 29(12):125003, oct 2016.

[106] M. Takayasu, J. V. Minervini, L. Bromberg, M. K. Rudziak, and T. Wong. "Investigation of twisted stacked-tape cable conductor". *AIP Conference Proceedings*, 1435(1):273–280, 2012.

[107] Yeonjoo Park, Myungwhon Lee, Heesung Ann, Yoon Hyuck Choi, and Haigun Lee. "A superconducting joint for GdBa2Cu3O7-coated conductors". *NPG Asia Materials*, 6(5):e98–e98, 2014.

[108] Makoto Takayasu, Luisa Chiesa, and Joseph V. Minervini. "Development of Termination Methods for 2G HTS Tape Cable Conductors". *IEEE Transactions on Applied Superconductivity*, 24(3):1–5, 2014.

[109] Michael J. Wolf, Walter H. Fietz, and Alan Preuss. "Investigation of HTS Cross-Conductor Joints, Connectors, and Terminations". *IEEE Transactions on Applied Superconductivity*, 27(4):1–5, 2017.

[110] Jaakko Samuel Murtomäki, Glyn Kirby, Jeroen van Nugteren, Pierre-Antoine Contat, Oscar Sacristan-de Frutos, Jérôme Fleiter, Francois-Olivier Pincot, Gijs de Rijk, Lucio Rossi, Janne Ruuskanen, Antti Stenvall, and Felix J. Wolf. "10 kA Joints for HTS Roebel Cables". *IEEE Transactions on Applied Superconductivity*, 28(3):1–6, 2018.

[111] T Mulder, A Dudarev, D C van der Laan, M G T Mentink, M Dhallé, and H H J ten Kate. "Optimized and practical electrical joints for CORC type HTS cables". *IOP Conference Series: Materials Science and Engineering*, 102(1):012026, nov 2015.

[112] IATA. "Global Outlook for Air Transport Highly Resilient, Less Robust". https://www.iata.org/en/iata-repository/publications/economic-reports/global-outlook-for-air-transport---june-2023/, 2023. [Online].

[113] Clean Sky 2. "CLEAN SKY HIGHLIGHTS". https://clean-aviation.eu/sites/default/files/2021-08/Highlights-2020_en.pdf, 2020. [Online].

[114] Flightpath 2050. "Europe Vision for Aviation. Report of the High Level Group on Aviation Research". https://op.europa.eu/en/publication-detail/-/publication/296a9bd7-fef9-4ae8-82c4-a21ff48be673/language-en, 2011. [Online].

[115] Pat Wheeler and Sergei Bozhko. "The More Electric Aircraft: Technology and challenges". *IEEE Electrification Magazine*, 2(4):6–12, 2014.

[116] Tania C. Cano, Ignacio Castro, Alberto Rodríguez, Diego G. Lamar, Yehia F. Khalil, Laura Albiol-Tendillo, and Parag Kshirsagar. "Future of Electrical Aircraft Energy

Power Systems: An Architecture Review". *IEEE Transactions on Transportation Electrification*, 7(3):1915–1929, 2021.

[117] Hendrik Schefer, Leon Fauth, Tobias H. Kopp, Regine Mallwitz, Jens Friebe, and Michael Kurrat. "Discussion on Electric Power Supply Systems for All Electric Aircraft". *IEEE Access*, 8:84188–84216, 2020.

[118] Cheryl L. Bowman, Ty V. Marien, and James L. Felder. *"Turbo- and Hybrid-Electrified Aircraft Propulsion for Commercial Transport"*.

[119] Shreeder Adibhatla, Sanjay Garg, Scot Griffith, Kent Karnofski, Nathan Payne, and Bruce Wood. *"Propulsion Control Technology Development Roadmaps to Address NASA Aeronautics Research Mission Goals for Thrusts 3a and 4"*.

[120] Ryota Sugouchi, Masataka Komiya, Shun Miura, Masataka Iwakuma, Koichi Yoshida, Teruyoshi Sasayama, Takashi Yoshida, Kaoru Yamamoto, Yuichiro Sasamori, Hirokazu Honda, Yoshiji Hase, Masao Shuto, Masayuki Konno, and Teruo Izumi. "Conceptual Design and Electromagnetic Analysis of 2 MW Fully Superconducting Synchronous Motors With Superconducting Magnetic Shields for Turbo-Electric Propulsion System". *IEEE Transactions on Applied Superconductivity*, 30(4):1–5, 2020.

[121] S. Zanegin, N. Ivanov, D. Shishov, I. Shishov, K. Kovalev, and V. Zubko. "Manufacturing and Testing of AC HTS-2 Coil for Small Electrical Motor". *Journal of Superconductivity and Novel Magnetism*, 33(2):355–359, 2020.

[122] Fangjing Weng, Min Zhang, Tian Lan, Yawei Wang, and Weijia Yuan. "Fully superconducting machine for electric aircraft propulsion: study of AC loss for HTS stator". *Superconductor Science and Technology*, 33(10):104002, aug 2020.

[123] Andrew Bollman Christine Ross Angela Campbell Catherine Jones Michael J. Armstrong, Mark Blackwelder and Patrick Norman. "Architecture, Voltage, and Components for a Turboelectric Distributed Propulsion Electric Grid Final Report". https://ntrs.nasa.gov/citations/20150014237, 2015. [Online].

[124] Timothy J. Haugan, Mary Ann P. Sebastian, Chris J. Kovacs, Mike D. Sumption, and Bang-Hung Tsao. *"Design and Scaling Laws of a 40-MW-class Electric Power Distribution System for Liquid-Hydrogen Fuel-Cell Propulsion"*.

[125] Antonio Morandi. "HTS dc transmission and distribution: concepts, applications and benefits". *Superconductor Science and Technology*, 28(12):123001, oct 2015.

[126] Byeongmo Yang, Jiwon Kang, Seungryul Lee, Changlyul Choi, and Younghyun Moon. "Qualification Test of a 80 kV 500 MW HTS DC Cable for Applying Into Real Grid". *IEEE Transactions on Applied Superconductivity*, 25(3):1–5, 2015.

[127] Pavan Chaganti, Weijia Yuan, Min Zhang, Lie Xu, Eoin Hodge, and John Fitzgerald. "Modelling of a High-Temperature Superconductor HVDC Cable Under Transient Conditions". *IEEE Transactions on Applied Superconductivity*, 33(5):1–5, 2023.

[128] Steffen Elschner, Joerg Brand, Wilfried Goldacker, Markus Hollik, Andrej Kudymow, Severin Strauss, Victor Zermeno, Claus Hanebeck, Stefan Huwer, Wolfgang Reiser, and Mathias Noe. "3S–Superconducting DC-Busbar for High Current Applications". *IEEE Transactions on Applied Superconductivity*, 28(4):1–5, 2018.

[129] Makoto Hamabe, Makoto Sugino, Hirofumi Watanabe, Toshio Kawahara, Satarou Yamaguchi, Yasuhide Ishiguro, and Kuniaki Kawamura. "Critical Current and Its Magnetic Field Effect Measurement of HTS Tapes Forming DC Superconducting Cable". *IEEE Transactions on Applied Superconductivity*, 21(3):1038–1041, 2011.

[130] Byeongmo Yang, Jiwon Kang, Seungryul Lee, Changlyul Choi, and Younghyun Moon. "Qualification Test of a 80 kV 500 MW HTS DC Cable for Applying Into Real Grid". *IEEE Transactions on Applied Superconductivity*, 25(3):1–5, 2015.

[131] Dong Zhang, Shaotao Dai, Fengyuan Zhang, Zhiqin Zhu, Xi Xu, WeiWei Zhou, Yuping Teng, and Liangzhen Lin. "Stability Analysis of the Cable Core of a 10 kA HTS DC Power Cable Used in the Electrolytic Aluminum Industry". *IEEE Transactions on Applied Superconductivity*, 25(3):1–4, 2015.

[132] A. Ballarino and R. Flükiger. "Status of MgB2 wire and cable applications in Europe". *Journal of Physics: Conference Series*, 871(1):012098, jul 2017.

[133] Noriko Chikumoto, Hirofumi Watanabe, Yury V. Ivanov, Hirohisa Takano, Satarou Yamaguchi, Hiromi Koshizuka, Kazuhiko Hayashi, and Toru Sawamura. "Construction and the Circulation Test of the 500-m and 1000-m DC Superconducting Power Cables in Ishikari". *IEEE Transactions on Applied Superconductivity*, 26(3):1–4, 2016.

[134] ABB. "ABB BUSBAR PMAX H". `https://library.e.abb.com/public/dee65286d224176a48257b3c001f0722/ABB%20Busduct.pdf`. [Online].

[135] A. Jackson Bush, Afsara T. F. Khan, Deniz Lara Gunesen, Alfonso J. Cruz, and Lukas Graber. "Design and Optimization of a Cryogenic Coreless Inductor with Copper Clad Aluminum Conductor". In *2021 AIAA/IEEE Electric Aircraft Technologies Symposium (EATS)*, pages 1–6, 2021.

[136] Wan-Soo Nah, Jin-Ho Joo, and Jai-Moo Yoo. "Critical Current Degradation Analysis in HTS Pancake Coil due to Self Field Effects". *Progress in Superconductivity*, 1:68–72, Aug 1999.

[137] Víctor M R Zermeño, Krzysztof Habelok, Mariusz Stepień, and Francesco Grilli. "A parameter-free method to extract the superconductor's Jc(B,) field-dependence from in-field current–voltage characteristics of high temperature superconductor tapes". *Superconductor Science and Technology*, 30(3):034001, jan 2017.

[138] N V Bykovsky, S S Fetisov, A A Nosov, V V Zubko, and V S Vysotsky. "Analysis of critical current reduction in self-field in stacked twisted 2G HTS tapes". *Journal of Physics: Conference Series*, 507(2):022001, may 2014.

[139] Huiming Zhang, Min Zhang, and Weijia Yuan. "An efficient 3D finite element method model based on the T–A formulation for superconducting coated conductors". *Superconductor Science and Technology*, 30(2):024005, dec 2016.

[140] Fei Liang, Sriharsha Venuturumilli, Huiming Zhang, Min Zhang, Jozef Kvitkovic, Sastry Pamidi, Yawei Wang, and Weijia Yuan. "A finite element model for simulating second generation high temperature superconducting coils/stacks with large number of turns". *Journal of Applied Physics*, 122(4):043903, 07 2017.

[141] Edgar Berrospe-Juarez, Frederic Trillaud, Víctor M R Zermeño, and Francesco Grilli. "Advanced electromagnetic modeling of large-scale high-temperature superconductor systems based on H and T-A formulations". *Superconductor Science and Technology*, 34(4):044002, feb 2021.

[142] Steffen Elschner, Joerg Brand, Wilfried Goldacker, Markus Hollik, Andrej Kudymow, Severin Strauss, Victor Zermeno, Claus Hanebeck, Stefan Huwer, Wolfgang Reiser, and Mathias Noe. "3S–Superconducting DC-Busbar for High Current Applications". *IEEE Transactions on Applied Superconductivity*, 28(4):1–5, 2018.

[143] Michael J. Wolf, Walter H. Fietz, Christoph M. Bayer, Sonja I. Schlachter, Reinhard Heller, and Klaus-Peter Weiss. "HTS CroCo: A Stacked HTS Conductor Optimized for High Currents and Long-Length Production". *IEEE Transactions on Applied Superconductivity*, 26(2):19–24, 2016.

[144] Florian Schreiner, Bernd Gutheil, Mathias Noe, Wolfgang Reiser, Stefan Huwer, Claus Hanebeck, Carsten Räch, Marcus Röhrenbeck, and Fabian Schreiner. "Design and Manufacturing of a Multistage Cooled Current Lead for Superconducting High Current DC Busbars in Industrial Applications". *IEEE Transactions on Applied Superconductivity*, 27(4):1–5, 2017.

[145] Michael J. Wolf, Walter H. Fietz, Mathias Heiduk, Stefan Huwer, Andreas Kienzler, Sonja I. Schlachter, and Thomas Vogel. "200 kA DC Busbar Demonstrator DEMO 200 – Conceptual Design of Superconducting 20 kA Busbar Modules Made of HTS CroCo Strands". *IEEE Transactions on Applied Superconductivity*, 32(4):1–7, 2022.

[146] S. Mukoyama, M. Yagi, H. Hirata, M. Suzuki, S. Nagaya, N. Kashima, and Y. Shiohara.

"Development of YBCO high-Tc superconducting power cables". *Furukawa Review*, pages 18–22, 03 2009.

[147] Mark D. Ainslie, Weijia Yuan, Zhiyong Hong, Ruilin Pei, Tim J. Flack, and Tim A. Coombs. "Modeling and Electrical Measurement of Transport AC Loss in HTS-Based Superconducting Coils for Electric Machines". *IEEE Transactions on Applied Superconductivity*, 21(3):3265–3268, 2011.

[148] Z Hong, A M Campbell, and T A Coombs. "Numerical solution of critical state in superconductivity by finite element software". *Superconductor Science and Technology*, 19(12):1246, oct 2006.

[149] G Barnes, M McCulloch, and D Dew-Hughes. "Computer modelling of type II superconductors in applications". *Superconductor Science and Technology*, 12(8):518, aug 1999.

[150] Naoyuki Amemiya, Shun ichi Murasawa, Nobuya Banno, and Kengo Miyamoto. "Numerical modelings of superconducting wires for AC loss calculations". *Physica C: Superconductivity*, 310(1):16–29, 1998.

[151] Y. Le Floch, G. Meunier, C. Guerin, P. Labie, X. Brunotte, and D. Boudaud. "Coupled problem computation of 3-D multiply connected magnetic circuits and electrical circuits". *IEEE Transactions on Magnetics*, 39(3):1725–1728, 2003.

[152] Roberto Brambilla, Francesco Grilli, and Luciano Martini. "Development of an edge-element model for AC loss computation of high-temperature superconductors". *Superconductor Science and Technology*, 20(1):16, nov 2006.

[153] Dong Zhang, Shaotao Dai, Fengyuan Zhang, Zhiqin Zhu, Xi Xu, WeiWei Zhou, Yuping Teng, and Liangzhen Lin. "Stability Analysis of the Cable Core of a 10 kA HTS DC Power Cable Used in the Electrolytic Aluminum Industry". *IEEE Transactions on Applied Superconductivity*, 25(3):1–4, 2015.

[154] Byeongmo Yang, Jiwon Kang, Seungryul Lee, Changlyul Choi, and Younghyun Moon. "Qualification Test of a 80 kV 500 MW HTS DC Cable for Applying Into Real Grid". *IEEE Transactions on Applied Superconductivity*, 25(3):1–5, 2015.

[155] Steffen Elschner, Joerg Brand, Wilfried Goldacker, Markus Hollik, Andrej Kudymow, Severin Strauss, Victor Zermeno, Claus Hanebeck, Stefan Huwer, Wolfgang Reiser, and Mathias Noe. "3S–Superconducting DC-Busbar for High Current Applications". *IEEE Transactions on Applied Superconductivity*, 28(4):1–5, 2018.

[156] Drew W. Hazelton, Venkat Selvamanickam, Jason M. Duval, David C. Larbalestier, William Denis Markiewicz, Hubertus W. Weijers, and Ronald L. Holtz. "Recent Developments in 2G HTS Coil Technology". *IEEE Transactions on Applied Superconductivity*, 19(3):2218–2222, 2009.

[157] Hyung-Seop Shin, Marlon J. Dedicatoria, and Sang-Soo Oh. "Critical Current Degradation Behavior in Lap-Jointed Coated Conductor Tapes With IBAD Substrate Under Uniaxial Tension". *IEEE Transactions on Applied Superconductivity*, 20(3):1447–1450, 2010.

[158] Chris M. Rey, R. C. Duckworth, and Y. Zhang. "Splice Resistance Measurements on 2G YBCO Coated Conductors". *IEEE Transactions on Applied Superconductivity*, 19(3):2317–2320, 2009.

[159] Dong Keun Park, Min Cheol Ahn, Ho Min Kim, H. G. Lee, Ki Sung Chang, Sand Jin Lee, Seong Eun Yang, and Tae Kuk Ko. "Analysis of a Joint Method Between Superconducting YBCO Coated Conductors". *IEEE Transactions on Applied Superconductivity*, 17(2):3266–3269, 2007.

[160] Z.S. Hartwig, C.B. Haakonsen, R.T. Mumgaard, and L. Bromberg. "An initial study of demountable high-temperature superconducting toroidal field magnets for the Vulcan tokamak conceptual design". *Fusion Engineering and Design*, 87(3):201–214, 2012. Special Section on Vulcan Conceptual Design.

[161] Jun Lu, Ke Han, William R. Sheppard, Youri L. Viouchkov, Kenneth W. Pickard, and William Denis Markiewicz. "Lap Joint Resistance of YBCO Coated Conductors". *IEEE Transactions on Applied Superconductivity*, 21(3):3009–3012, 2011.